Ph.D. THESIS

Digital Low-Level Radio-Frequency phase-amplitude feedback development and its application for KEK LUCX facility stabilization

デジタル低電力高周波位相振幅フィードバック開発とその KEK LUCX 施設安定化への応用

Popov Konstantin

DOCTOR OF PHILOSOPHY

Department of Accelerator Science

School of High Energy Accelerator Science

The Graduate University for Advanced Studies, SOKENDAI

2023

Supervisor: Alexander Aryshev

Co-supervisor: Nobuhiro Terunuma

Reviewers: Takako Miura

Toshihiro Matsumoto

Tetsuya Kobayashi

Yuuki Uesugi

Day of submission: 8th of the September

For: my mother

Popova Nadezhda Vasilievna

And my younger sister

Popova Dariya Evgenievna

Посвящается моей маме

Поповой Надежде Васильевне

и моей младшей сестре

Поповой Дарье Евгеньевне

Thank myself

for hardworking!

Я благодарю себя

за трудолюбие!

I will be a Nobel Prize physicist someday!

Однажды, я стану Нобелевским Лауреатом!

ABSTRACT

X-Ray is widely utilized in material science [1], applied biology [2] and medicine science [3]. Synchrotron radiation facilities such as KEK-PF [4], Spring-8 [5] provide high-quality intense X-Ray. Despite of their capabilities, these facilities are large scale and difficult to maintain. However, an intense monochromatic source of X-Ray based on laser-Compton backscattering phenomena [6-8] is an alternative to synchrotron radiation facilities. Over decade, several scientific organizations performed an R&D in this field. High Energy Accelerator Research Organization (KEK) is one of these organizations.

The KEK LUCX facility [9] is a normal conductive compact multi-bunch linear electron accelerator. It is devoted to develop and operate an intense monochromatic X-Ray source for imaging and tomography applications [10]. The X-Ray parameters, such as energy, energy bandwidth, temporal structure and flux, are defined by the multi-bunch beam and laser pulses train characteristics [8, 11]. From the accelerator side, X-Ray parameters stability are limited by the electron beam characteristics, such as transverse normalized emittance, average energy, energy spread, bunch charge, bunch length and arrival time. All these characteristics depend on the accelerating field phase and amplitude absolute values and its stability [12, 13].

The LUCX facility RF-Gun and 12-cell Linac [12, 13] stabilization is a milestone to generate the stable electron beam to produce highest quality laser-Compton X-Ray. Therefore, a digital Low-Level Radio-Frequency (LLRF) feedback was developed, implemented and tested at KEK LUCX facility for the RF field precise control.

This research investigates implementation of the FPGA board based digital LLRF feedback to stabilize accelerating field phase and amplitude inside the LUCX S-band RF-Gun and 12-cell Linac [12]. RedPitaya STEMlab 125-14 FPGA board [14] equipped with ZYNQ-7010 chip [15] was chosen for the feedback development, implementation and test at KEK LUCX facility due to competitive specifications, standalone form-factor and commercial availability [14].

The following tasks were accomplished during the research:

- Review the basic accelerator feedback principles possible to utilize with RedPitaya STEMlab 125-14 FPGA board.
- Review the stability and reliability of existing KEK LUCX facility beam diagnostics, DAQ, timing and LLRF.
- Creation of an ASTRA particle tracking simulation for LUCX beamline: the electron bunch parameters dependence on the RF-Gun and 12-cell Linac accelerating fields phase simulated in ASTRA tracking code. Beam line simulation model limitations study and its potential usage for feedback corrections calculation.
- Implementation of feedback algorithm with the Digital Down-Conversion (DDC) and Digital Up-Conversion (DUC) on the RedPitaya STEMlab 125-14 FPGA board.
- Summary of beam parameters, tuning knobs with associated tuning ranges which can be included into feedback algorithm.
- FPGA based LLRF feedback programming and its implementation into KEK LUCX facility LLRF system.
- Inclusion of the feedback system tuning knobs and monitors into the existing EPICS control system of LUCX.
- Demonstration of the accelerating field phase and amplitude stability in the LUCX S-band RF-Gun and 12-cell Linac. Long-term measurement of the feedback system performance. The electron beam energy, energy spread, charge stability measurement at experiment.

The thesis presents results of the RedPitaya STEMlab 125-14 FPGA board based LLRF phase and amplitude feedback development, implementation and test at the KEK LUCX facility. The RF-Gun and 12-cell Linac cavities accelerating field phases stability was improved from 2.4 ° (RMS) to the 0.09 ° (RMS). The experimental results of the electron beam parameters stabilization (average energy, energy spread (RMS) and bunch charge) demonstrate 10 times improvement. As an optimistic prediction, laser-Compton X-Ray characteristics stability will be improved 10 times too.

Contents

CHAPTER 1

Introduction

KEK LUCX facility is located in the KEK Accelerator Test Facility (ATF) building. The facility size is 20 x 15 m^2. The facility includes accelerator tunnel with experimental stations, two klystrons with modulators and waveguide system, RF-Gun laser system room and control room.

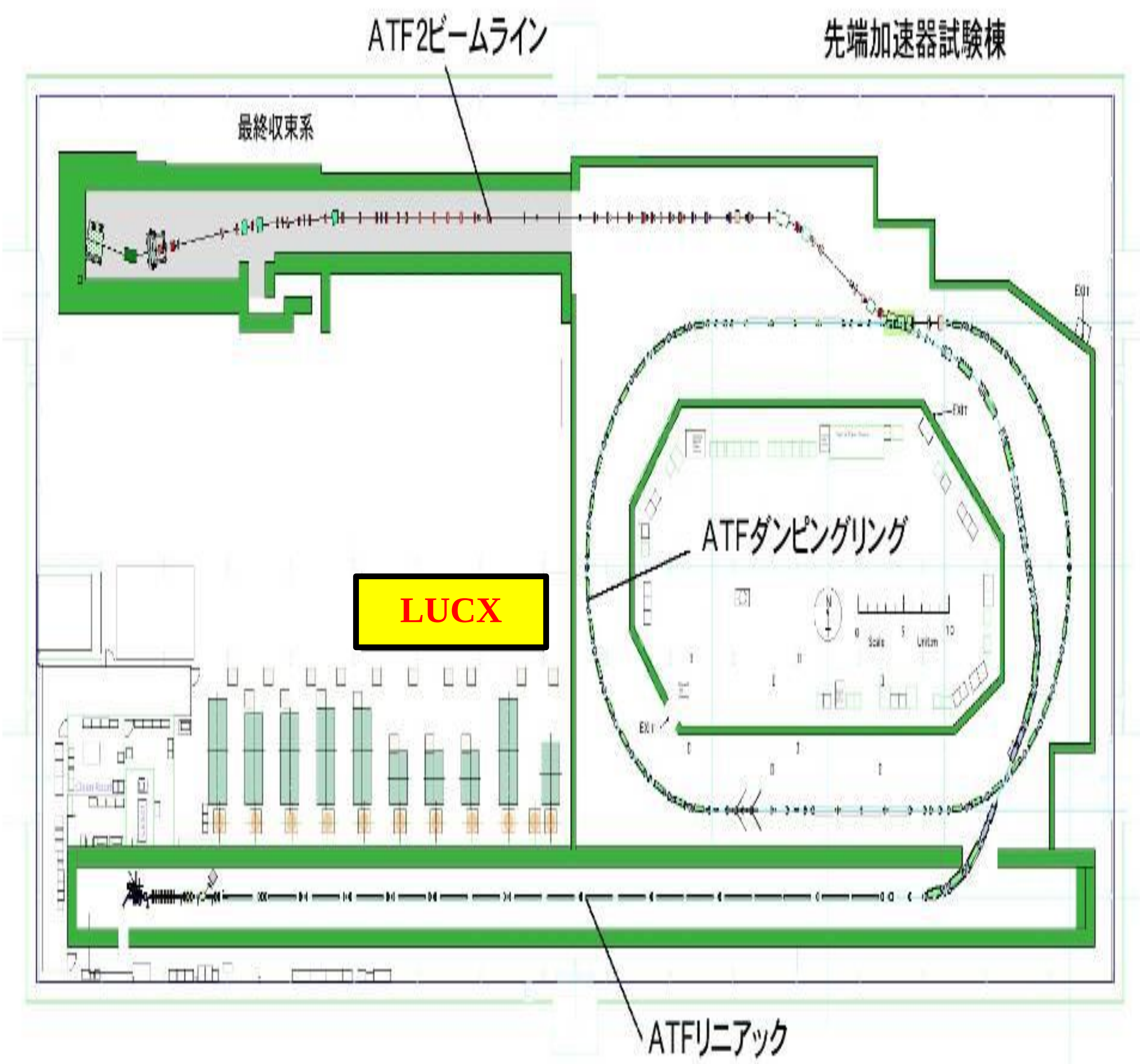

Figure 1: KEK LUCX facility location in the Accelerator Test Facility building

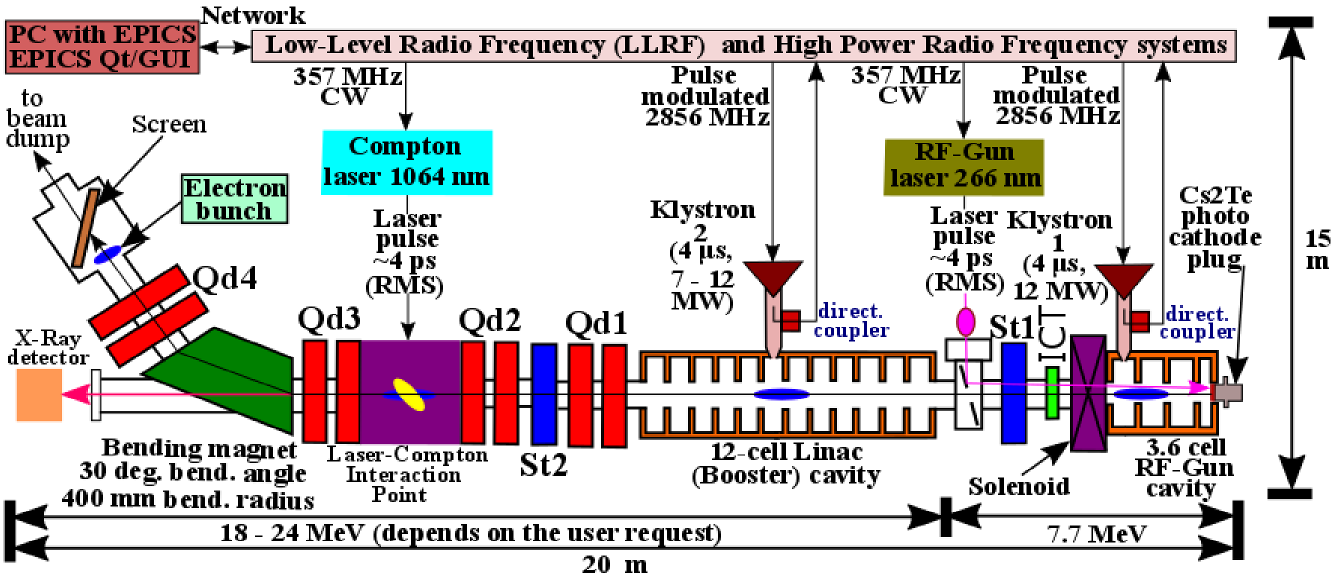

Figure 2: KEK LUCX facility beamline schematic: **Qd** is the quadrupole doublet, **St** is the steering magnet, **ICT** is the integrating Current Transformer

KEK LUCX facility has laser-driven standing wave 3.6-cell RF-Gun and 12-cell Linac (Booster), which accelerate electron beam up to 18-24 MeV. The electron beam energy depends on a user request and experiment requirements. Beamline includes solenoid, steering magnets, quadrupole magnet doublets and bending magnets.

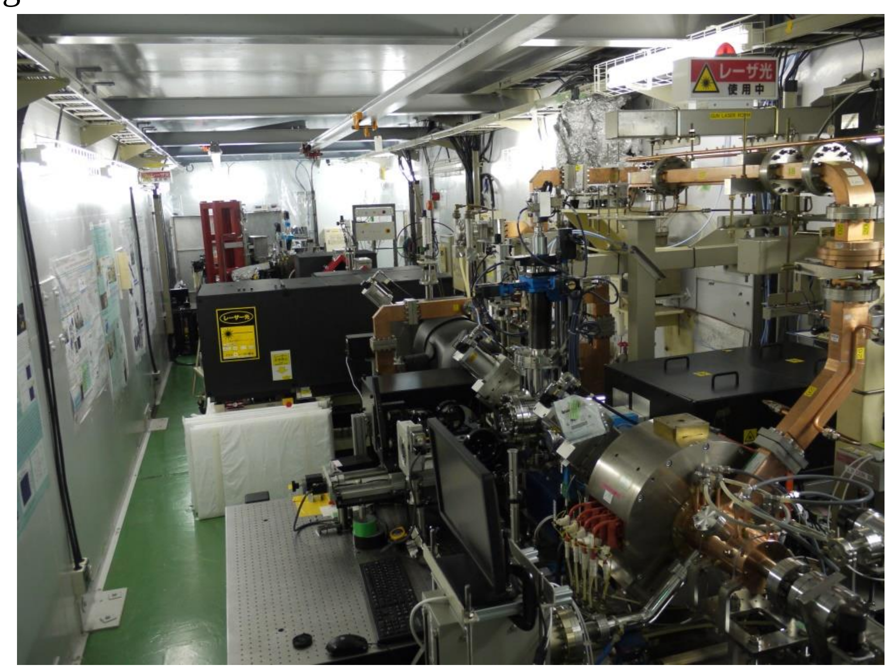

Figure 3: KEK LUCX facility beamline photo

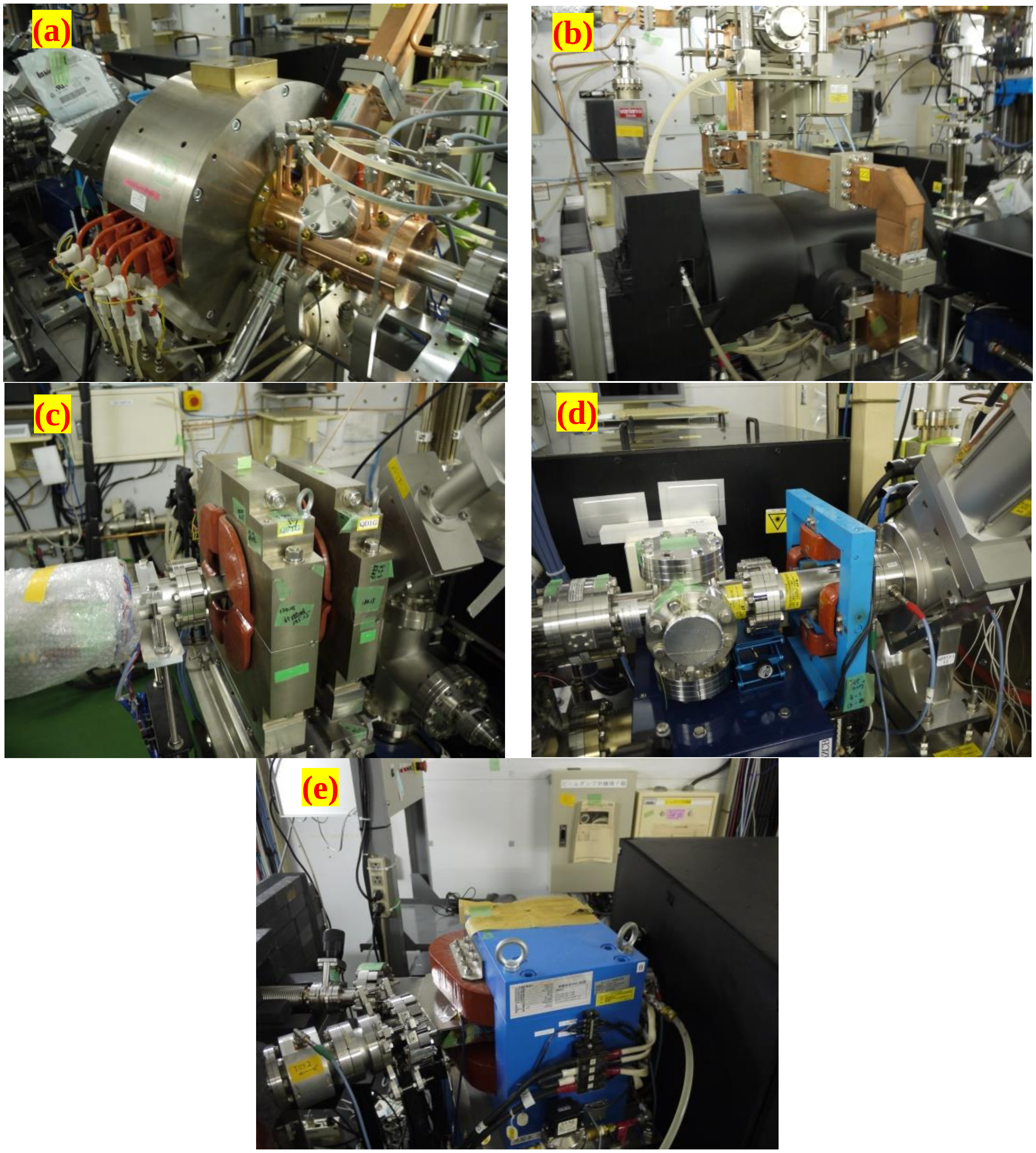

Figure 4: Photos of KEK LUCX accelerator beam line components: (a) is the RF-Gun and Solenoid, (b) is the Booster cavity with temperature isolation cover, (c) is the quadrupole magnet doublet, (d) is the steering magnet and (e) is the bending magnet

The magnet system, beam parameter monitors, RF, timing and beam optics are explained in the next sections.

1.1 Photo-cathode RF-Gun

The Gun is 3.6-cell normal conductive cavity. The Figure 5 demonstrates the schematic of the RF-Gun accelerating cavity.

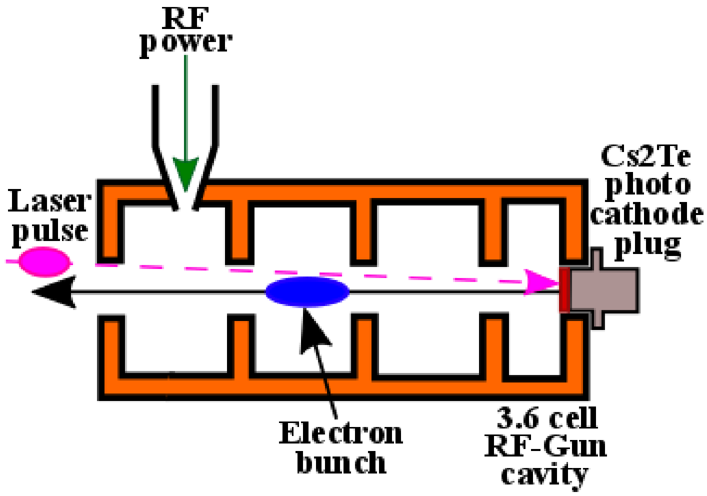

Figure 5: RF-Gun cavity schematic

The RF-Gun is a standing wave RF resonant cavity made up of 4 cylindrical cells: 3 full cells and 1 half-cell. The RF-Gun cavity operating frequency is 2856MHz. Each cell is fabricated from oxygen-free copper, and the end plate of the half-cell has a hole for mounting the cathode plug. With such approach, electrons are generated using photoeffect phenomena. Photo electrons are produced by Cs2Te photocathode [16] irradiation by 266 nm laser light. The electrons are accelerated by the RF field up to 8 MeV, thereby minimizing the emittance growth induced by the space charge effect [17]. The electron beam has normalized transverse emittance at 2.8 π mrad mm and a short pulse at 4 ps (RMS) due to the short laser pulse duration and bunching effect in the RF-Gun cavity [17].

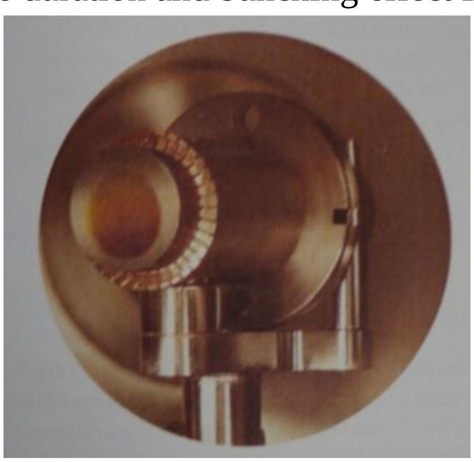

Figure 6: Photo of Cs2Te photo-cathode with plug [18]

Cs2Te is produced in evaporation equipment on a Mo plug and transported to the RF-Gun cavity within a constant vacuum. Cs2Te is evaporated on the plug surface (circle area).

1.2 RF-Gun laser system

The timing and profile of the photo electrons are determined by the photo-cathode irradiation by 266 nm laser light pulse. In order to produce a multi-bunch electron beam, multi-pulse UV laser system synchronized with the RF accelerating field operates at KEK LUCX facility. Figure 7 demonstrates the scheme of the photo-cathode irradiation.

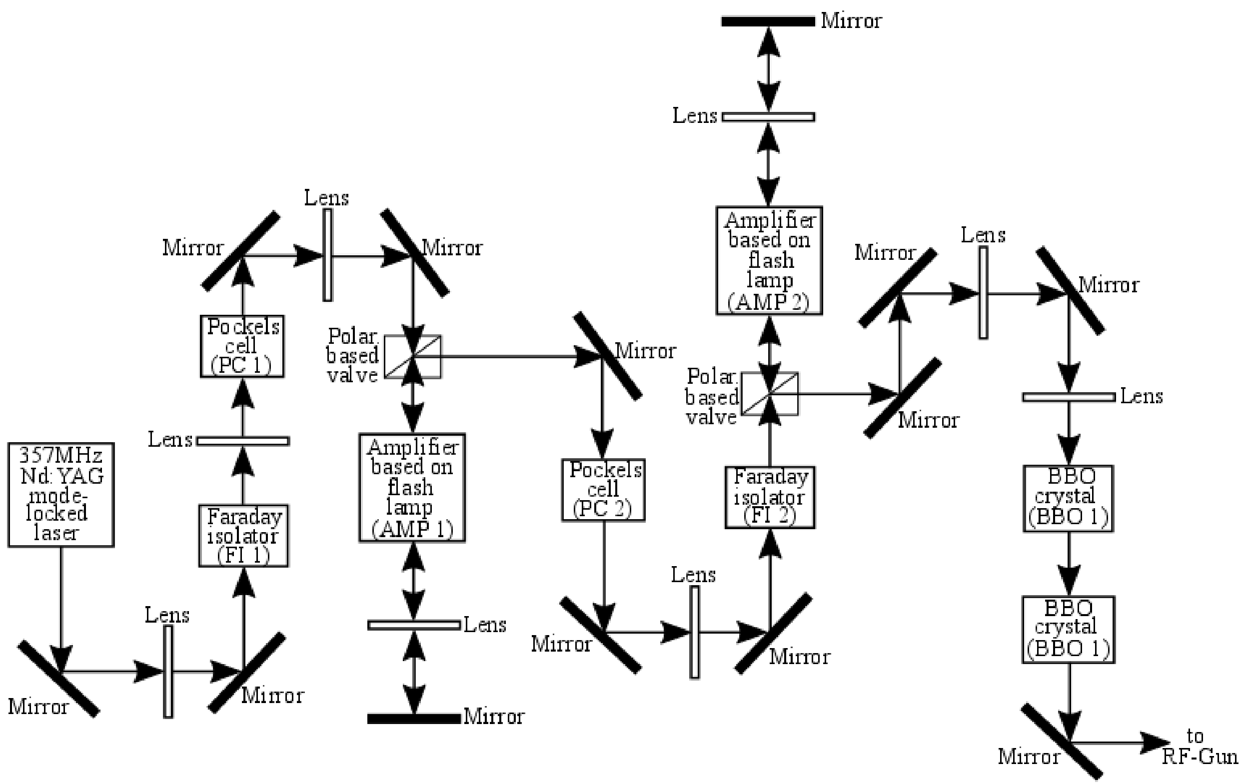

Figure 7: LUCX photo-cathode irradiation schematic

The seed pulses are produced in Nd:YAG mode-locked oscillator (Time Bandwidth Products) with repetition frequency of 357 MHz. 357 MHz is the 8^{th} subharmonics of 2856 MHz. The timing jitter between the 357 MHz CW reference signal fed into the laser oscillator feedback and output pulses is 100 fs (RMS) according to the readout output.

The oscillator average power is 9 W, wavelength is 1064 nm, the laser pulse length FWHM is 7 ps (RMS is ~ 3 ps). The oscillator is stabilized by phase-locked loop. The phase-locked loop utilizes piezo actuator in the oscillator cavity.

The laser pulse train passes through Faraday isolator to avoid a return light and then train is injected into the first Pockels cell. The Pockels cells passes limited number of laser pulses. The number is controlled by accelerator operator. The number range is from 4 to 1000. Then, the pulses are amplified by the first amplification module. The pulses pass through the module twice (double pass) via pumping by pulse flash lamp, and are amplified about 100 times. The amplified pulses pass through the second Pockels cell to increase the contrast ratio, then it goes to the second amplifier. Finally, amplified 1064 nm laser pulses are converted to the 266 nm by two BBO crystals.

After the conversion from 1064 nm to 266 nm, the pulse energy is ~3 μJ/pulse. Pulse train is guided to the photo-cathode installed in the RF-Gun accelerating cavity.

The pulse train is transported through ~11 m long optical beam line and passage through vacuum window and optical components, the estimated duration of the 266 nm laser pulse is 5 ps (RMS). The part of the optical beamline is shown on the figure 8.

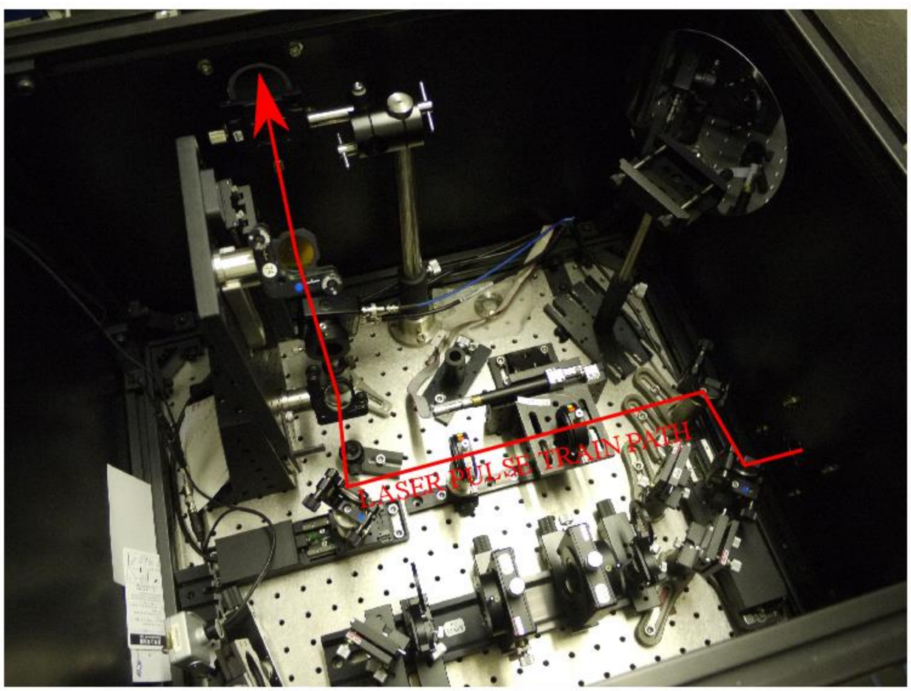

Figure 8: The part of the laser pulse train optical beamline

The transverse density of the UV pulse at the photocathode is controlled via a virtual cathode consisting of a UV sensitive CCD camera installed outside of the vacuum chamber to provide a one-to-one optical image of the real cathode.

The virtual cathode CCD camera with beam matching optics is demonstrated on the figure 9. The figure 9 shows only a part of the beam matching optics.

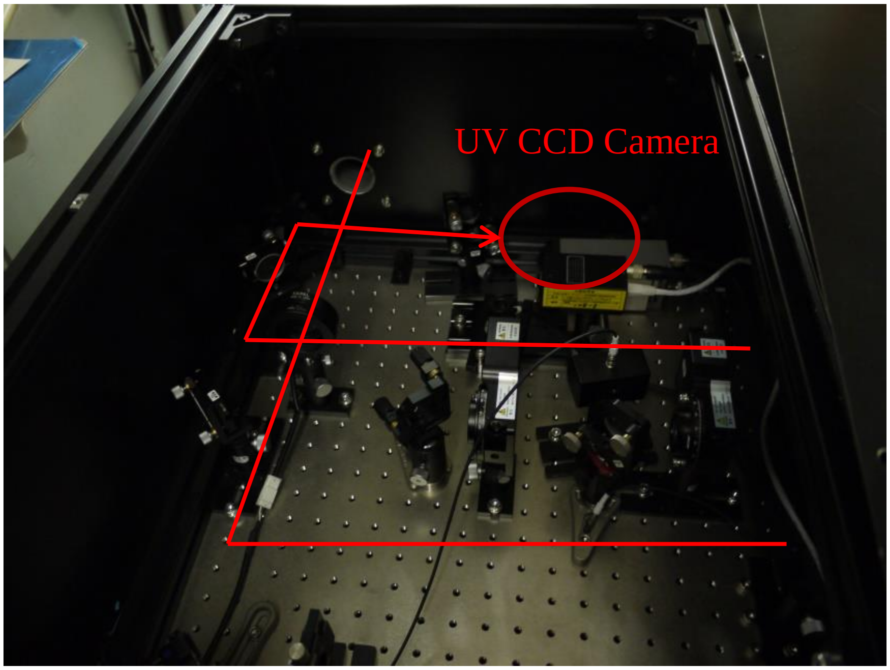

Figure 9: The virtual cathode CCD camera beam matching optics
and CCD camera itself

The figure 10 shows the typical transverse spatial distribution of the UV laser pulse train (4 laser pulses in train) on the virtual cathode. The UV pulse transverse density is $800 \times 800\ \mu m^2$(RMS).

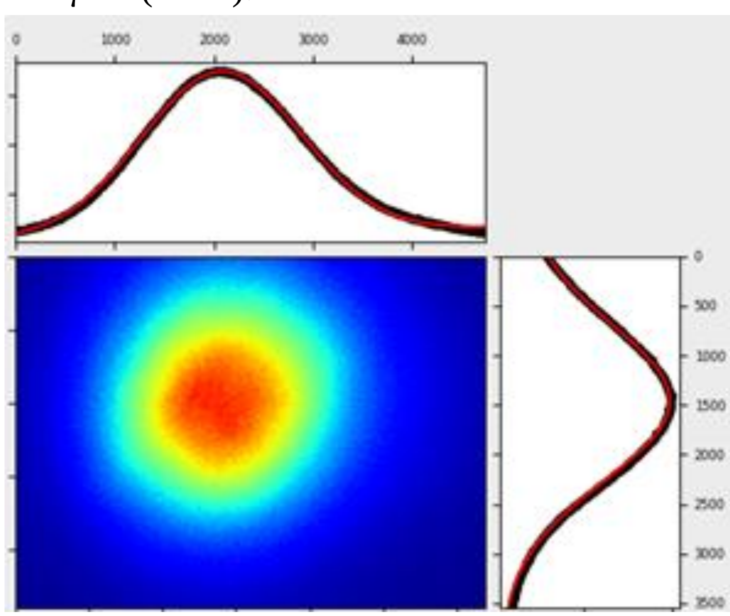

Figure 10: The laser beam typical transverse profile (the projection units are μm)

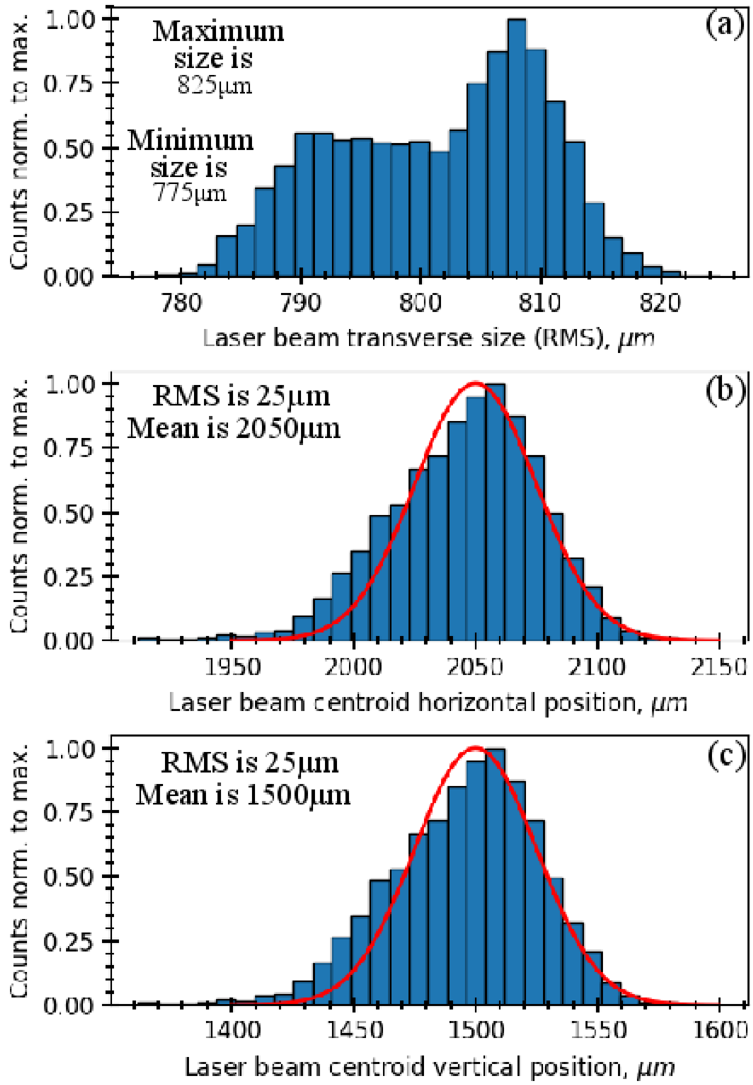

Figure 11: The laser pulse train (4 pulses in train) transverse profile parameters jitter: (a) is the laser pulse train transverse size histogram, (b) is the laser pulse train centroid position (horizontal direction), (c) is the laser pulse train centroid position (vertical direction)

Number of bins is 30. The data for histograms has 10000 profiles. For the visibility sake, the histograms data maximums are normalized to 1.

The train transverse profile stability data has not Gaussian shape, hence the stability characteristics are minimum and maximum sizes, which are 775μm and 825 μm.

The laser pulse train (4 pulses in train) energy jitter measured with an energy meter is demonstrated on the figure 12.

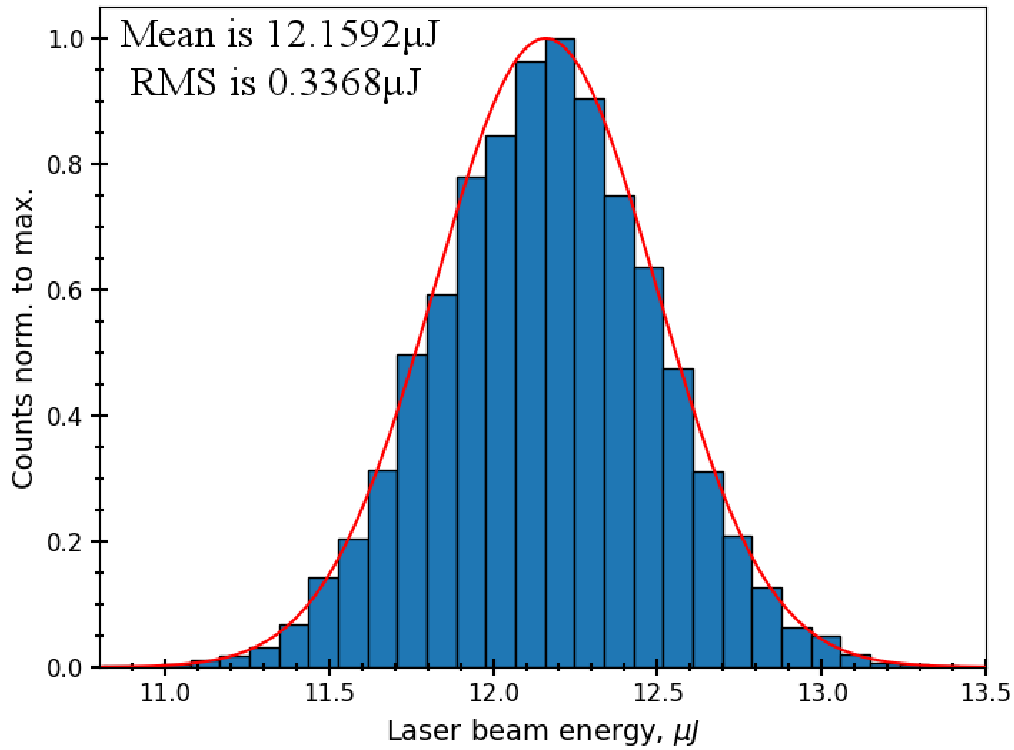

Figure 12: Laser pulse train energy jitter

The train consists from 4 individual laser pulses. The laser pulse spacing is 2.8 ns. So, the energy jitter of a single laser pulse is 0.3368 μJ/4. It is 0.0842 μJ, mean value is 3.0398 μJ. The laser pulse energy jitter is ~3 %. From general point of view, such jitter can be neglected. The train transverse profile parameters jitter is ~ 1 %. So, its influence can be neglected too.

1.3 Booster

Once generated in the RF-Gun, the multi-bunch electron beam passes through solenoid and steering magnets (see figure 2). Then, it enters Booster. The Booster is 12-cell standing wave accelerating cavity [19]. Its schematic is demonstrated on the figure 13.

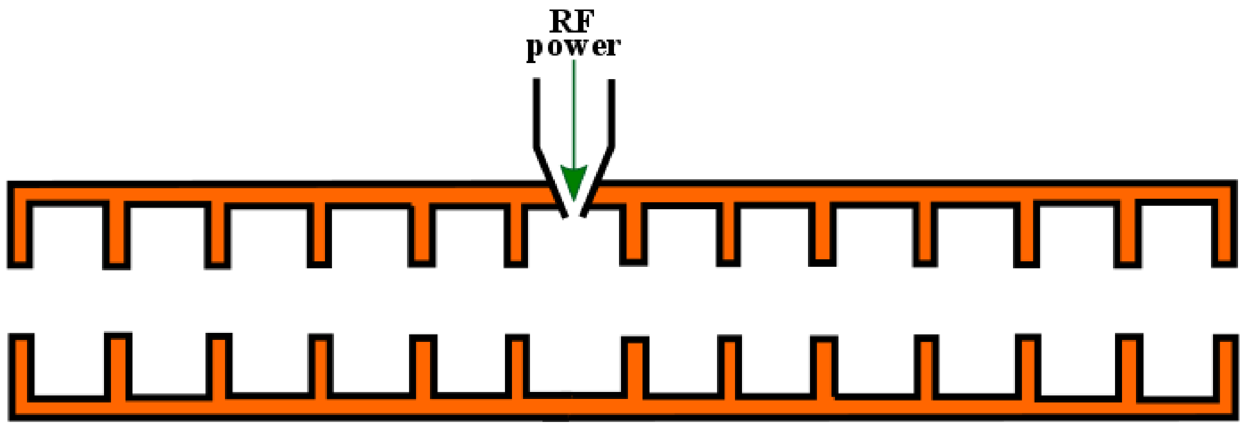

Figure 13: Booster cavity schematic

The Booster is an RF resonate cavity made up of 12 cylindrical full cells. The Booster cavity operating frequency is 2856MHz.

Each cell is fabricated from oxygen-free copper. In general, the phase of the Booster is tuned to get maximum energy gain. Yet, the bunch from the RF-Gun has a finite energy spread, while the electrons at the head and tail of the bunch have a wide energy spread (high energy at the head, low energy at the tail). To decrease energy spread, the Booster accelerating field phase is tuned to have the minimum energy spread as possible.

1.4 RF system

Toshiba 3729 [20] and Toshiba 3712 [21] klystrons supplies the high power to the RF-Gun and Booster cavities via waveguide system (see figures 2, 3 and 4). The high power RF field is controlled by Low-Level RF system. Moreover, LLRF signals phase-lock the RF-Gun Nd:YAG laser oscillator and trigger branch signals with accelerating field phase.

Figure 14: Toshiba 3712 klystron: (a) is the klystron without cover, (b) is the klystron with cover

Directional couplers are installed on the waveguide system for RF-field diagnostic purposes. Its coupling and directivity are 60 dB and 20 dB, respectively.

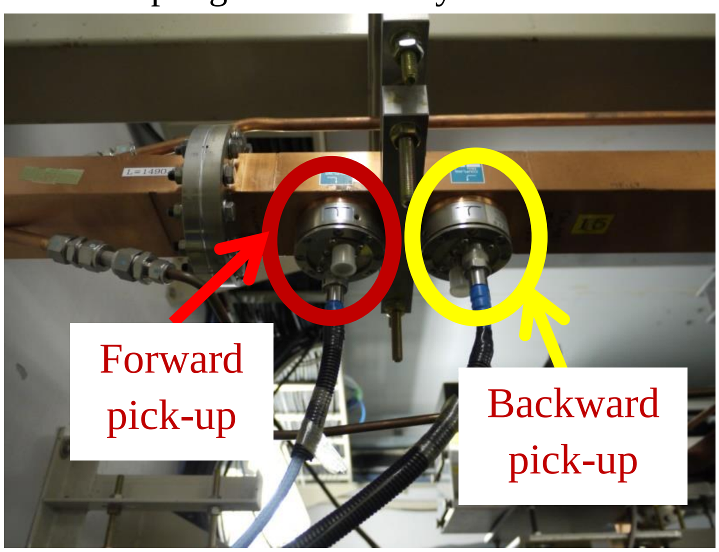

Figure 15: RF-Gun directional couplers photo

Directional coupler installed to pick up the RF-power, which is transferred from the klystron to the cavity, is utilized to control accelerating field phase and amplitudes. The LLRF system is comprehensively described in the next chapters.

1.5 RF-Gun and Booster cavities water cooling system

RF-Gun and Booster cavities temperature control is realized using water cooling system, so called chillers. The chiller supplies water with a certain temperature from its water tank to the cavities via plastic tubes. Hence, water is keeping the cavities body temperature constant. Pipe with water enters the cavity and passes through the all cells and return back to the chiller. The returned water temperature is compared with setup temperature and the chiller controller adjusts the water temperature. Thermoflex 1400 [22] recirculating chillers are utilized at KEK LUCX facility. According to the chiller datasheet, the water temperature control resolution is 0.1 ℃.

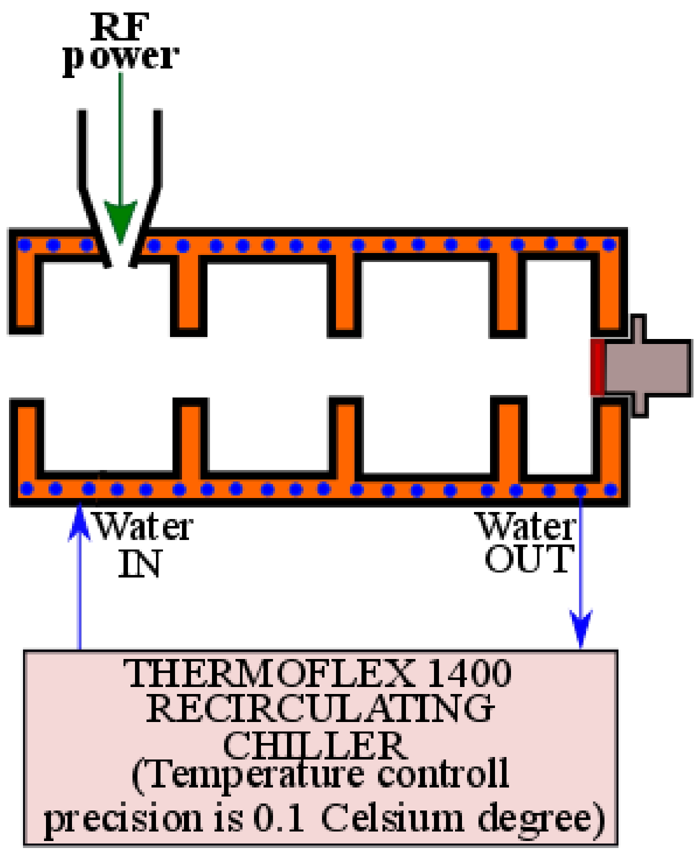

Figure 16: RF-Gun temperature control schematic

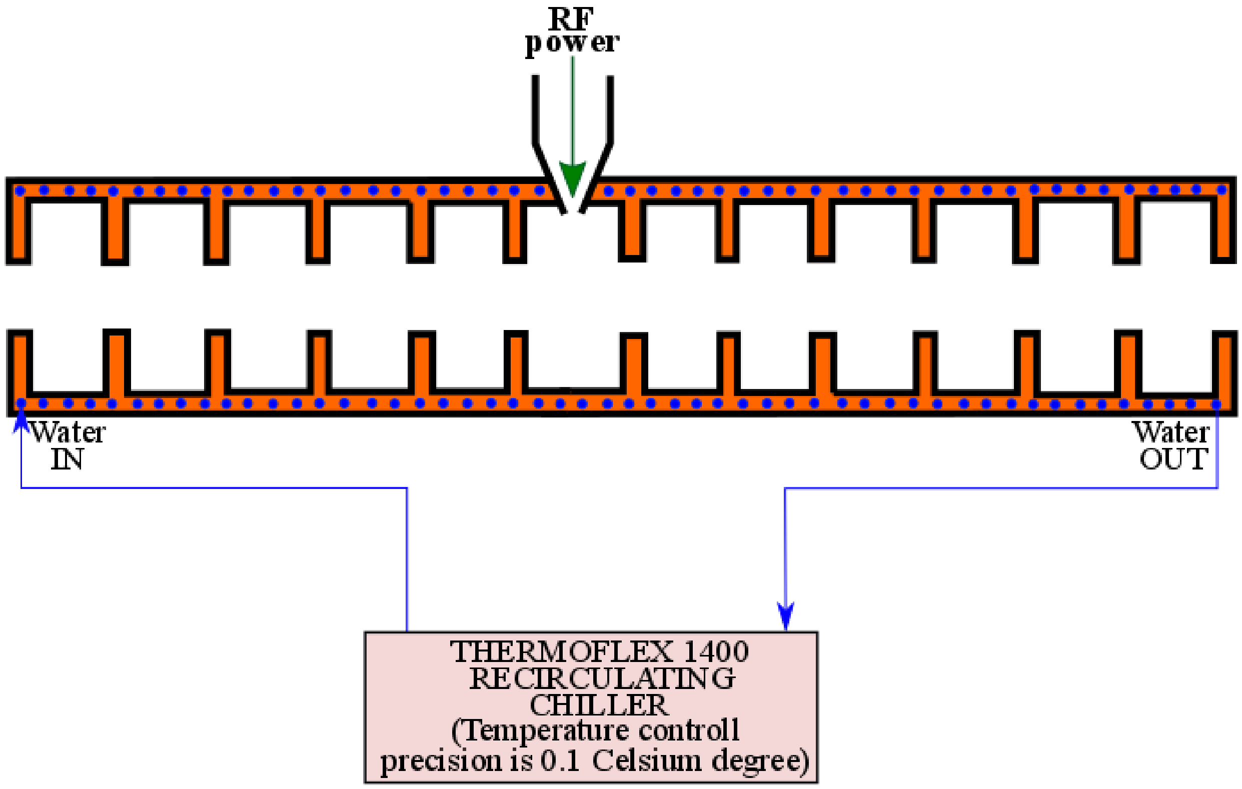

Figure 17: Booster temperature control schematic

Figure 18: Thermoflex 1400 recirculating chiller

The entire accelerator is located inside the tunnel. The temperature inside the LUCX tunnel is controlled by conventional air conditioner from Mitsubishi Electric [23] without readback. The air flow direction is periodically changing to cool down the tunnel more effectively. The period is several minutes.

Figure 19: Mitsubishi Electric air conditioner

Booster cavity has an additional temperature isolation cover, while RF-Gun cavity has not the cover. So, RF-Gun cavity body and surface are affected by any environment fluctuations more than Booster cavity body and surface.

The cavities surface temperature monitors are T-type thermocouples. Temperature detection resolution is 0.1 ℃. The photo of the thermocouples installed on the RF-Gun surface is shown on the figure 20.

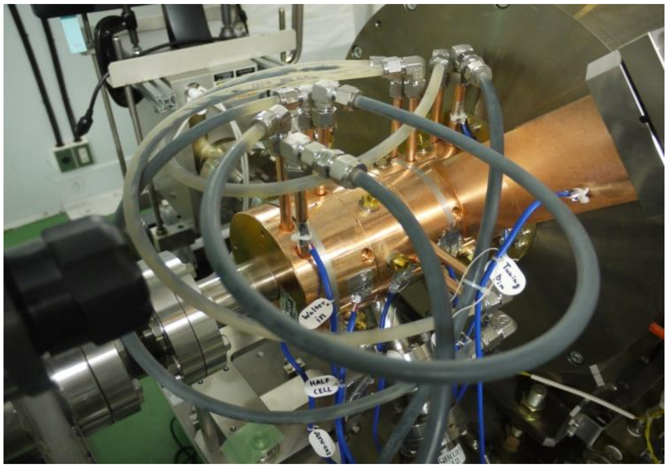

Figure 20: The photo of the thermocouples installed on the RF-Gun surface

The signals from thermocouples are digitized by ADC and sent to the EPICS PV [24]. So, the cavities surface and cooling water temperature are monitored in real-time.

1.6 Beam monitors

Many beam monitors are installed in the KEK LUCX accelerator beamline to characterize the beam parameters and monitor beam conditions. The facility has 1 beam current monitor, 9 button type beam position monitors (BPM) and 5 beam profile monitors. Beam profile monitors are scintillator screens.

1.6.1 Beam current monitor

The beam current monitor is the Integrating Current Transformer (ICT).

The Integrating Current Transformer (ICT) was designed to measure intensity of short bunches with several picoseconds length (RMS). The ICT fundamental principle is the same as conventional current transformer (CT) demonstrated on the figure 21, but the ICT integrates the signal with a time constant (it depends on the circuit) to suppress the core losses and Eddy current .

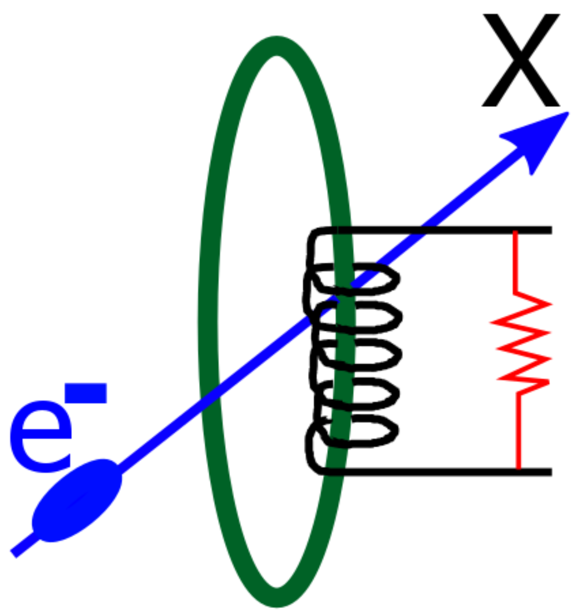

Figure 21: Current transformer diagram

The advantage of the ICT is non-distractive monitoring. So, it is possible to measure integral beam current. The ICT can measure beam charge by recalculation from current to charge. Bunch-by-bunch spacing at LUCX is 2.8 ns. The ICT cannot measure bunch-by-bunch, so it measures the charge of the entire electron beam.

The resolution of the ICT itself plus data acquisition electronics noise allows measuring the bunch charge with 2 pC resolution according to the datasheet [25].

The RF-Gun phase scan measurement schematic is demonstrated on the figure 22. Phase scan is the electron beam charge dependence on the RF-Gun cavity accelerating field phase.

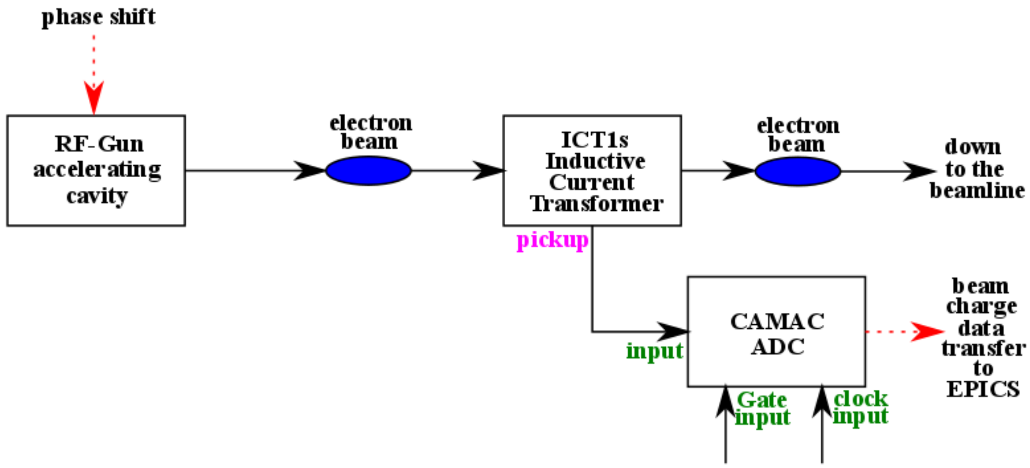

Figure 22: phase scan measurement schematic

The RF-Gun accelerating field phase is shifted by the LLRF system (see next chapters). Then, the bunch charge is detected by the ICT. At the final step, the ICT signal is digitized by ADC and recorded to the EPICS PV.

An example of the bunch charge vs the RF-Gun cavity accelerating phase dependence is demonstrated on the figure 23.

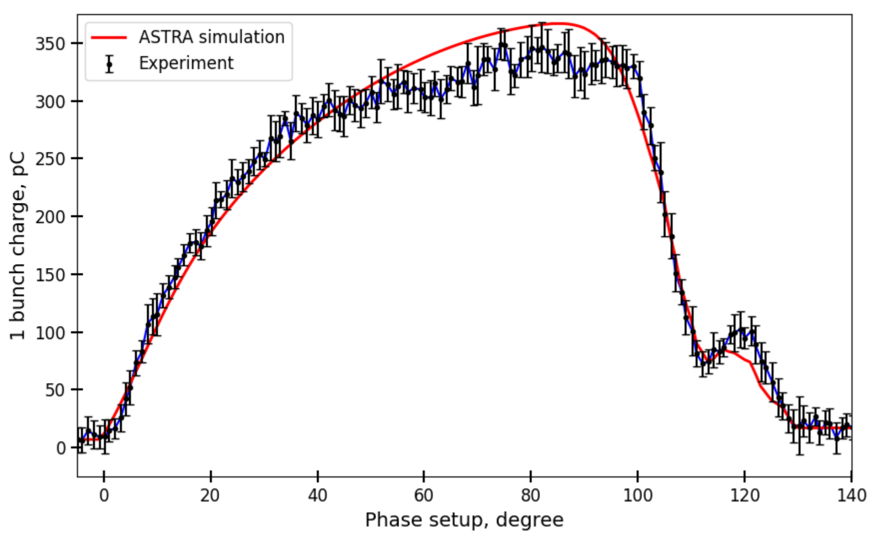

Figure 23: Phase scan data matched with simulated one in ASTRA

The electron beam charge (4 bunches in beam) was measured, then the data values were divided by 4.

The bunch charge vs the RF-Gun cavity accelerating phase dependence was matched with data simulated at ASTRA. As can be seen at figure 23, the simulation data and measured data are matching within the measurement error bars. Every point was measured 10 times, and then mean values and standard deviation were calculated. Standard deviation is plotted as a measurement error.

1.6.2 Beam position monitors

Nine beam position monitors (BPM) are installed in the LUCX accelerator beamline for the beam orbit measurement. These BPMs have four button-type electrodes in the horizontal and vertical directions (see figure 24).

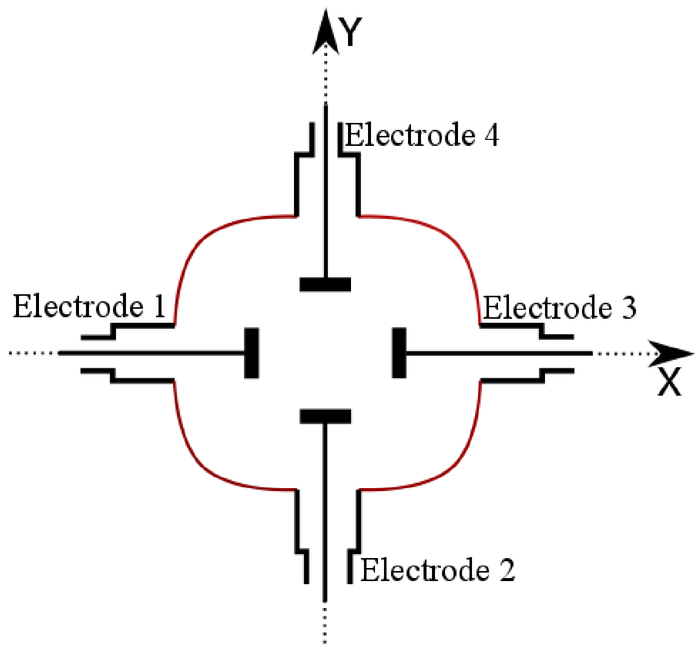

Figure 24: Button type beam position monitor (BPM) schematic

The electron beam induces an image charge (or induces the surface currents) on the electrodes, and the image charge is detected as a bi-polar signal pulse. The signal amplitude depends on the electron beam charge and a distance between the beam and electrodes.

The beam position is proportional to the signal asymmetry of the two opposite electrodes:

$$x = S_x \cdot \frac{V_3 - V_1}{V_3 + V_1}, \qquad (1)$$

where x is the horizontal transverse beam position, V_1 is the signal amplitude on the electrode 1, V_3 is the signal amplitude on the electrode 3, S_x is the sensitivity coefficient determined by the geometrical structure.

$$y = S_y \cdot \frac{V_2 - V_4}{V_2 + V_4}, \quad (2)$$

where y is the vertical transverse beam position, V_2 is the signal amplitude on the electrode 2, V_4 is the signal amplitude on the electrode 4, S_y are the sensitivity coefficient determined by the geometrical structure.

1.6.3 Beam profile monitors

The type of beam profile monitor installed in KEK LUCX facility for beam transverse size monitoring is scintillator screen. The scintillator type is alumina fluorescent plate (named as a screen hereafter).

An alumina fluorescent plate (AF995R, Desmarquest Co.) has sufficient sensitivity to scintillate under stimulation by electron beam with pC level charge. An alumina fluorescent plate is made from 0.5% chromium oxide (Cr_2O_3)-doped alumina (Al_2O_3). It takes a name “desmarquest” from the company-manufacturer. The scintillation light wavelength is 693 nm. The detection resolution is limited by the grain size of the fluorescent plate. The resolution is enough to work with electron beam sizes around 100 micrometers (RMS) and bunch charge at hundreds pC.

1.6.4 Beam energy monitor

Beam energy monitor consists of the bending magnet (B1), quadrupole doublet (Qd4) and screen. The conventional technique is applied to analyze the electron beam average energy based upon relationship between the Lorentz force and magnetic field. The electron beam can be directed through the center of the beam pipe or screen by adjusting the current of the analyzer magnet. The electron beam energy is obtained by measuring the current (magnetic field of the bending magnet) and considering beam profile position on scintillator screen and the bending magnet design.

The magnet is the electromagnet with coil. The relationship between current and magnet field is linear.

$$B \sim I, \quad (3)$$

where B is the magnetic field, I is the current supplied to the magnet coil.

The figure 25 demonstrates the experimental dependence between magnet field and current supplied by the power supply to magnet coil. The data and equation 4 are provided by the company manufacturer.

$$B = 0.007903 \cdot I + 0.005376, \quad (4)$$

where B is the magnetic field (in Tesla), I is the current supplied by the power supply to magnet coil (in A).

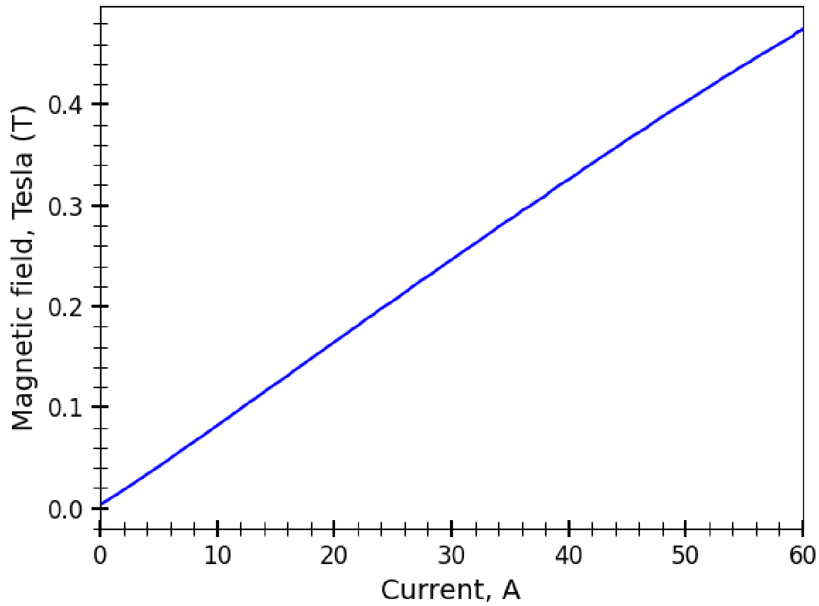

Figure 25: Experimental dependence between magnetic field of the bending magnet and current supplied to the magnet coil

The bending magnet is the sectoral magnet. The bending radius is 400 mm defined by the magnet geometry. The angle between the electron beam propagation direction at the magnet input and electron beam propagation direction at the magnet output is 30 °. The sectoral magnet has a limited acceptance (angle and momentum). Hence, only particles with a limited range of a bending radius centered on 400 mm can pass through the entire magnet, enter the beamline and hit the screen.

The dependence between magnet field, bending radius and the particle momentum is called "magnetic rigidity".

$$B \cdot \rho = pc/300, \quad (5)$$

where B is the magnetic field [Tesla], ρ is the bending radius [m], p is the magnitude of the particle momentum [MeV/c], c is the speed of light.

The dependence between particle momentum and total energy is explained by equation 6:

$$pc = \sqrt{E_{total}{}^2 - E_{rest}{}^2}, \tag{6}$$

where p is the magnitude of the particle momentum, c is the speed of light in vacuum, E_{total} is the total energy of the electron beam. E_{rest} is the rest energy of electron beam.

$$E_{rest} = 0.511\ MeV \tag{7}$$

The equation 6 substitution to equation 5 gives equation 8:

$$B \cdot \rho = \sqrt{E_{total}{}^2 - E_{rest}{}^2}/300 \tag{8}$$

As a result, the dependence between the total energy or magnitude of the particle momentum and the current supplied to the magnet coil is linear. So, the calibration equation from the current supplied to the magnet coil and the electron beam average energy is demonstrated in the equation below. Substitute equation 4 to equation 8 and restructure to get $E_{total} = E_{total}(I)$:

$$E_{total} = \sqrt{((0.007903 \cdot I + 0.005376) \cdot \rho \cdot 300)^2 + E_{rest}^2}, \tag{9}$$

where I is the current (in A), ρ is the bending radius (in meters), E_{rest} is the 0.511MeV, E_{total} is the total energy (in MeV).

Moreover, the equation 9 demonstrates the beam average energy dependence on the current supplied by the power supply. The graph is shown on the figure 26.

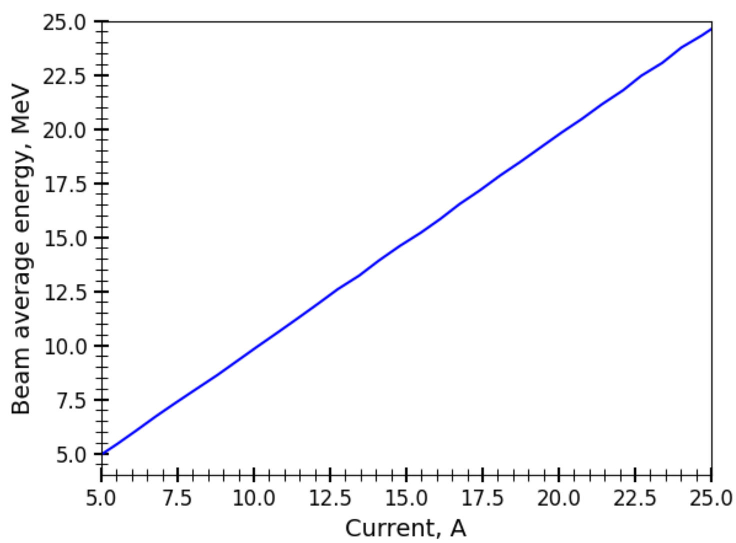

Figure 26: The beam energy vs the current supplied to the magnet coil

The calibration equation neglects the losses in the cables, the magnet cooling system instability and other factors.

According to the power supply datasheet, the current stability is 0.05% of the setup current [26]. Hence, the magnet field does not jitter, fluctuate or drift. The measurement results are not affected by the magnetic field instability. It is necessary to note that the same current stability has all power supplies for solenoid magnet, steering magnets and quadrupole magnets.

1.6.5 Beam emittance monitor

Normalized transverse emittances are measured by the Q-scan (Quadrupole-scan) method [26]. Q-scan method utilizes quadrupole magnet and scintillation screen beam profile monitor. Emittance can be calculated by measuring the beam size at the beam profile screen as a function of magnetic field strength. The monitor is installed at the "Compton Experiment IP' location (see figure 2). The emittance measurement example is presented on the figure 27.

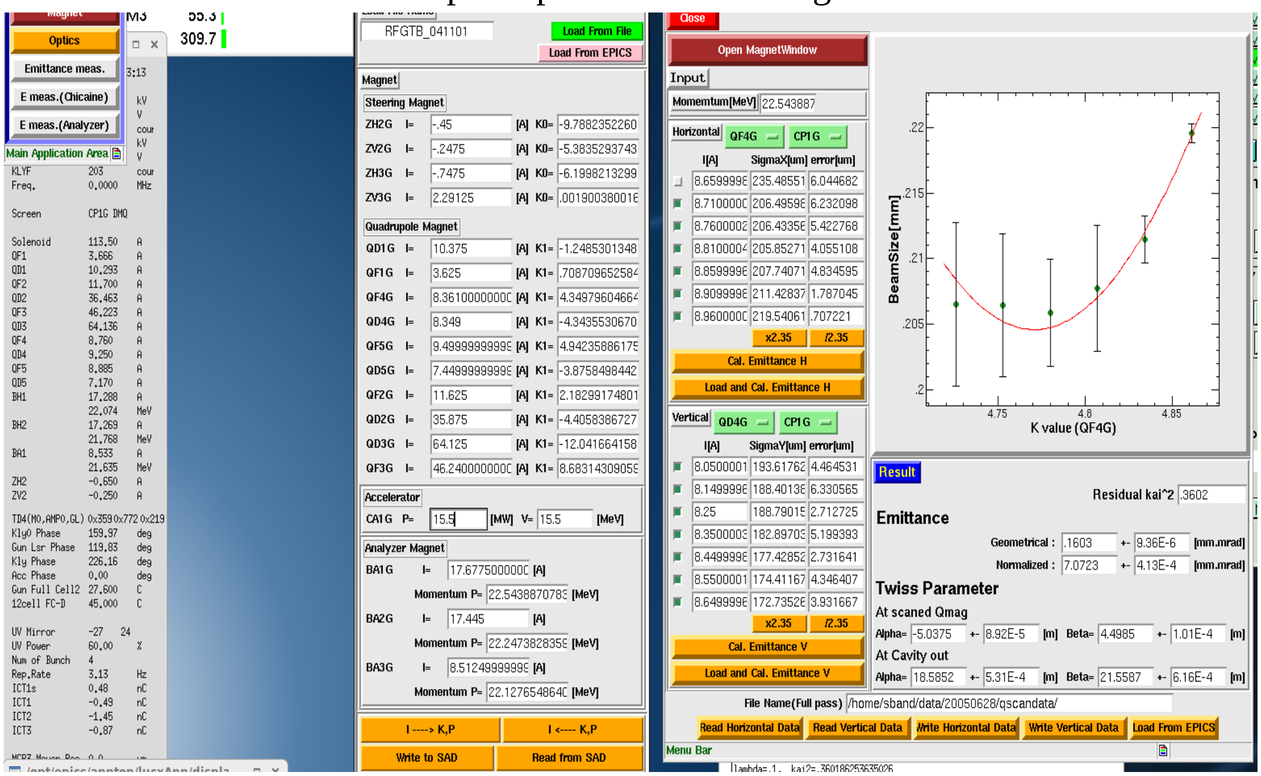

Figure 27: Example of the normalized horizontal emittance measurement by Q-scan at KEK LUCX facility

Beam emittance measurement is not pulse by pulse. The measurement usually takes from 1 to 4 minutes.

1.7 Timing system

Timing system supplies trigger signals for data acquisition system, RF-Gun laser system flash lamps, Pockels cells, klystrons, beam monitors etc. KEK LUCX facility timing system is based on the SINAP Event Generator STD-EVO and Event Receiver STD-EVE standalone modules [27]. The modules photos are shown on the figure 28 and figure 29.

Figure 28: SINAP Event Generator STD-EVO (Standalone module)

Figure 29: SINAP Event Receiver STD-EVE (Standalone module)

Event Generator is connected with Event Receiver via fiber. Event information is sent via fiber too. Timing system control is employed to EPICS IOC [22]. EPICS server is supplied by SINAP.

Only client side was programmed at EPICS Qt framework [28, 29]. SINAP EVE module rear panel channels settings setup GUI is demonstrated on the figure 30.

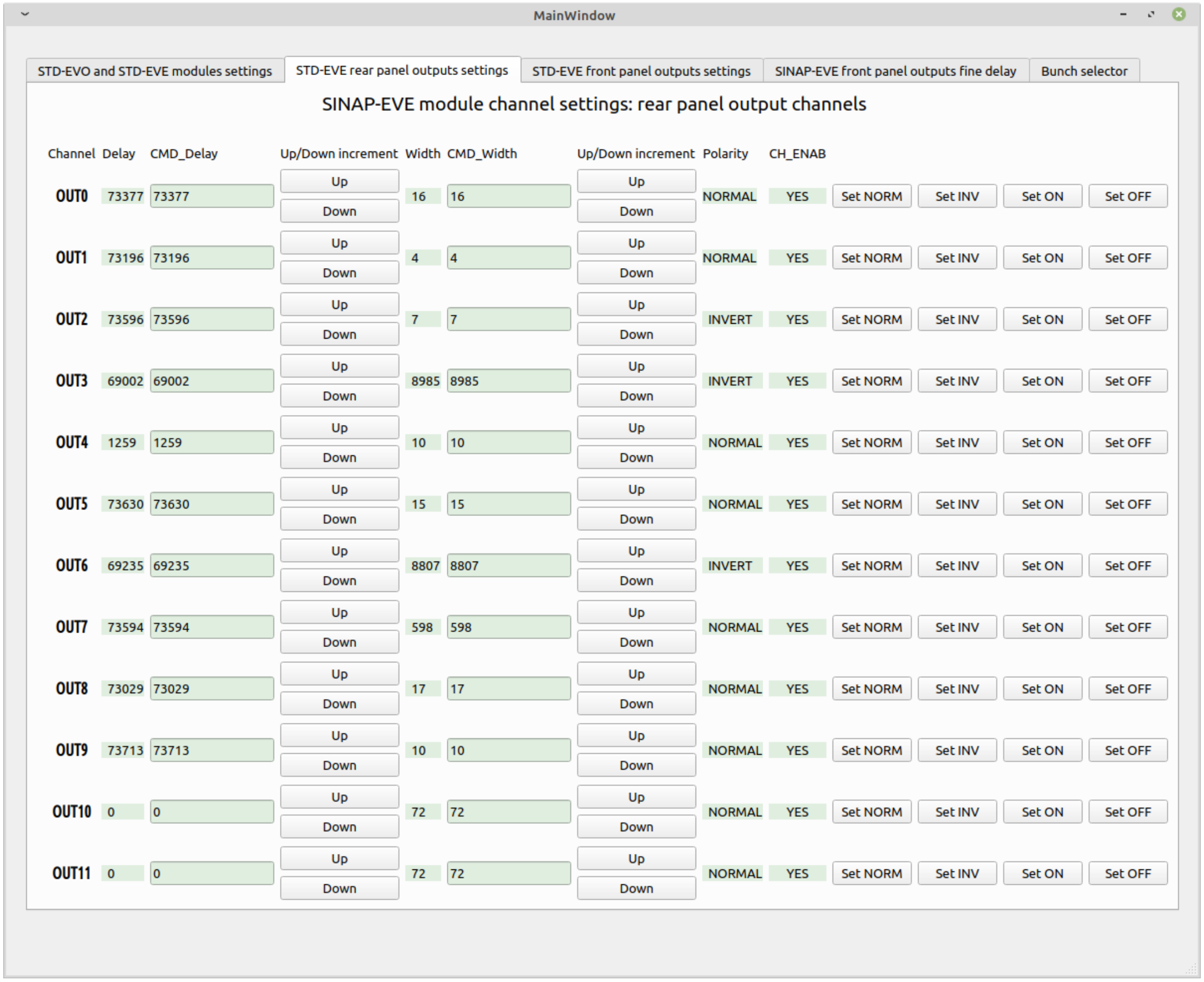

Figure 30: SINAP EVE module rear panel channels settings tab

Trigger channel output level is normal and inverted TTL. GUI controls every channel delay, width, polarity. If the channel is not used to trigger any devices at KEK LUCX facility, it will be possible to turn off the channel. Timing system connection map is presented on the figure 31.

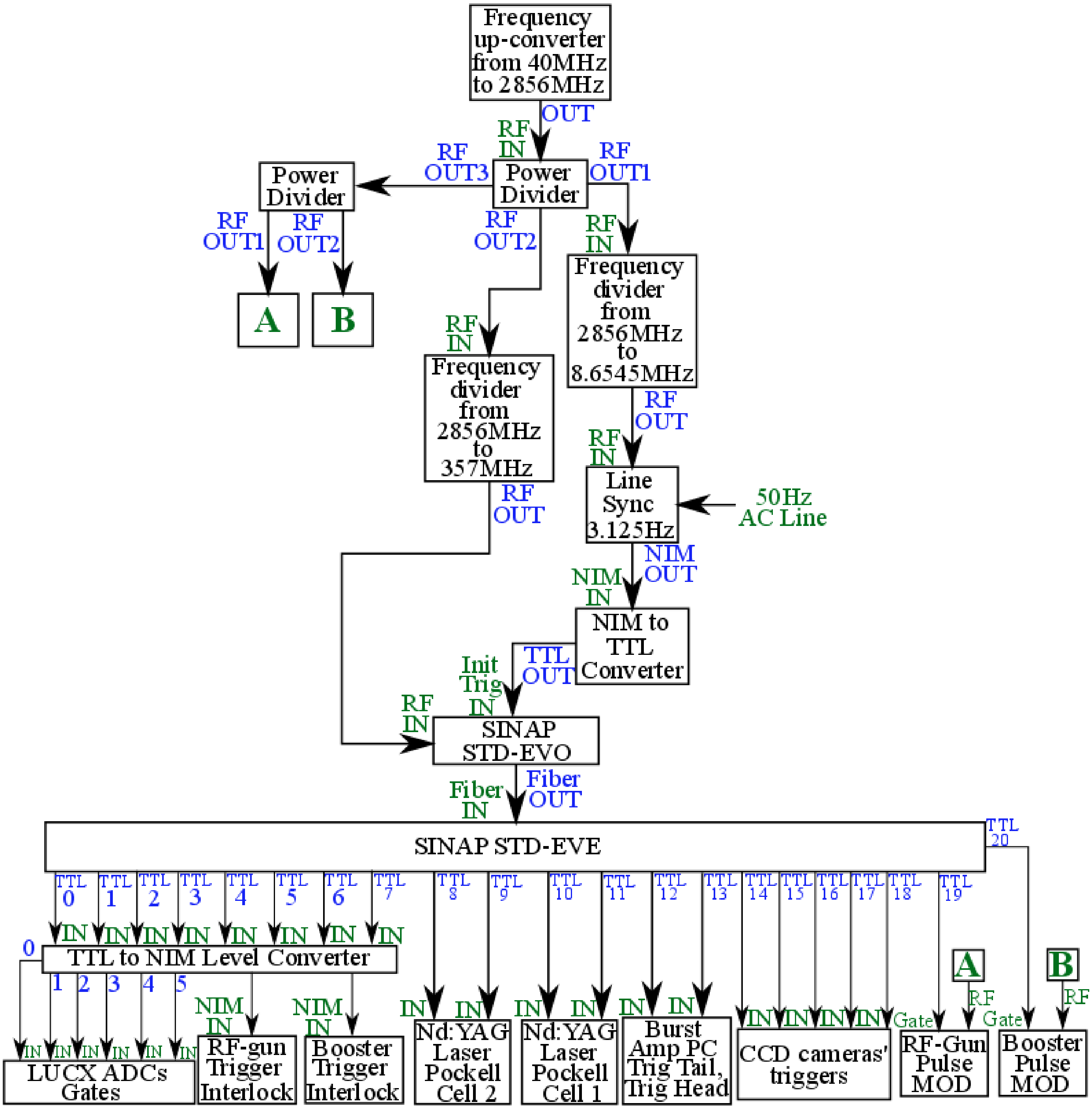

Figure 31: KEK LUCX facility upgraded timing system layout

SINAP STD-EVE supplies trigger signals for DAQ, klystrons, laser systems, interlock etc. System is compact, flexible and reliable. Facility operation is easy and friendly.

Moreover, the stability phase-locking between TTL trigger and accelerating field RF is ~20 ps (RMS). The phase-locking stability was checked with oscilloscope [30].

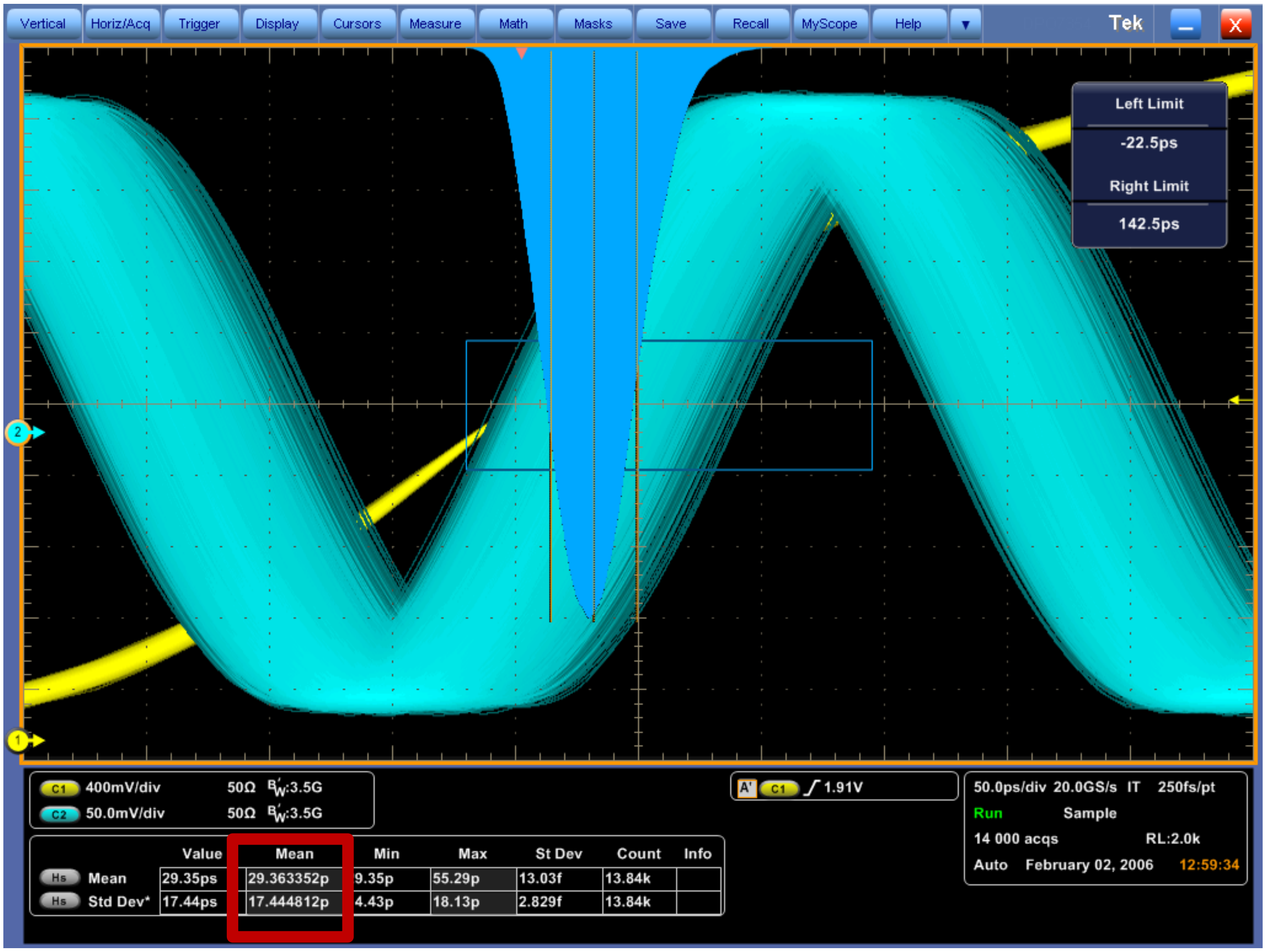

Figure 32: Timing jitter of the TTL trigger signal relative the 2856MHz signal (the oscilloscope display printscreen)

The data was measured with Tektronix DPO7354 oscilloscope [30] with 250 fs resolution (interpolation mode) and infinity persistence. So, all ~14000 traces are displayed on the printscreen. The yellow line is the digitized part of the TTL trigger. The horizontal division is 50 ps. The blue lines are 14000 traces of the 2856MHz signal. The blue box is the region of the data acquisition for the histogram plot. The histogram bin width is 250fs. The phase-locking stability is 17.5ps (RMS) (see the red box on the figure 32).

The separated histogram is demonstrated on the figure 33. The bin width was changed from 250 fs to 2 ps for the sake of visibility. Also for the visibility sake, the histogram data maximum is normalized to 1 and the histogram position is shifted from 29.3 ps to 0 ps.

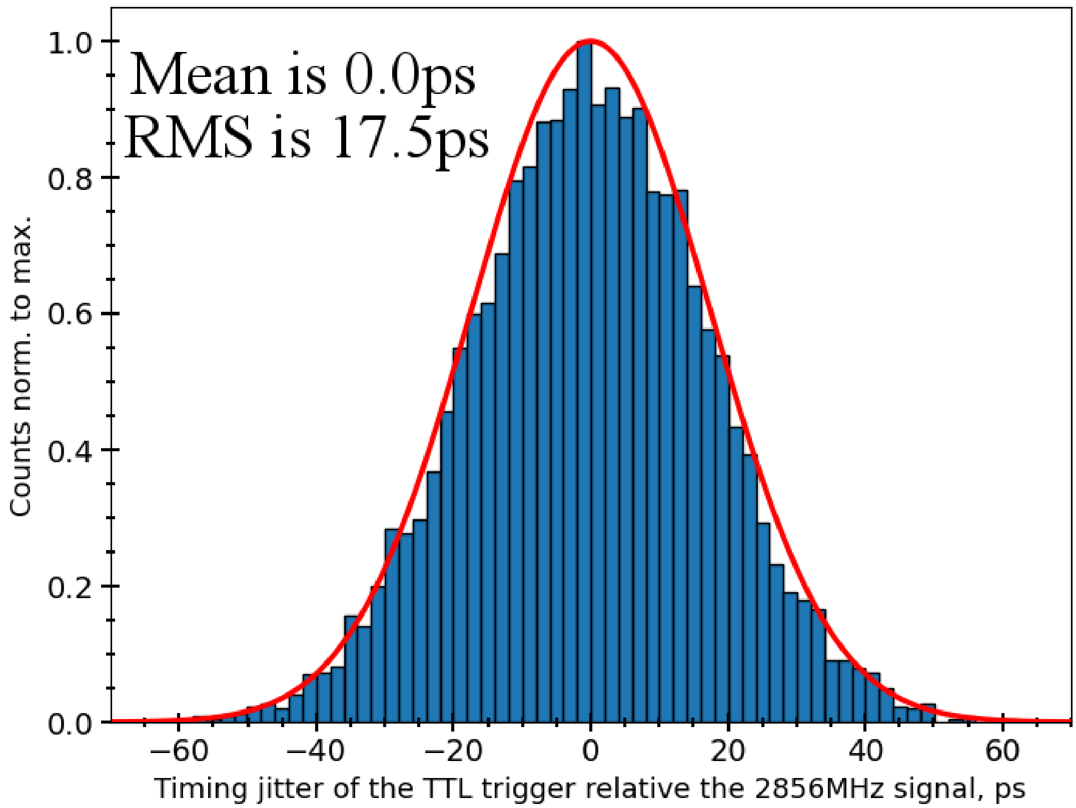

Figure 33: Timing jitter of the TTL trigger relative the 2856MHZ signal (histogram)

LUCX is a pulsed beam accelerator. Hence, this stability allows operating beam diagnostics, DAQ and feedback synchronously with the electron beam generation. The initial trigger from Line Sync is phase-locked with 2856MHz 8^{th} subharmonic (357MHz). So, the trigger signals have not any timing ambiguity. This statement is proved by the data demonstrated on the figure 32 and 33.

1.8 Control software: EPICS, Qt and EPICS Qt

KEK LUCX facility utilizes EPICS, Qt and EPICS Qt to control accelerator in real-time mode and to monitor accelerator parameters.

EPICS is the Experimental Physics and Industrial Control System. It is the set of software tools and applications used to develop and implement distributed control systems to operate devices such as accelerators, telescopes and any other large scientific and industrial facilities.

Figure 34: EPICS software label

EPICS uses client-server and publish-subscribe techniques to communicate between computers. Servers and “input/output controllers” (IOCs) collect experiment and control data in real-time using measurement instruments attached to them. Then, this information is provided to clients, using the high-bandwidth Channel Access or pvAccess networking protocols that are designed for real-time applications. Data held in the records are presented by unique identifiers known as Process Variables (PVs) These PVs are accessible over the network channels provided by the CA/pvAccess protocol. C programming language with “cadef.h” header file was used to create EPICS server side with entire EPICS functions and features. Moreover, Graphical User Interface (GUI) packages are available at Qtcreator software [31].

Figure 35: Qt programming language label

It allows viewing and interacting with PV data through typical display widgets. Furthermore, EPICS Qt is layered framework based on Qt for accessing data using Channels Access and PVAccess. It has been designed for rapid development of control system graphical user interface.

From the maintainability side, EPICS is open-source, cross-platform software with wide community of developers and maintainers. EPICS, Qt and EPICS Qt are the appropriate choices for KEK LUCX facility.

1.9 Beam optics

Electron beam is generated by Cs2Te photo-cathode irradiation. The beam is accelerated up to 7.7 MeV by RF-Gun cavity. Then it enters the solenoid. An emittance compensation solenoid is installed at an outlet of the RF-Gun. The emittance compensated electron beam passes through the first steering magnet (St1) to correct beam misalignment caused by the misalignment of the laser transport line and send the beam to the Booster cavity entrance center. The beam is accelerated up to 18 MeV–24 MeV (it depends on the user's request). After acceleration in the Booster, the beam passes the quadrupole doublet (Qd1) and the second steering magnet (St2) to match optics with final focus doublet. Hence, the final focus doublet (Qd2) focuses the beam at collision point (IP). The third quadrupole doublet (Qd3) refocus the electron beam to suppress background X-rays caused by bremsstrahlung processes and other factors. Finally, electron beam is bent by the analyzer magnet (B1), then the electron beam is guided to the beam dump after passing through an energy monitor system. The fourth quadrupole doublet (Qd4) controls horizontal dispersion η_x at the scintillator screen location. The beam line layout of the KEK LUCX accelerator (without dump section) is demonstrated on the figure 36. Beam optics was calculated by ASTRA tracking code [32].

ASTRA is A Space charge Tracking Algorithm. ASTRA tracking code is particle in cell simulation tool. Particle code represents the dynamics of the physical bunch by tracking the positions and momenta of large number N_p of simulation particles or macroparticles. It was developed for photoinjector simulations. The code utilizes the internal and external fields. The individual particles are propagated through Runge-Kutta 4^{th} order integrator [32]. ASTRA can track electron bunches from photocathode to any point at beamline.

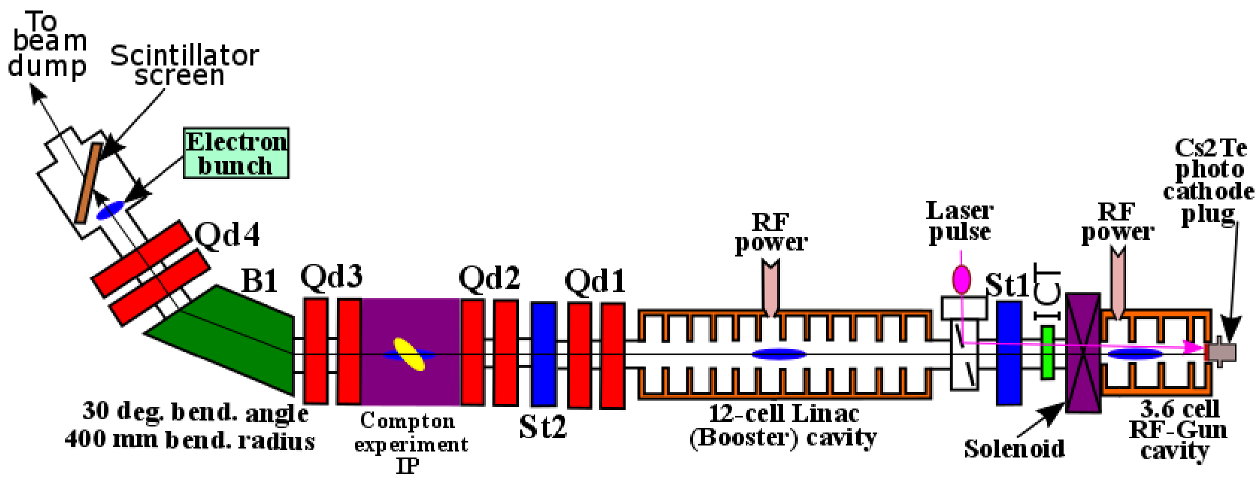

Figure 36: KEK LUCX accelerator beamline layout from photo-cathode to the scintillator screen: ICT is the integrating current transformer, St is the steering magnet, Qd is the quadrupole doublet, B is the bending magnet

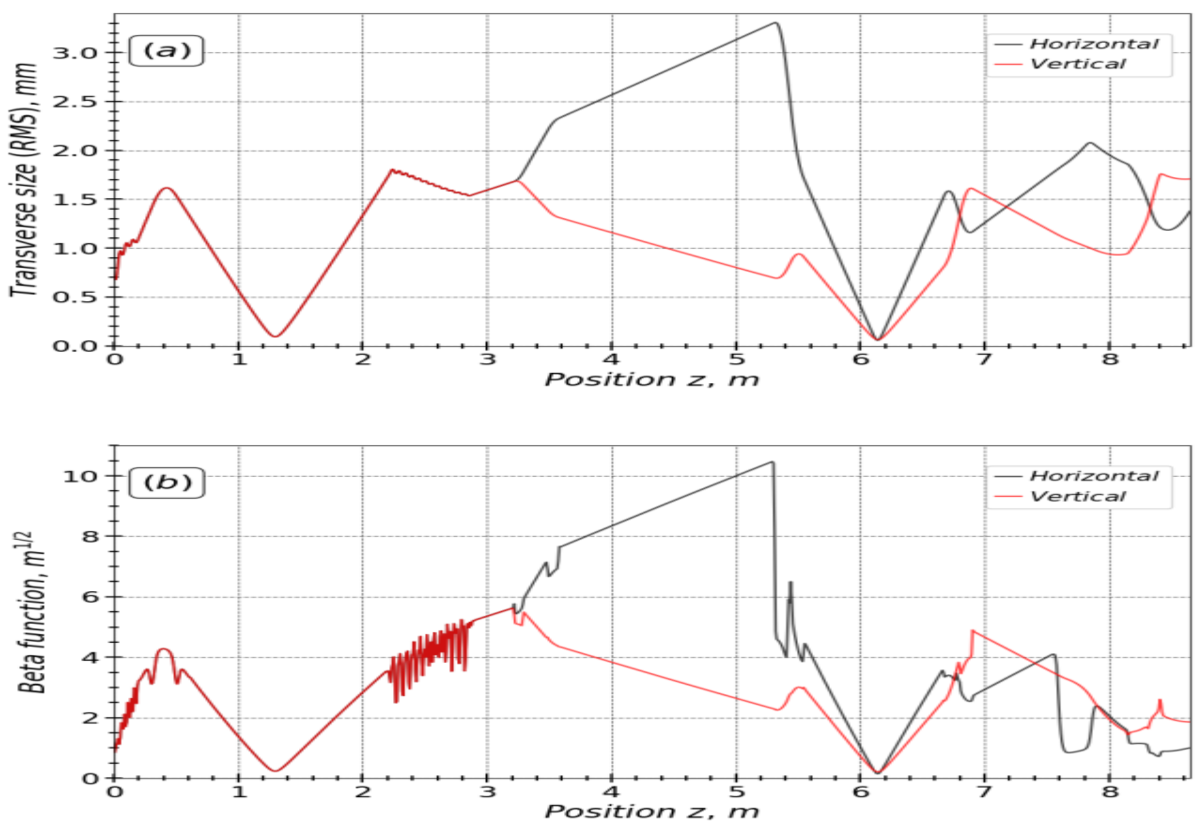

Figure 37: The beam optics calculated by ASTRA from the photocathode to the scintillator screen: (a) is the square root of the beta function vs position at beamline, (b) is the transverse beam size (RMS) vs position at the beamline

Table 1: Typical facility parameters

Characteristic	Value
Laser pulse length (RMS)	*5 ps*
Laser spot size on the photocathode: horizontal x vertical (RMS)	$800 \times 800\ \mu m^2$
Solenoid magnetic field	0.234 T
RF-Gun cavity accelerating field phase	23 °
RF-Gun cavity accelerating gradient	77 MV/m
Booster cavity accelerating cavity phase	33 °
Booster cavity accelerating gradient	44 MV/m

The input parameters of the calculation are laser pulse length (RMS), laser pulse transverse sizes (RMS) on the photocathode, RF-Gun accelerating field gradient and phase, Booster accelerating field gradient and phase and magnet optics (positions and magnet field). The beam optics calculated by ASTRA is demonstrated on the figure 37. It does not take into account steering magnets. Technically speaking, it is beam optics for the perfect orbit. Let's calculate the dependence of RF-Gun accelerating field phase on the bunch parameters (see figure 38). "RF-Gun phase" label on the figure 38 means RF-Gun cavity accelerating field phase. "Hor. Emittance" means normalized horizontal emittance. "Vert. emittance" means normalized vertical emittance. The beam parameters after RF-Gun cavity are summarized in table 2.

Table 2: Beam parameters after RF-Gun

Characteristic	Value
Bunch charge	$250\ pC$
Bunch length (RMS)	4 *ps*
Normalized transverse horizontal emittance	$2.7\ \pi\ mrad\ mm$
Normalized transverse vertical emittance	$2.7\ \pi\ mrad\ mm$
Bunch average energy	$25\ keV$
Bunch energy spread	$7.7\ MeV$

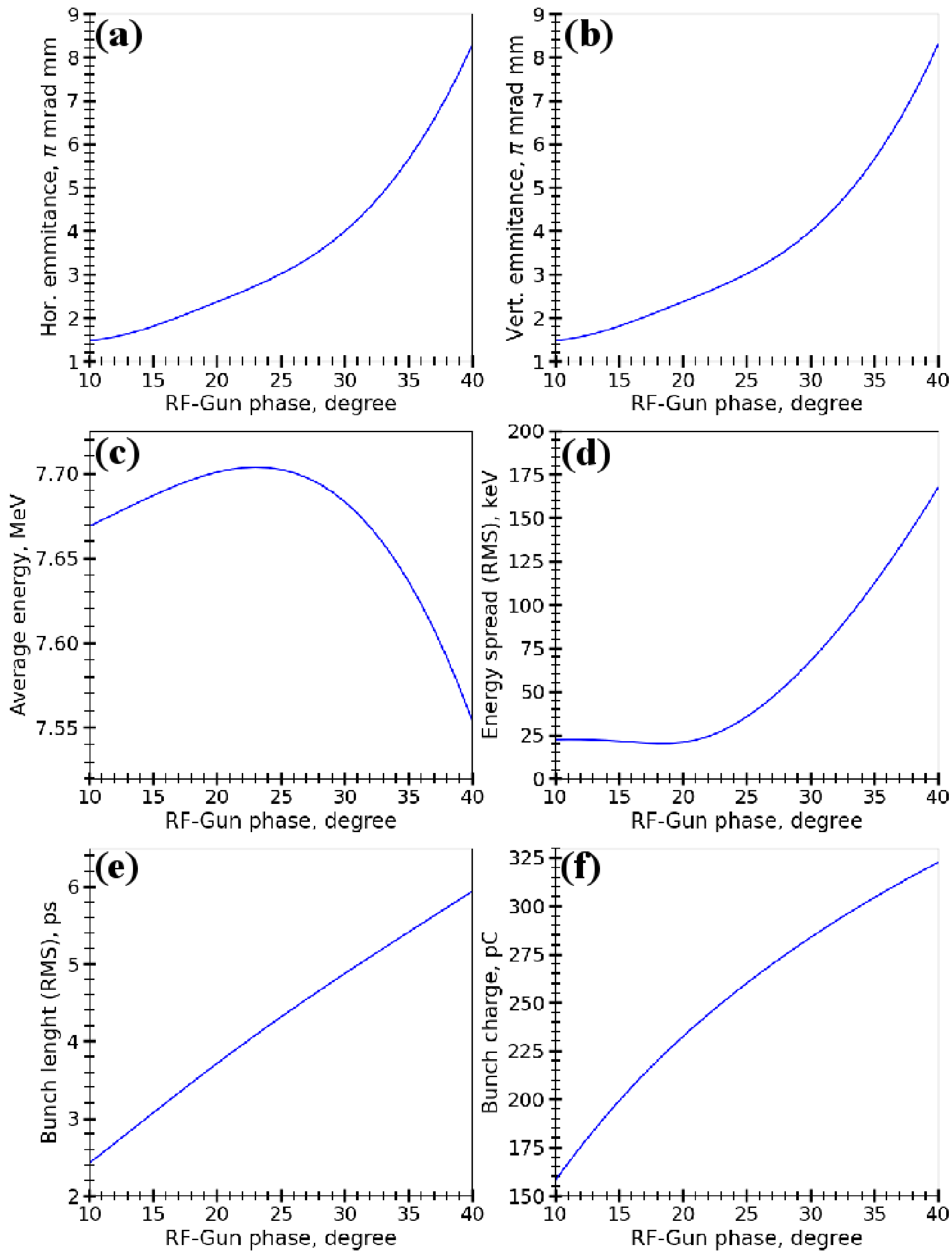

Figure 38: The electron bunch parameters dependence on the RF-Gun cavity accelerating field phase : (a) is the normalized horizontal emittance vs RF-Gun phase, (b) is the normalized vertical emittance vs RF-Gun phase, (c) is the average energy vs RF-Gun phase, (d) is the energy spread (RMS) vs RF-Gun phase, (e) is the bunch length (RMS) vs RF-Gun phase, (f) is the bunch charge vs RF-Gun phase

As can be seen from the table 2 and figure 38, the optimum phase is 23 ° , because average energy is 7.7 MeV, energy spread (RMS) is 25 keV, bunch charge is 250 pC, bunch length (RMS) is 4 ps, and normalized transverse emittance is 2.7 π mrad mm.

Let’s calculate the dependence of Booster accelerating field phase on the bunch parameters (see figure 39). “Booster phase” label on the figure 39 means Booster cavity accelerating field phase. “Hor. Emittance" means normalized horizontal emittance. “Vert. emittance” means normalized vertical emittance. The bunch parameters after Booster cavity are summarized in table 3.

Table 3: Bunch parameters after Booster

Characteristic	**Value**
Bunch charge	250 pC
Bunch length (RMS)	4 ps
Normalized transverse horizontal emittance	$3.84\ \pi\ mrad\ mm$
Normalized transverse vertical emittance	$3.84\ \pi\ mrad\ mm$
Bunch average energy	80 keV
Bunch energy spread	21.34 MeV

As can be seen from the figure 39, the optimum phase is 33 ° , because average energy is 21.34 MeV, energy spread (RMS) is 80 keV, bunch charge is 250 pC, bunch length (RMS) is 4 ps, and normalized transverse emittance is 3.84 π mrad mm. These parameters are optimum to perform laser-Compton experiment at KEK LUCX facility.

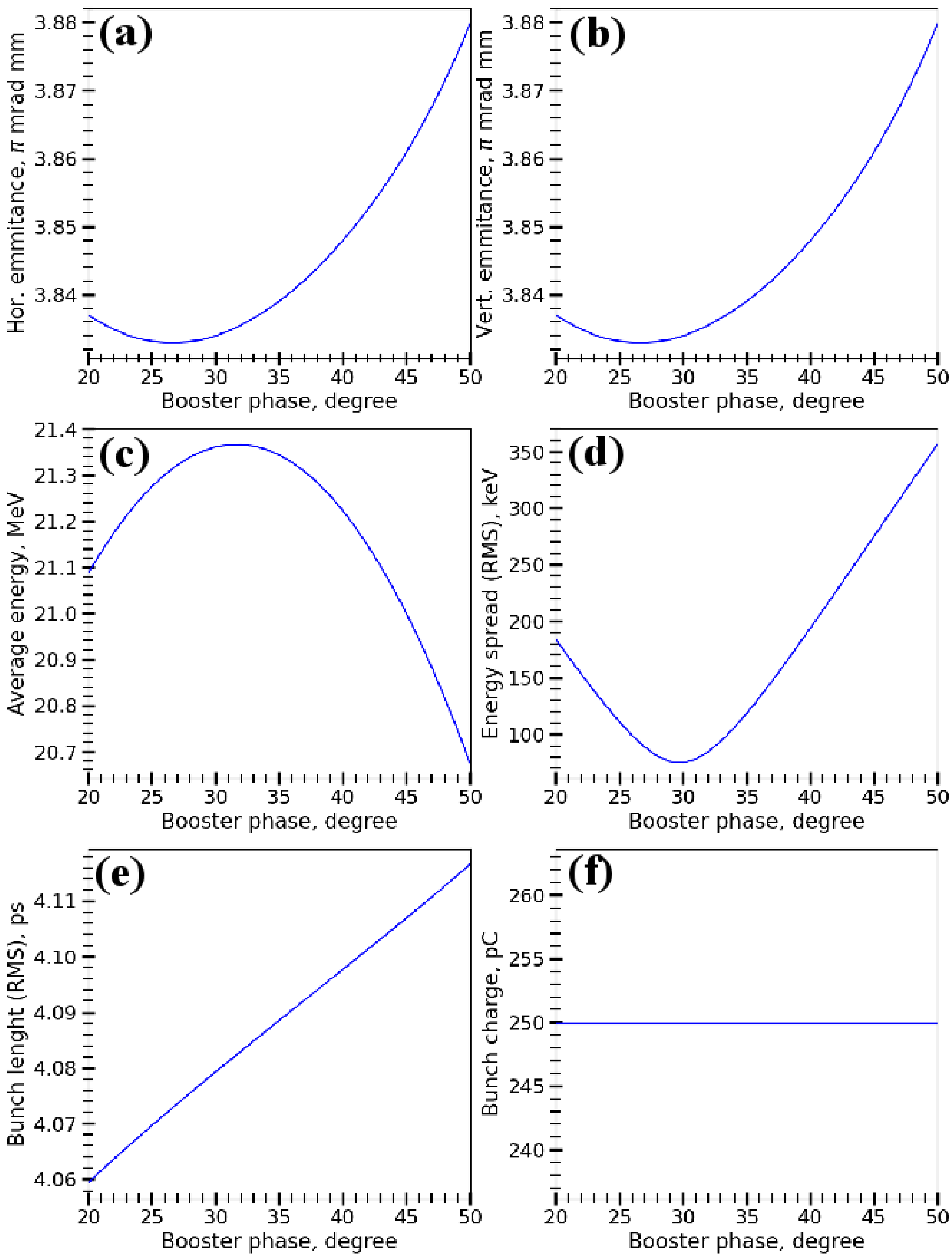

Figure 39: The electron bunch parameters dependence on the Booster cavity accelerating field phase: (a) is the normalized horizontal emittance vs Booster phase, (b) is the normalized vertical emittance vs Booster phase, (c) is the average energy vs Booster phase, (d) is the energy spread (RMS) vs Booster phase, (e) is the bunch length (RMS) vs Booster phase, (f) is the bunch charge vs Booster phase

1.10 Motivation

KEK LUCX facility is devoted to develop and operate an intense monochromatic X-Ray source based on laser-Compton backscattering phenomena for imaging and tomography applications [1-3] as an alternative to the synchrotron radiation facilitates such as KEK PF [4], Spring-8 [5], etc.

A laser-Compton backscattering phenomena is a collision between relativistic electron bunch with laser pulse. As a collision result, low energy photons became high energy photons. The energy gain depends on the laser pulse and electron bunch characteristics. The collision schematic is demonstrated on the figure 40 and 41.

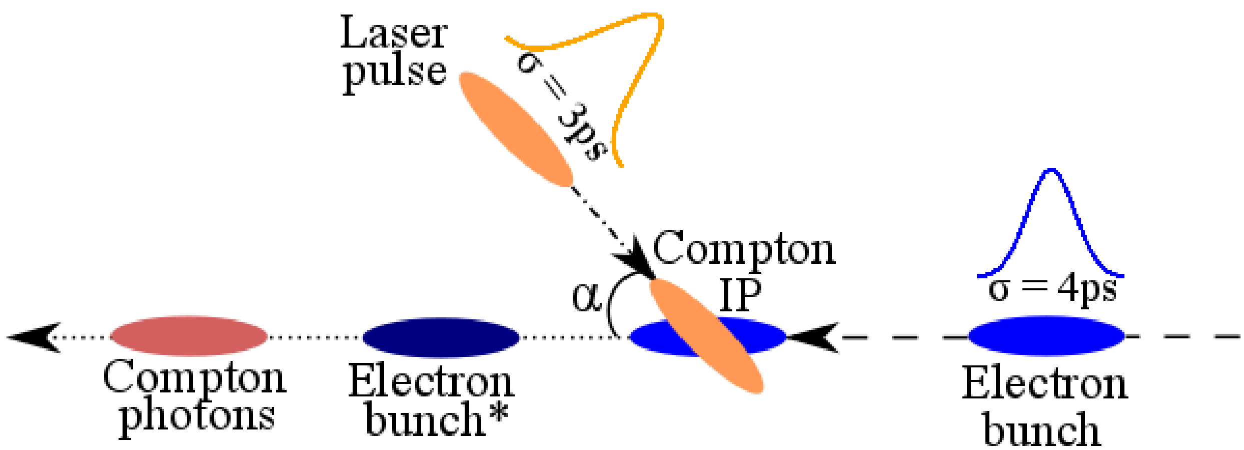

Figure 40: Laser-Compton collision schematic between electron bunch and laser pulse

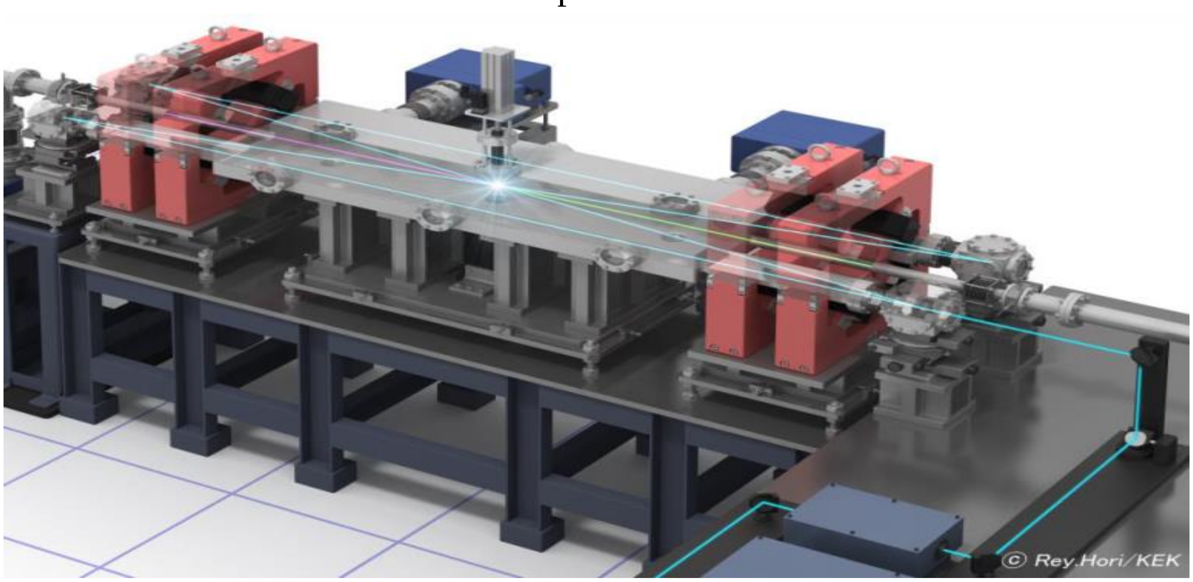

Figure 41: Illustration of laser-Compton collision scheme at KEK LUCX facility

The laser-Compton X-Ray energy equation for the head on collision [34] is:

$$E_\gamma = 4 \cdot \gamma^2 \cdot E_l, \tag{10}$$

where E_γ is the laser-Compton X-Ray energy, γ is the Lorentz factor, E_l is the laser photon energy .

The laser wavelength is 1064 nm, the electron energy is 22.5 MeV. Hence, the Lorentz factor is equal to 44. The laser photon energy is calculated using following equation:

$$E_l = h \cdot c/\lambda, \tag{11}$$

where E_l is the laser photon energy, h is the Plank constant, c is the speed of light in vacuum, λ is the laser photon wavelength.

According to the equation 11, the laser photon energy is equal to 1.2 eV. Therefore, the X-Ray energy for KEK LUCX case is 9 keV.

Another important parameter for the X-Ray imaging is the energy bandwidth, which is mainly defined by the electron bunch parameters [34]:

$$\frac{dE_\gamma}{E_\gamma} \approx \sqrt{\left(\frac{\varepsilon_n}{\sigma_x}\right)^4 + 4 \cdot \left(\frac{dE}{E}\right)^2} \tag{12}$$

where dE_γ is the laser-Compton X-Ray energy bandwidth, E_γ is the laser-Compton X-Ray bandwidth, ε_n is the transverse normalized emittance, σ_x is the transverse size (RMS), dE is the electron bunch energy spread (RMS), E is the electron bunch average energy.

According to the bunch parameters shown in the section 1.10, the relative bandwidth of the laser-Compton X-Ray energy is equal to 4 % for the RF-Gun phase at 23 ° and Booster phase at 33 °.

When the RF-Gun and Booster RF-field phase drifts, all electron bunch parameters will be changed. As a result, the laser-Compton X-Ray energy and energy bandwidth and flux will be changed too [34]. Hence, the LUCX facility RF-Gun and Booster stabilization is a milestone to generate the stable electron beam to produce highest quality laser-Compton X-Ray. The conventional way to stabilize RF-Gun and Booster is a Low-Level Radio Frequency feedback implementation.

Therefore, a digital Low-Level Radio-Frequency (LLRF) feedback was developed, implemented and tested at KEK LUCX facility for the RF field precise control.

This research investigates implementation of the FPGA board based digital LLRF feedback to stabilize accelerating field phase and amplitude inside the LUCX S-band RF-Gun and 12-cell Linac [12]. RedPitaya STEMlab 125-14 FPGA board [14] equipped with ZYNQ-7010 chip [15] was chosen for the feedback development, implementation and test at KEK LUCX facility due to competitive specifications, standalone form-factor and commercial availability. As an optimistic prediction, laser-Compton X-Ray characteristics will be stabilized for the X-Ray imaging applications.

CHAPTER 2

Commercially available FPGA board based digital Low-Level Radio-Frequency feedback implementation techniques

RedPitaya STEMlab 125-14 FPGA board was chosen and utilized for digital Low-Level RF feedback development and implementation due to the competitive specification, standalone form-factor and commercial availability. The board has two 14 bit ADCs with 125 MSa/s sampling rate, two 14bit DACs with 125 MSa/s sampling rate. Frequency bandwidth is from DC to 50 MHz. Several FPGA boards can be connected into daisy chain for synchronous acquisition of the RF signals. Digital extension inputs are used to trigger the acquisition on the external +3.3V pulse signal arrival. Digital extension inputs utilize 12 bit ADC with 100 kSa/s sampling rate.

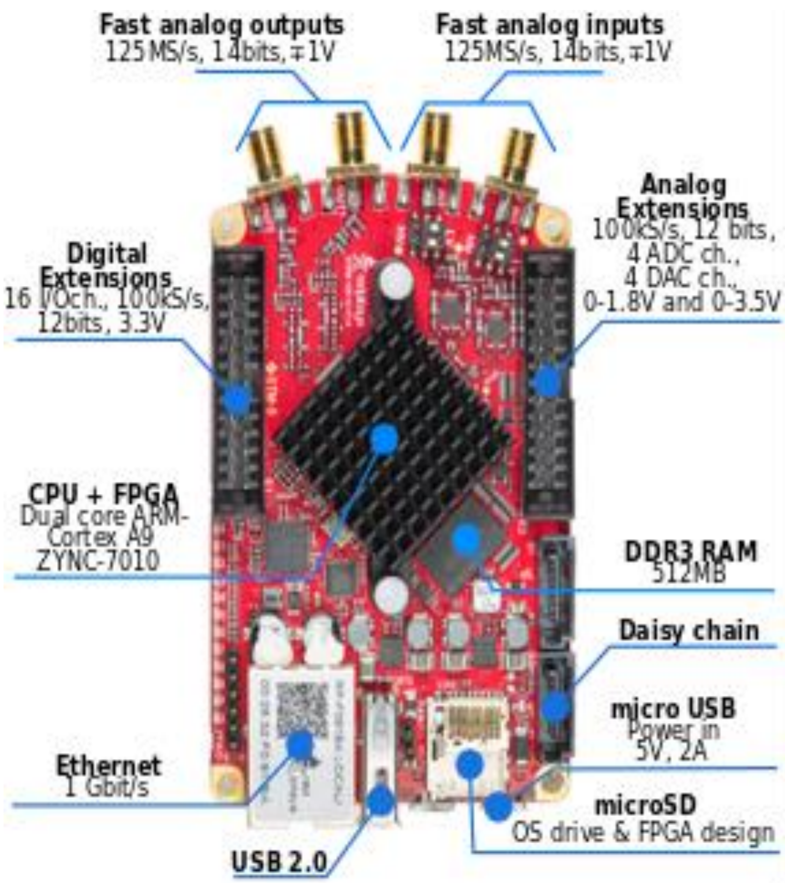

Figure 42: RedPitaya STEMlab 125-14 FPGA board

The board is equipped with ZYNQ 7010 System on the Chip (SoC), which consists from FPGA chip and ARM CPU. The FPGA chip is responsible for the programmable logic (PL), while CPU communicates with control PC and process signals in real-time.

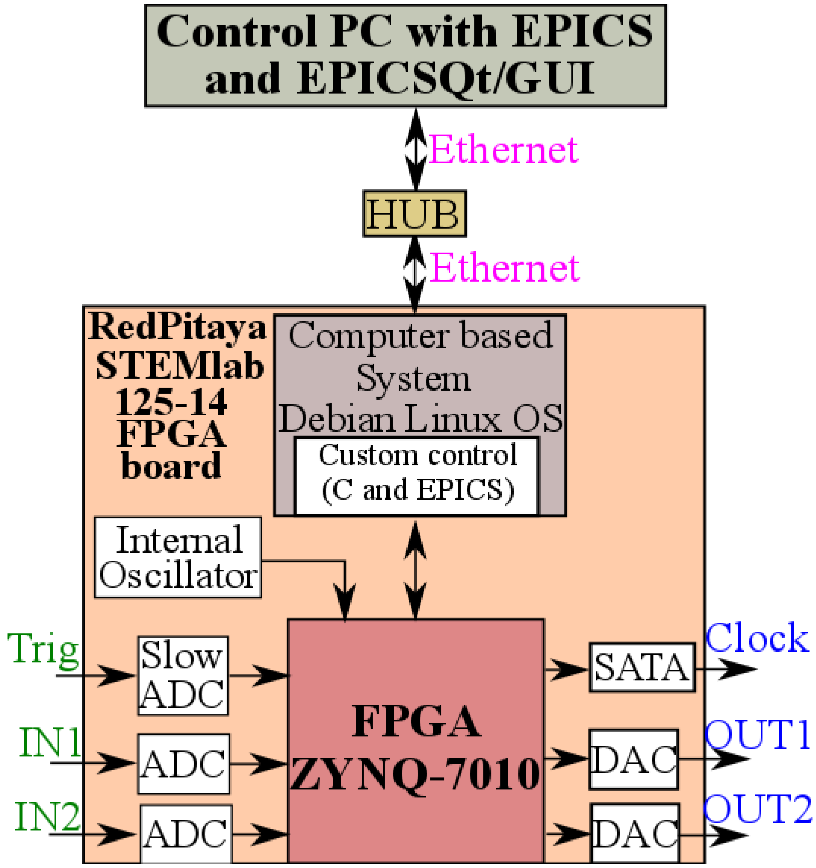

Figure 43: Communication logic between SoC and PC using EPICS IOC

The data digitized by ADC is transferred to the FPGA based programmable logic. Then, the FPGA process the signal and transfer processed data to the CPU and to DAC (see figure 43). FPGA chip transfers data to the CPU with embedded Linux OS. EPICS library implemented into the C programming code transfers data from client side to the EPICS server side at the main control PC inside the facility control room.

The board has not the external clock input. Therefore, the board firmware and entire LLRF system is phase-locked to the internal oscillator. Several FPGA board can be phase-locked in daisy-chain by sending the Master board clock via Serial AT Attachment (SATA) cable to the Slave board [33]. The connection configuration is demonstrated on the figure 44 and 45.

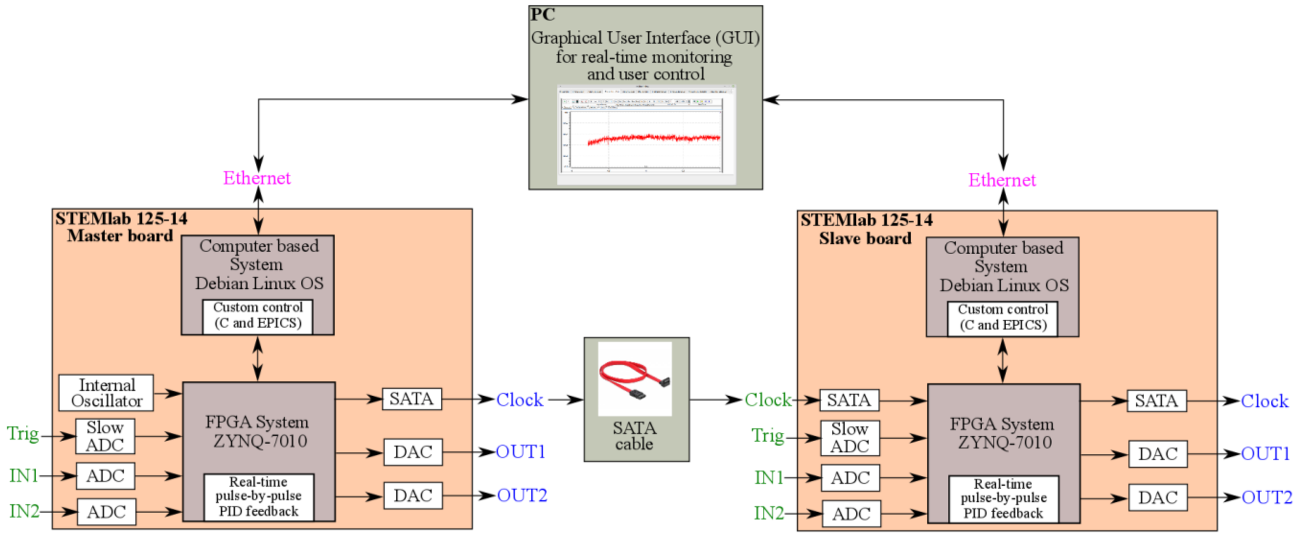

Figure 44: Daisy chain connection of two RedPitaya STEMlab 125-14 FPGA boards

SATA itself is a computer bus interface that connects host bus adapters to slave bus adapters, slave devices, mass storage devices etc. [33].

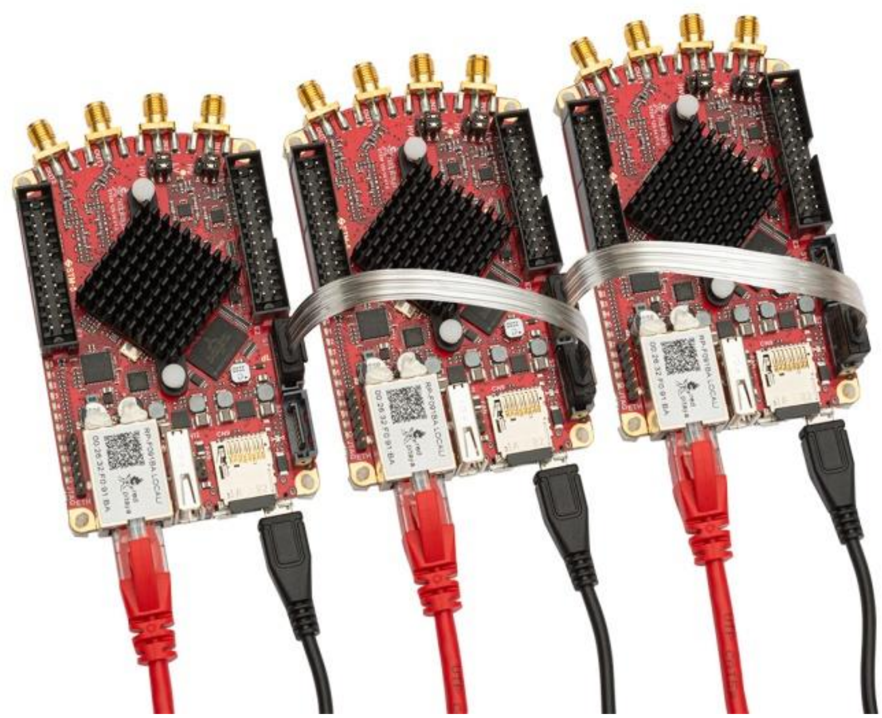

Figure 45: Connection of RedPitaya STEMlab 125-14 FPGA boards via SATA

The phase-locking stability between CW signals generated by the Master board DAC and Slave board DAC are demonstrated on the figure 46.

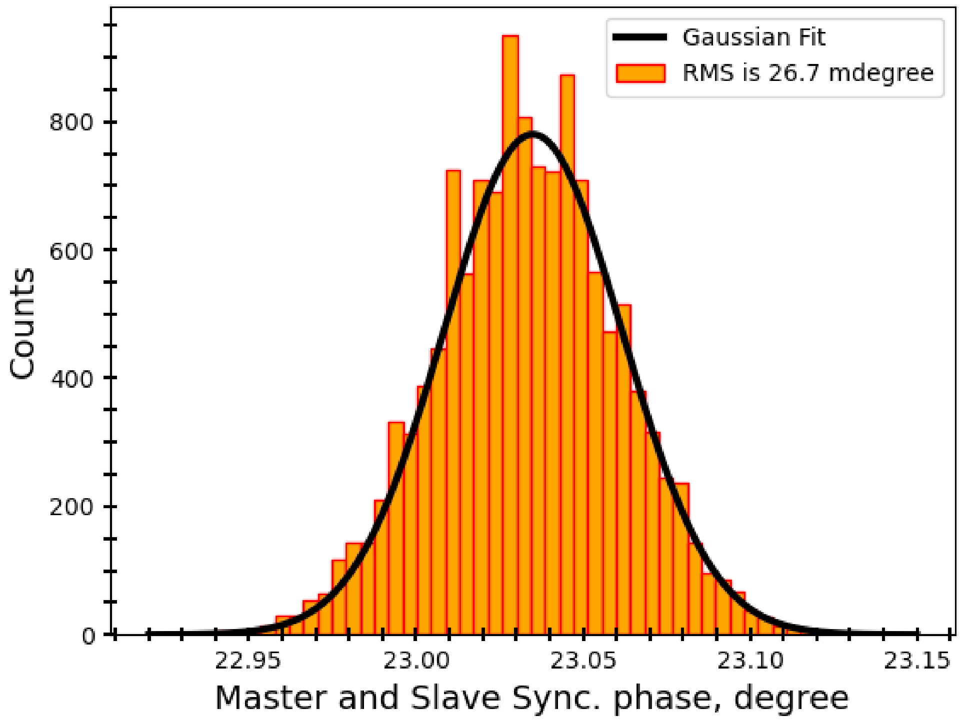

Figure 46: Synchronization stability of two RedPitaya STEMlab 125-14 FPGA boards DAC outputs

Peak-to-peak phase noise is 0.2 °. Peak-to-peak noise is difference between the maximum value and minimum value of measured data. RMS phase noise is 0.027 °. So, such stability allows connecting several RedPitaya STEMlab 125-14 boards in daisy chain to supply synchronized RF signals for the several LLRF branches at KEK LUCX facility.

Limited number of the digital LLRF feedback implementation techniques can be realized at KEK LUCX facility due to the external clock input absence at RedPitaya STEMlab 125-14 FPGA board. These techniques are described in the next sections.

2.1 In-Phase and Quadrature sampling&generation technique

In-Phase (I) and Quadrature (Q) sampling&generation LLRF technique includes the FPGA board, analogue In-Phase and Quadrature modulator, analogue In-Phase and Quadrature demodulator, Signal Generator, Pulse modulator and frequency dividers (see figure 47).

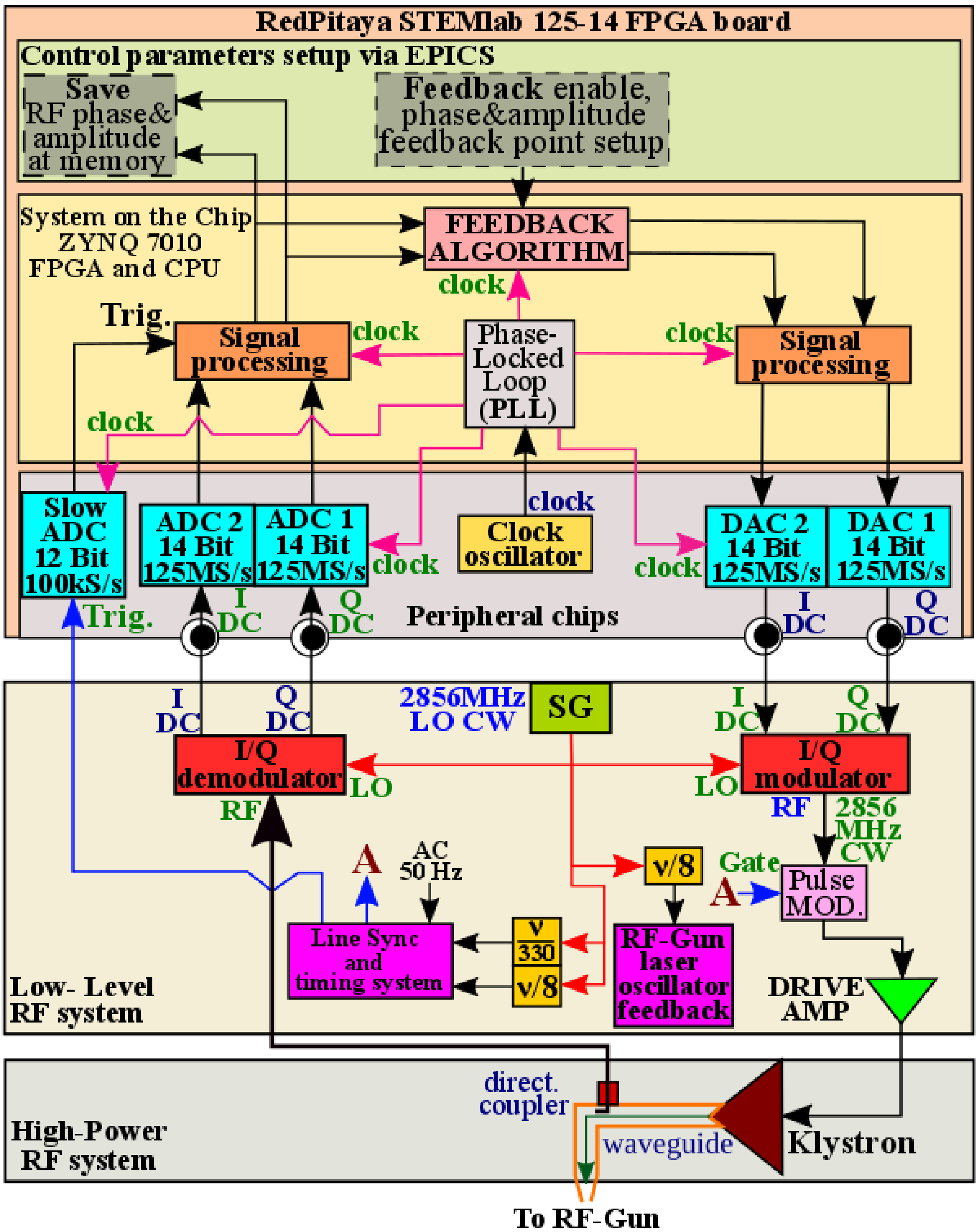

Figure 47: RedPitaya STEMlab 125-14 FPGA board based I/Q sampling&generation LLRF feedback technique implementation schematic

DC coupled ADC and DAC chips generate and digitize In-Phase and In-Quadrature DC signals, respectively. Signal generator supplies 2856 MHz CW reference signal, which is phase and amplitude modulated by I and Q signals generated by DACs. Then 2856 MHz signal is pulse modulated by the Gate signal, which is is phase-locked to the 8^{th} subharmonic of the reference frequency. The pulse modulated 2856 MHz signal is preamplified up to 700 W by the drive amplifier. At the next stage, the signal is transferred to the klystron and amplified up to 12 MW.

High-Power RF signal is transferred to the cavity. Directional couplers are installed on the waveguide system for the accelerating field precise control. Its coupling and directivity are 60 dB and 20 dB, respectively. So, the power of the picked up signal is 12 W. The power is attenuated from 12 W down to 10 mW during the signal transfer from the accelerator tunnel to control room.

Picked up forward signal is transferred to the I/Q demodulator module to the RF input. I/Q demodulator converts RF signal to the I/Q DC signals relative 2856 MHz CW reference signal.

In-Phase and Quadrature DC signals are sampled by ADC and phase&amplitude are calculated by the signal processing modules programmed inside the FPGA borad. Phase and amplitude are corrected by the feedback algorithm. At the final stage, In-Phase and Quadrature DC signals are corrected to eliminate accelerating field phase&amplitude jitter, drift and fluctuation. The analogue I/Q modulator and demodulator modules are demonstrated on the figure 49 and 50. The mathematics of I/Q modulation and demodulation is explained at the Appendix A.

Figure 48: Signal Generator photo

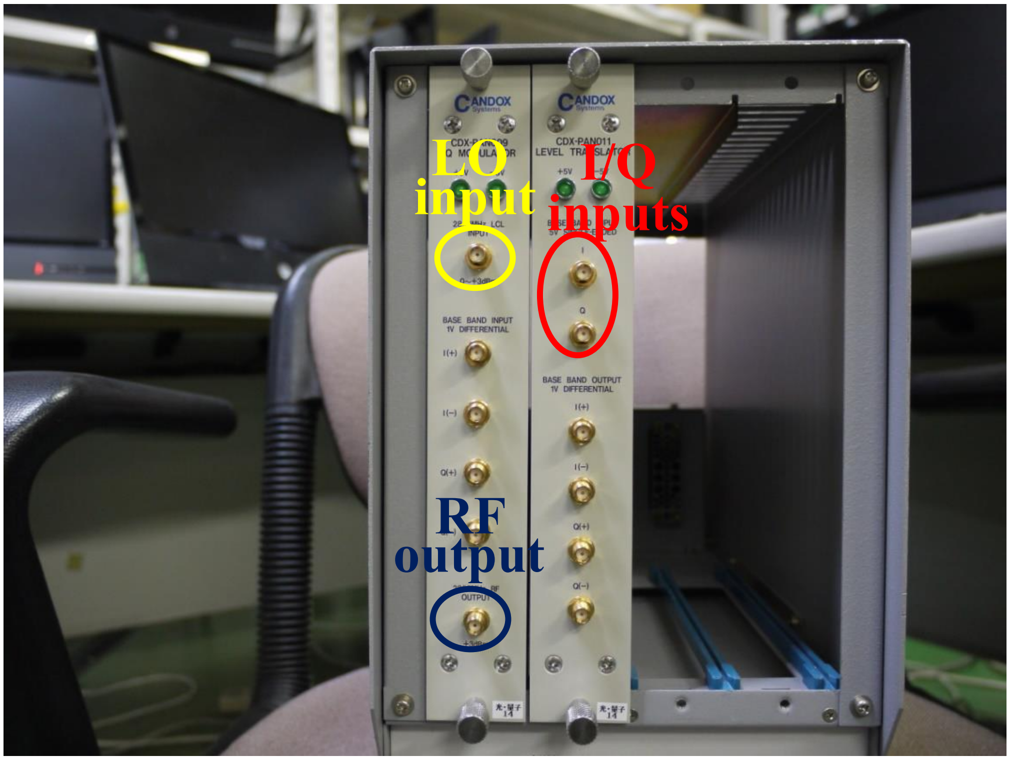

Figure 49: Analogue In-phase and Quadrature modulator

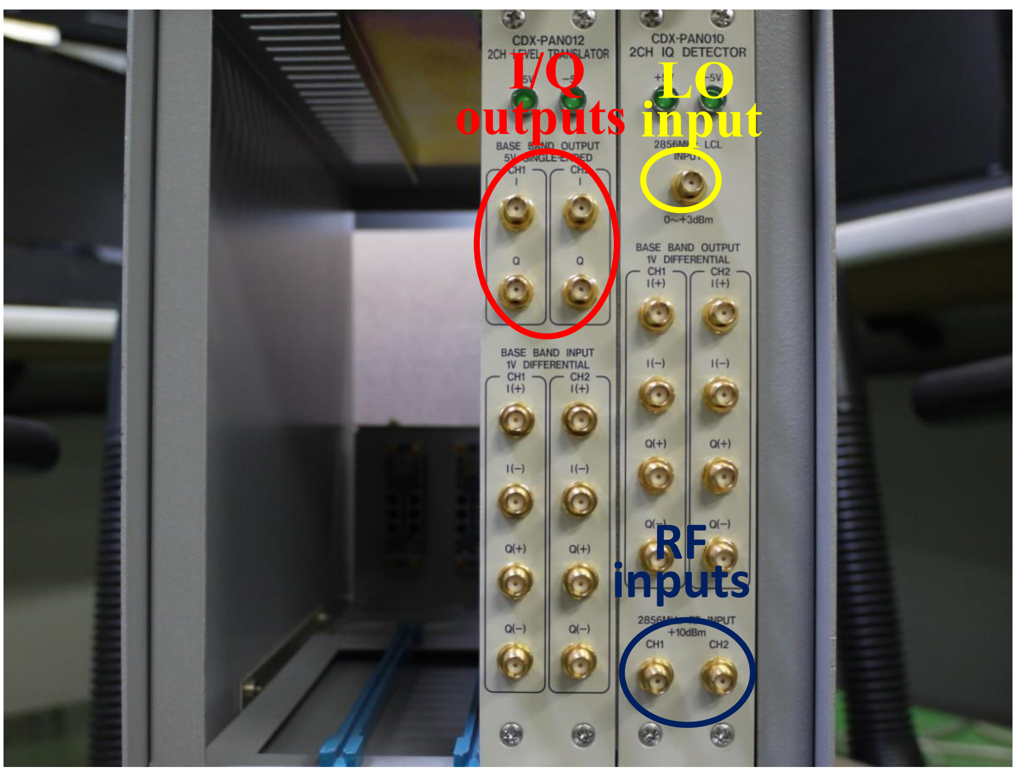

Figure 50: Analogue In-phase and Quadrature demodulator

2.2 Digital Down-Conversion&Digital Up-Conversion technique

Digital Down-Conversion (DDC)&Digital Up-Conversion (DUC) technique includes the FPGA board, the Signal Generator with preinstalled conventional 10 MHz phase-locked loop (PLL), RF-mixers, Band-Pass Filters (BPFs), pulse modulator and frequency dividers (see figure 51).

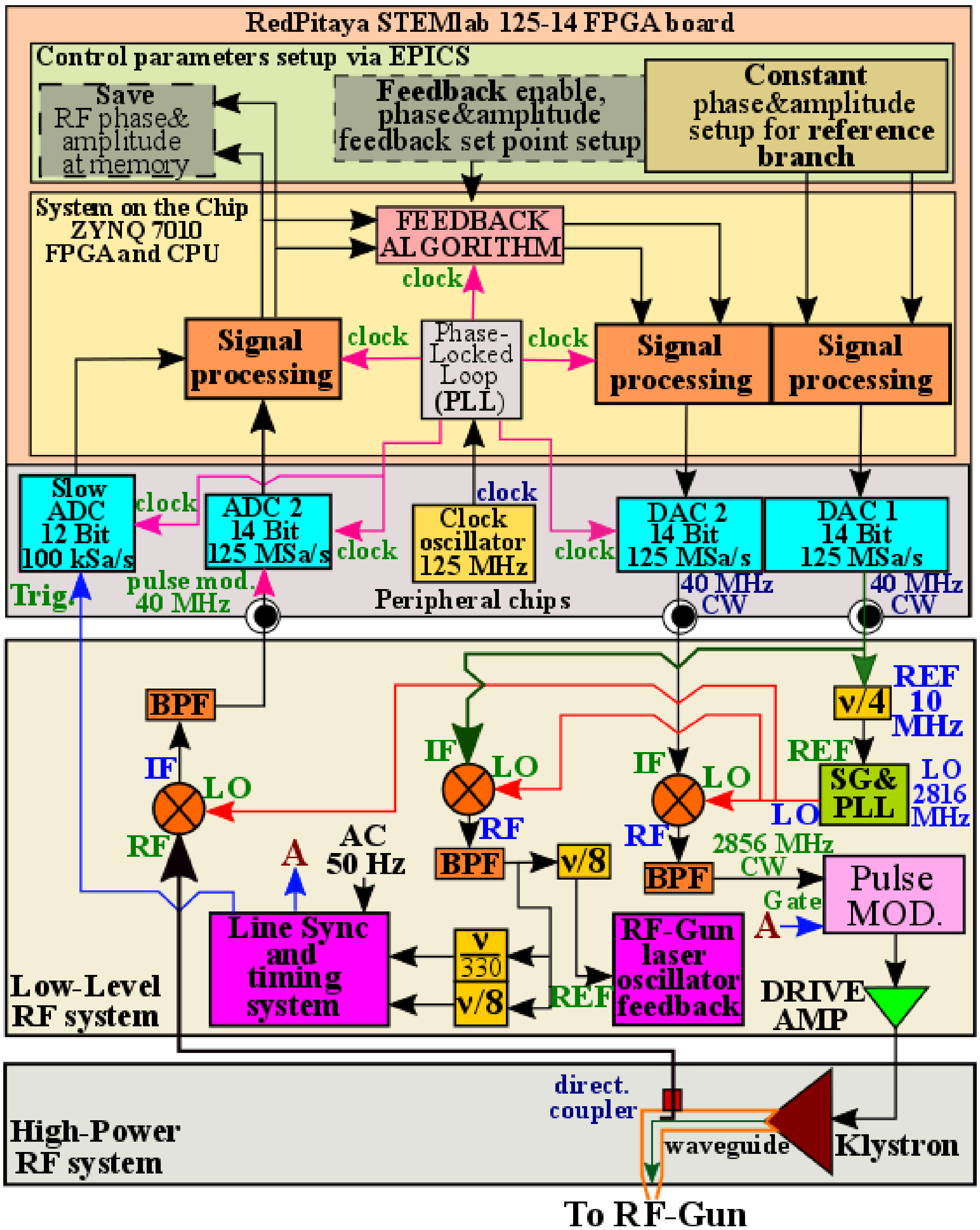

Figure 51: RedPitaya STEMlab 125-14 FPGA board based DDC&DUC LLRF feedback technique implementation schematic

The FPGA board periphery is equipped with two channels DC-coupled 14 bit ADC, two channel DC-coupled DAC both with 125 MSa/s sampling rate and additional 12 bit ADC with 100 kSa/s sampling rate. The internal crystal oscillator generates the clock for the periphery and signal processing logic. The DAC 1 output is utilized to phase-lock the FPGA board with the SG using a conventional 10 MHz PLL preinstalled at the SG [34]. The DAC 1 output generates the 40 MHz CW signal with constant phase and amplitude. The signal phase stability is 0.059 ° (RMS). The phase noise map measured by Agilent Signal Source Analyzer E5052B [35] is demonstrated on the figure 52. The phase stability is defined by the internal oscillator stability

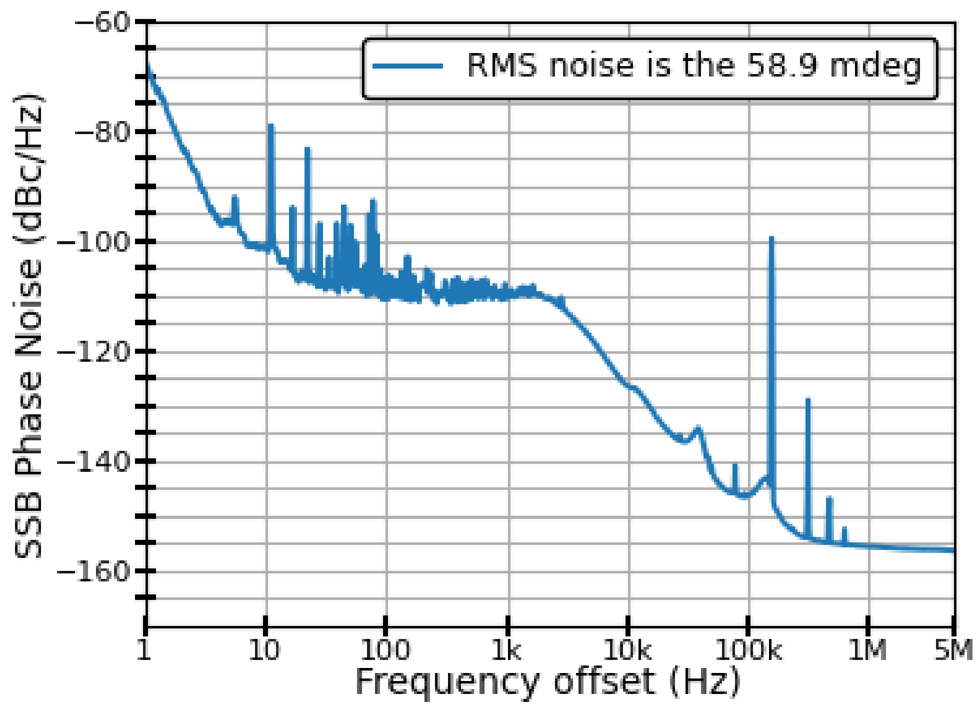

Figure 52: 40MHz CW signal phase noise map

Then, the signal frequency is divided by 4 and fed to the 10 MHz PLL input. The phase-locked SG generates 2816 MHz CW local oscillator (LO) signal for frequency up-conversion and down-conversion purposes. The DAC 2 output generates 40 MHz CW signal which is fed to the RF-miser intermediate frequency (IF) input, while 2816 MHz CW is injected to the LO input. The RF output is filtered by BPF to reject sub-harmonics occurred during the signals mixing. The resulting frequency after filtering is 2856 MHz and its amplitude and phase are controlled by DAC 2.

Then, it is pulse modulated by the gate signal generated by the timing system, which is phase-locked to the 8th subharmonic of the 2856 MHz and phase-locked to the 330th sub-harmonic of the 2856 MHz by the Line-Sync generator (Tsuji Denshi Co, Ltd). In the final stage, the RF-pulse is amplified up to 700 W by the drive amplifier (Nihon Koshuna) and supplied to the klystron (Toshiba 3729). The klystron amplifies power from 700 W to 12 MW, which is transferred to the cavity via waveguide system. The RF field directed to the cavity is picked up by directional coupler installed at the waveguide. The directional coupler directivity and coupling are 20 dB and 60 dB, respectively. The picked up RF signal is down-converted from 2856 MHz to 40 MHz by mixing with common LO and resulting IF signal is filtered by the BPF, digitized by the ADC 2, down-converted from 40 MHz to I/Q signals by DDC, processed by signal processing logic, corrected by the feedback algorithm and returned back to the LLRF system. The LLRF feedback algorithm and signal processing are implemented at the ZYNQ-7010 SoC.

The LLRF components are demonstrated on the figure 53.

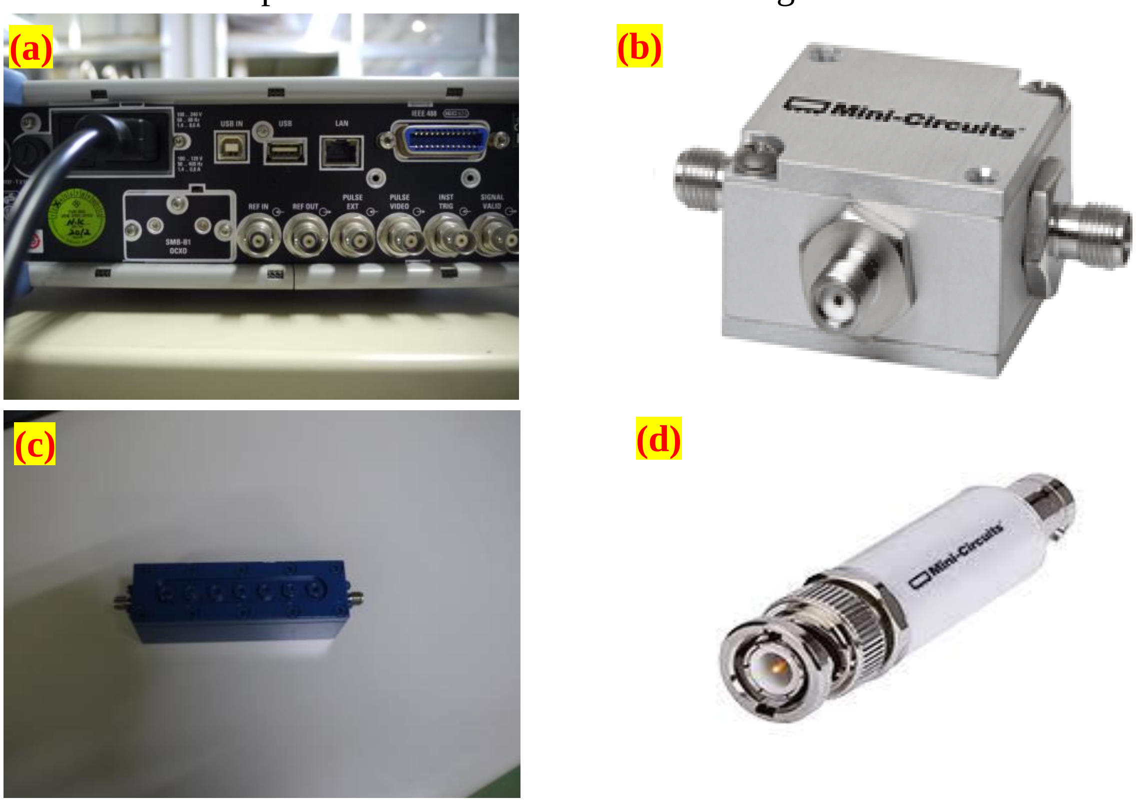

Figure 53: LLRF components: (a) is the SG with preinstalled conventional 10 MHz PLL, (b) is the RF-mixer, (c) is the 2856 MHz BPF, (d) is the 40 MHz BPF

2.3 Comparison of In-Phase and Quadrature sampling&generation technique and Digital Down-Conversion&Digital Up-Conversion technique

The comparison of the techniques and its limitations are presented at the table 4. Comparison parameters are setup flexibility, FPGA chip programing flexibility, reliability, commercial availability of the feedback components, and FPGA board synchronization with the SG.

Table 4: The comparison of the techniques limitations

Parameter	In-Phase and Quadrature sampling&generation	Digital Down-Conversion&Digital Up-Conversion
Setup flexibility	Limited by In-phase and Quadrature modulator and demodulator functions defined by company-developer	Limited by the FPGA chip Digital Signal Processing units and CPU calculation power
FPGA chip programing flexibility	Limited by the FPGA chip Digital Signal processing units and CPU calculation power. Programming flexibility depends on the FPGA programming skills of the user.	Limited by the FPGA chip Digital Signal processing units and CPU calculation power. Programming flexibility depends on the FPGA programming skills of the user.
Reliability	Depends on the quality of external I/Q modulator and demodulator. High temperature influence on the analogue electronics and RF cables. So, electronics circuits temperature stabilization is required.	Depends on the quality of the FPGA board printed circuit board (PCB) and peripheral chips quality: ADC, DAC, crystal oscillator etc.
Commercial availability of the components	I/Q modulator and demodulator are custom made components.	All components are commercially available.
FPGA board synchronization of with SG	Not required	Required for frequency up- and down-conversion

The Digital Down-Conversion&Digital Up-Conversion feedback implementation technique is limited only by the FPGA programming skills of the user, FPGA chip Digital Signal Processing units and CPU calculation power. The world-wide FPGA programming community is developed and maintained by students, engineers, professors etc. So, it is easy to find necessary information about FPGA chip programming at forums and web-sites [36]. While, FPGA board based LLRF feedback technique with analogue front-end is limited by quality of external I/Q demodulator and modulator modules. Moreover, analogue electronics is affected by the temperature and humidity. So, from long-term operation point of view, the less analogue components are utilized in LLRF feedback, the long-term operation will be more stable.

Finally, the DDC&DUC technique utilizes commercially available hardware and RF-components. So, the maintenance becomes easy and friendly. In case of any component breaking, it is possible to purchase the components from the shelf within the short time. The I/Q sampling&generation technique uses the custom-made I/Q demodulator and modulator modules developed by small electronics companies which need several months to produce the modules, so the fast repair of the LLRF system is not possible.

According to the written above reasons, the FPGA board based DDC&DUC LLRF feedback implementation technique was chosen for this research.

CHAPTER 3
Firmware

The main idea behind the FPGA board based digital Low-Level Radio Frequency feedback is to sample the IF signal, make necessary digital signal processing to get In-Phase and Quadrature DC signals, calculate phase&amplitude, correct the signal phase&amplitude and return the corrected IF signal back to the LLRF system.

3.1 Signal processing and feedback algorithm

A firmware design with IF signal datapath between ADC 2 and DAC 2 was developed at the ZYNQ-7010 SoC FPGA and feedback algorithm at SoC CPU using the Verilog hardware description language [37] and Vivado Design suite [38]. The figure 54 shows the datapath and the signal processing logic. The common clock signal generated by the 125 MHz oscillator is shared to ADC, Slow ADC, DDC, feedback algorithm, DUC and DACs.

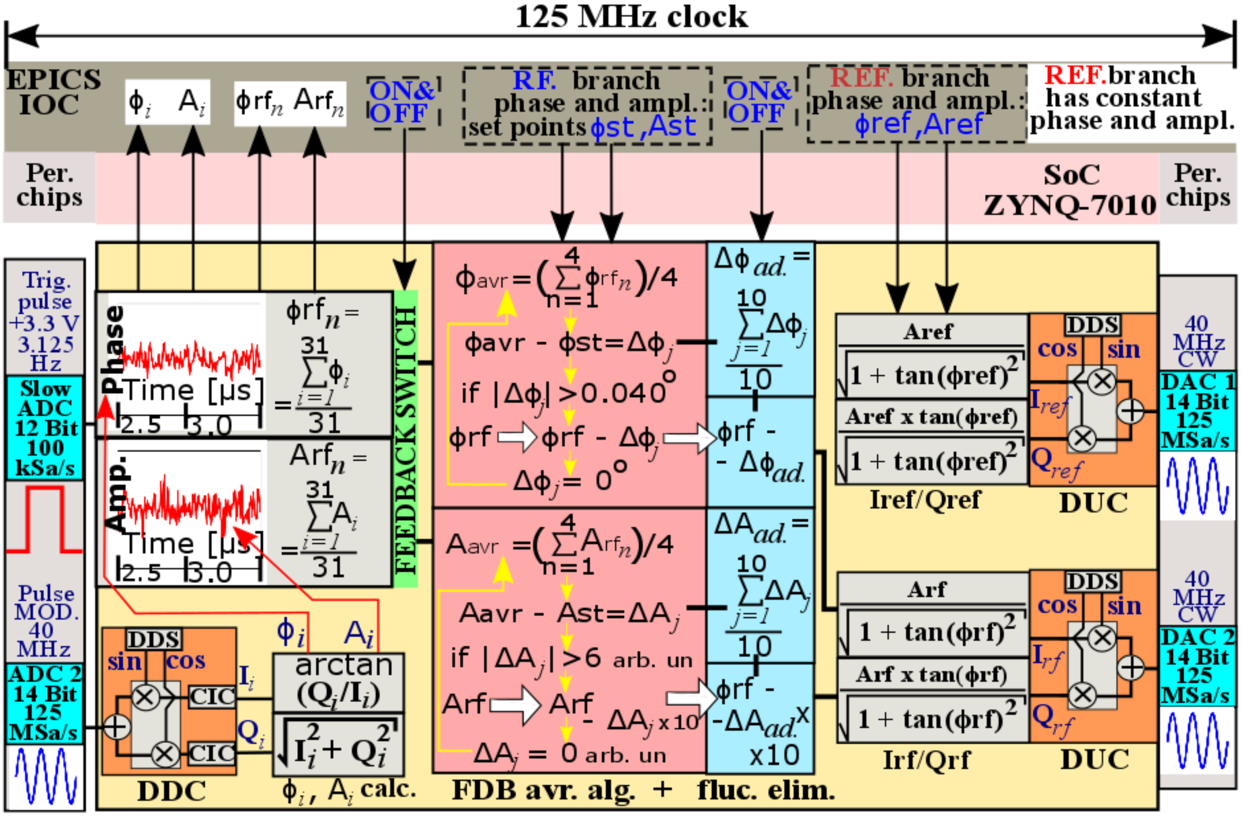

Figure 54: Block diagram of the signal processing and feedback algorithm implemented into the RedPitaya STEMlab 125-14 FPGA board

Therefore, signal digitizing&generation and signal processing are phase-locked to one clock oscillator. The ADC 2 digitizes the pulse modulated 40 MHz signal with 125 MSa/s sampling rate to get 500 digital data points. The IF signal pulse length is 4 µs. Then, the data is transferred to the DDC, which consists of the digital divider [39], Direct Digital Synthesizer (DDS) [40], complex multiplier [41] and two Comb Integrated Compiler decimation filters (CICs) [42]. The decimation factor is 4. The DDS supplies sine and cosine data for the multiplication with the samples. The multiplied signals are filtered by CICs (see the mathematical explanation in Appendix B). As a result, the dataset with 125 Q_i and 125 I_i is directed to the next stage. The i^{th} sample phase φ_i and amplitude A_i are calculated using the equation 1 and equation 2.

$$\varphi_i = \arctan(Q_i/I_i), \tag{12}$$

where φ_i is the i^{th} sample phase, Q_i is the i^{th} sample In-Quadrature component, I_i is the i^{th} sample In-Phase component.

$$A_i = \sqrt{{Q_i}^2 + {I_i}^2}, \tag{13}$$

where A_i is the i^{th} sample amplitude.

As a result, the phase and amplitude distributions inside the 4 µs picked up RF pulse are calculated. These distributions for RF-Gun and Booster pulses are demonstrated on the figure 55 and 56. The pulses have the 1 µs rise time, ringing caused by a superposition between RF power from the cavity and the forwarded RF power to the cavity, and a stable region with 1 µs duration (see figure 55 and 56). The stable regions are used for the electron beam acceleration, its φ_i and A_i are averaged over 31 points from the trigger pulse rising edge arrival. The average values are considered as RF pulse phase φ_{rf_n} and amplitude A_{rf_n}. φ_{rf_n} and A_{rf_n} are transferred to the averaging feedback algorithm logic ("FDB avr."), which consists of the two independent sides: phase and amplitude. The phase algorithm averages 4 consequent RF pulse phases φ_{rf_n} and compares it φ_{avr} with the set point φ_{st} externally set via EPICS variable. If the difference appear to be more than the phase RMS jitter inside the stable region, which is 0.040 ° (see figure 55 and 56), the is shifted at the difference value $\Delta\varphi_j$. Otherwise, the RF pulse phase and amplitude detection loop repeats.

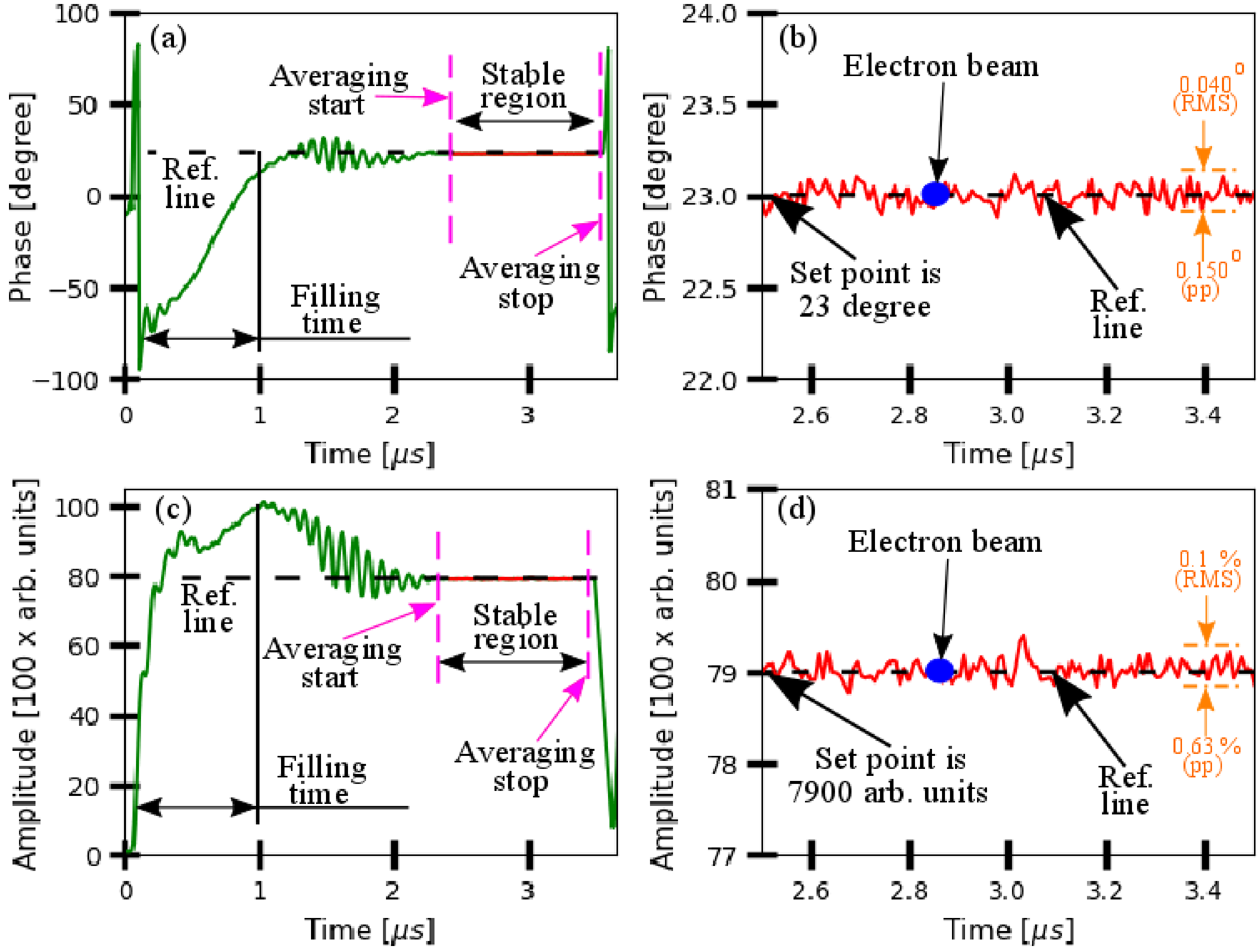

Figure 55: RF field waveforms: (a) and (b) are the RF-Gun accelerating field phase and zoomed in stable region, (c) and (d) are the RF-Gun accelerating field amplitude and zoomed in stable region

The feedback amplitude side has an identical logic, except the amplitude shift. If detected amplitude difference is more than 6 arb. units, the amplitude difference ΔA_j is multiplied by 10 due to the RF-mixer (see figure 51) amplitude non-linearity. When the phase and amplitude are shifted, the I_{rf} and Q_{rf} are calculated (see Appendix B), multiplied with sine and cosine generated by DDS and finally, the multiplied signals are summed up. The 40 MHz CW signal with corrected phase and amplitude is generated by the DAC 2 between the 4th and 5th RF pulse cycle. The RF pulse repetition rate is 3.125 Hz.

Synchronously with the averaging algorithm logic, the fluctuation elimination algorithm ("fluc. elim.") averages 10 consequent phase and amplitude corrections $\Delta\varphi_j$ and ΔA_j and applies an additional corrections $\Delta\varphi_{ad}$ and ΔA_{ad}. The additional correction values updates every 10 correction cycles. The entire feedback algorithm does not require tuning or pre-operation routine. It just requires φ_{st} and A_{st} setup.

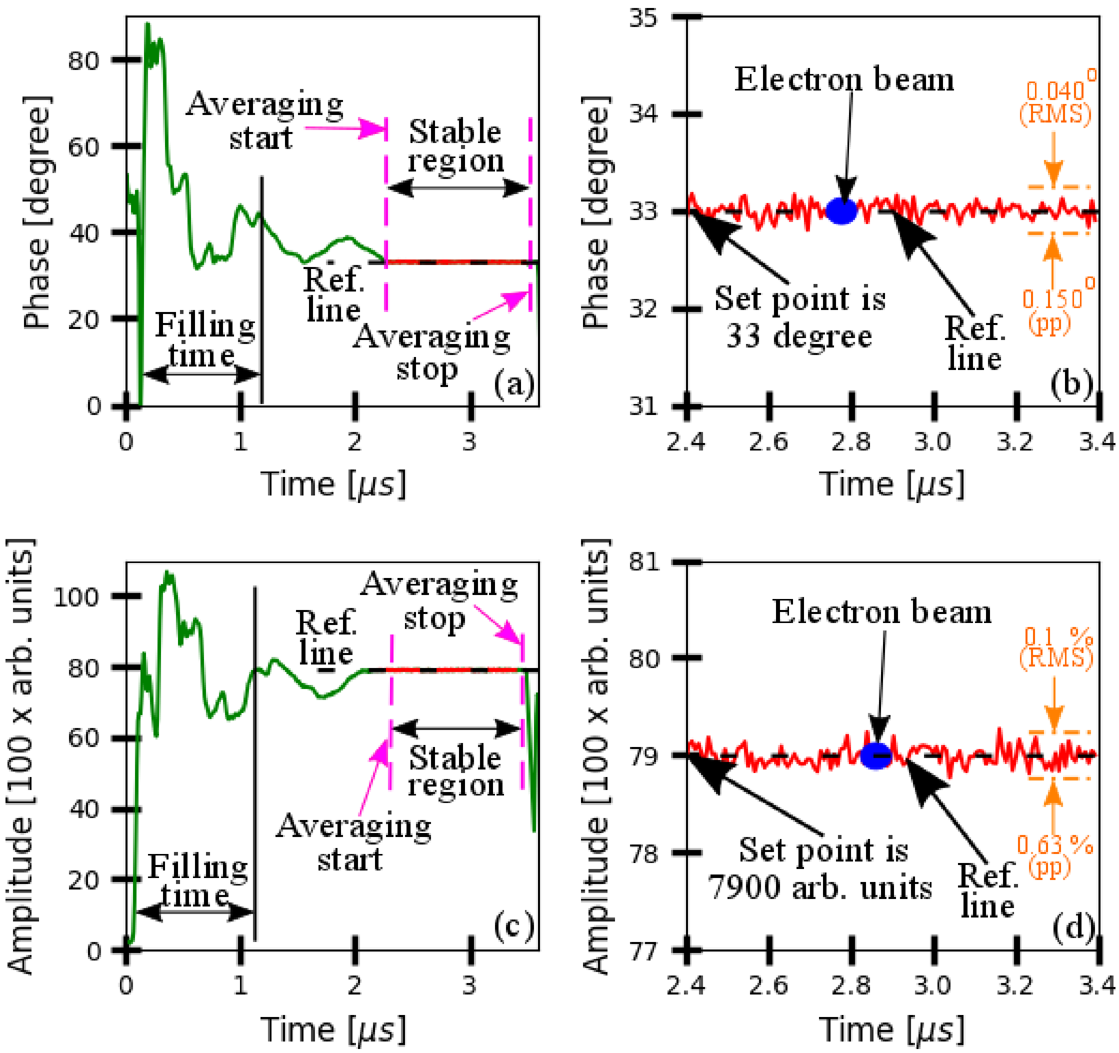

Figure 56: RF field waveforms: (a) and (b) are the Booster accelerating field phase and zoomed in stable region, (c) and (d) are the Booster accelerating field amplitude and zoomed in stable region

The DAC 1 is not included into the feedback loop as it is utilized to generate 40 MHz CW with the constant phase φ_{ref} and amplitude A_{ref} to phase-lock the FPGA board and SG crystal oscillators to generate stable LO signal for frequency up-conversion and down-conversion purposes (see chapter 2.2).

3.2 Real-time monitoring system

Real-time control system based on the EPICS IOC was implemented at the FPGA board CPU, which is responsible for the phase&amplitude monitoring, the feedback control (see figure 54 and 43). The entire feedback or its parts can be disabled upon the user request via the control panel programmed at the EPICS Qt framework. As an example, the RF-Gun accelerating field phase monitoring tab is demonstrated on the figure 57.

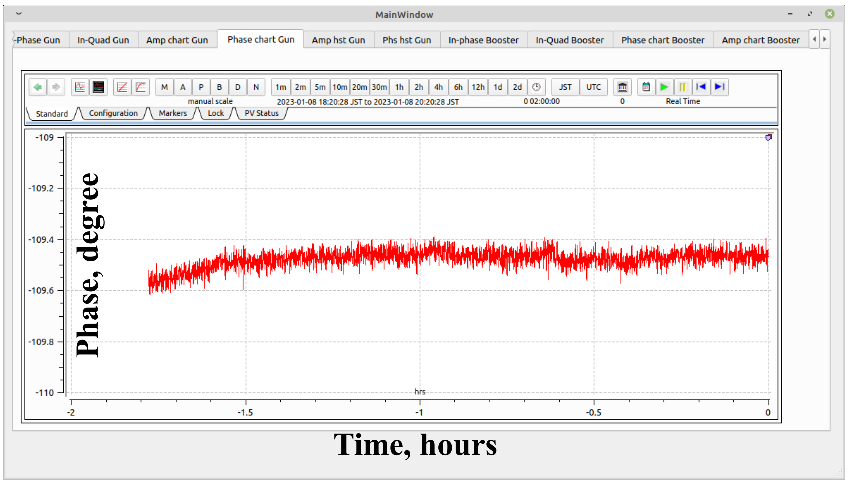

Figure 57: RF-Gun accelerating field phase monitoring tab

The monitoring is continuous. The chart is updated every 320ms (every machine cycle). Therefore, any phase instability or RF system fail is monitored in real-time during the facility operation. Moreover, real-time histogram plot (see figure 58) is implemented into the GUI.

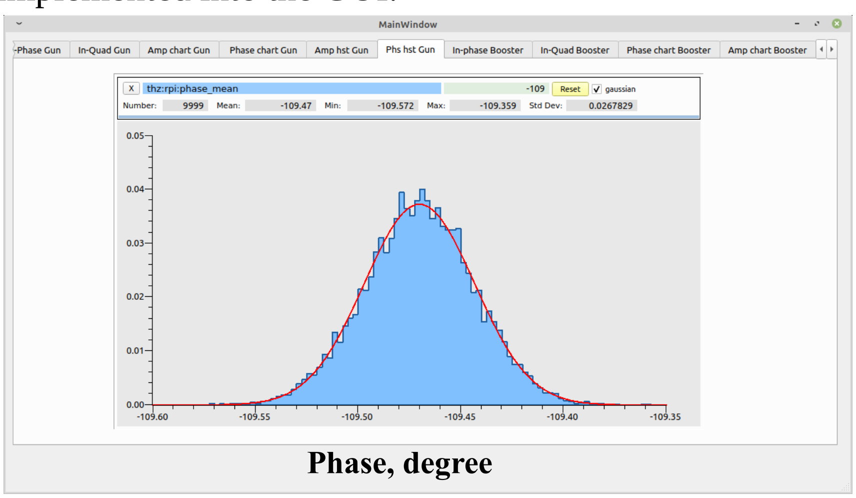

Figure 58: RF-Gun accelerating field phase monitoring tab (histogram)

The histogram itself, RMS and peak-to-peak noise are updated every machine cycle too. The histogram plot can be restarted upon the user request.

CHAPTER 4

Phase setup and detection firmware part performance test on the test-bench

Low-Level RF system based on the FPGA board requires the system features verification on the test-bench. Hence, several test-benches were assembled to measure phase setup&detection linearity performance, while the feedback was disabled.

4.1 40 MHz signal phase detection linearity check

A test-bench setup was created to check 40MHz CW signal (IF) phase detection linearity (see figure 60). DAC 1 generates the 40MHz CW signal. The signal frequency is divided 4 times and fed to the Signal Generator (SG) and the Arbitrary Waveform Generator (AWG) conventional preinstalled 10 MHz PLLs to phase-lock FPGA board crystal oscillator with SG and AWG crystal oscillators. SG and AWG photos are shown on the figure 59.

The SG generates the phase-locked 40MHz CW signal. *The signal phase shift is default function inside the SG*. The AWG generates +3.3V pulse signal for the FPGA board external trigger input to start acquisition on the pulse rising edge arrival. The pulse is phase-locked with the SG and the FPGA board.

The test-bench setup schematic is demonstrated on the figure 60.

Figure 59: Hardware used at 40 MHz signal phase detection linearity check test-bench: (a) is the Agilent 33500B Arbitrary Waveform Generator, (b) is the Rohde&Schwartz SMB 100A Signal Generator

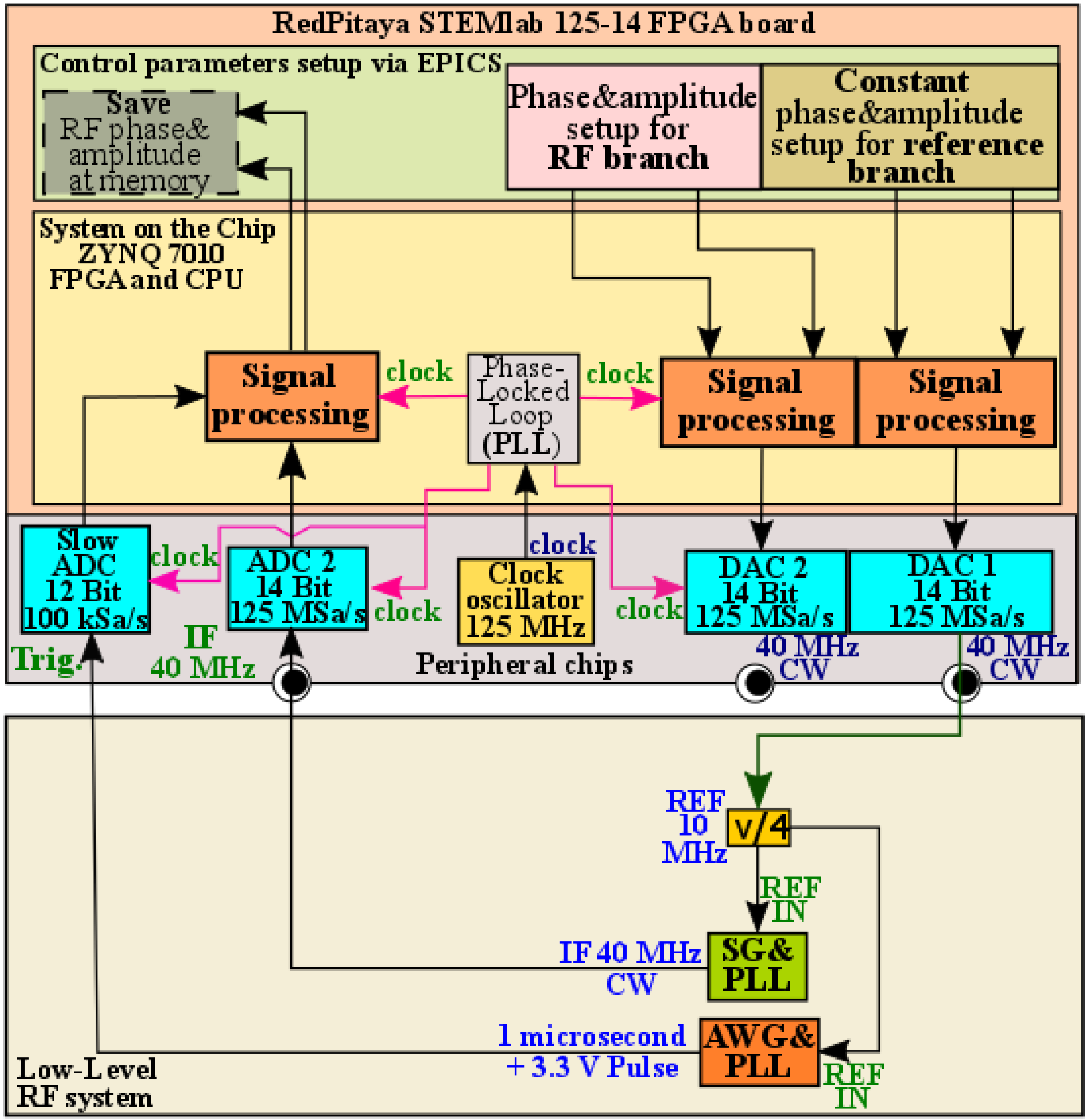

Figure 60: 40 MHz CW signal phase detection linearity measurement setup

The IF signal phase was shifted using the conventional preinstalled “phase shift” function inside the SG. Minimum step of the phase-shift is 0.010 °. Phase was shifted to certain delta. Then, it was detected by the FPGA board. Measurement results are demonstrated on the figure 61.

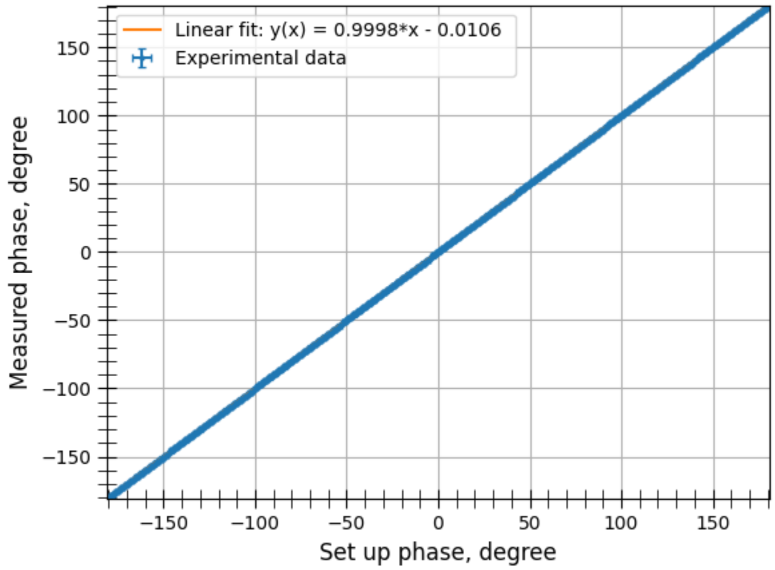

Figure 61: Phase detection linearity measurement results

Phase detection resolution is 0.044 ° (RMS). The error bar width demonstrated on the figure 61 is 6·RMS for the sake of visibility. The phase detection range is 360 °: from -180 ° to +180 °. The zoomed in region from -10 ° to +10 ° is demonstrated on the figure 62. The measured data was fitted with linear dependence. The fit amplitude and slope are $-0.011 \pm 0.001\,°$ and 0.998 ± 0.001, respectively. The line lies within the detection resolution.

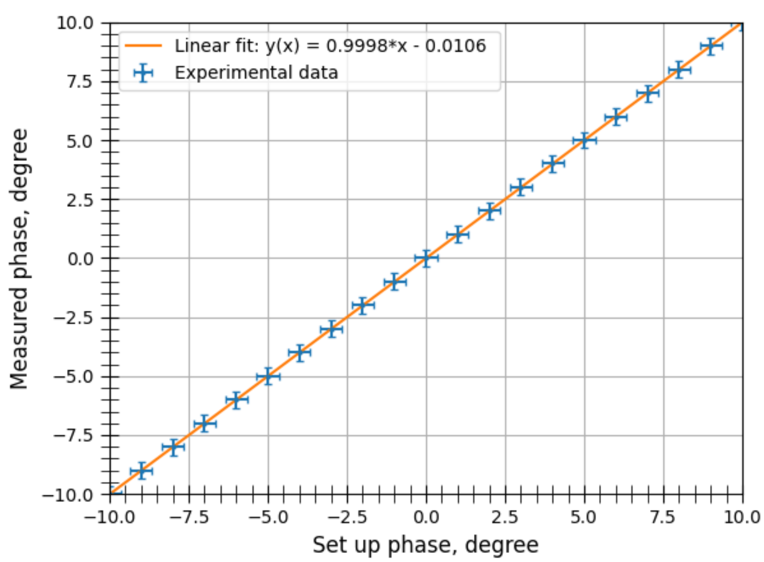

Figure 62: Zoomed in phase detection linearity measurement results

4.2 2856 MHz signal phase detection linearity check

Test-bench setup demonstrated on the figure 63 was assembled to check 2856 MHz signal phase detection linearity The DAC 1 output generates the 40 MHz CW signal with constant phase and amplitude. Then, the signal frequency is divided by 4 and fed to the 10 MHz PLL input. The phase-locked SG generates 2816 MHz CW local oscillator (LO) signal for frequency up-conversion and down-conversion purposes. The DAC 2 output generates 40 MHz CW signal which is fed to the RF-miser intermediate frequency (IF) input, while 2816 MHz CW is injected to the LO input.

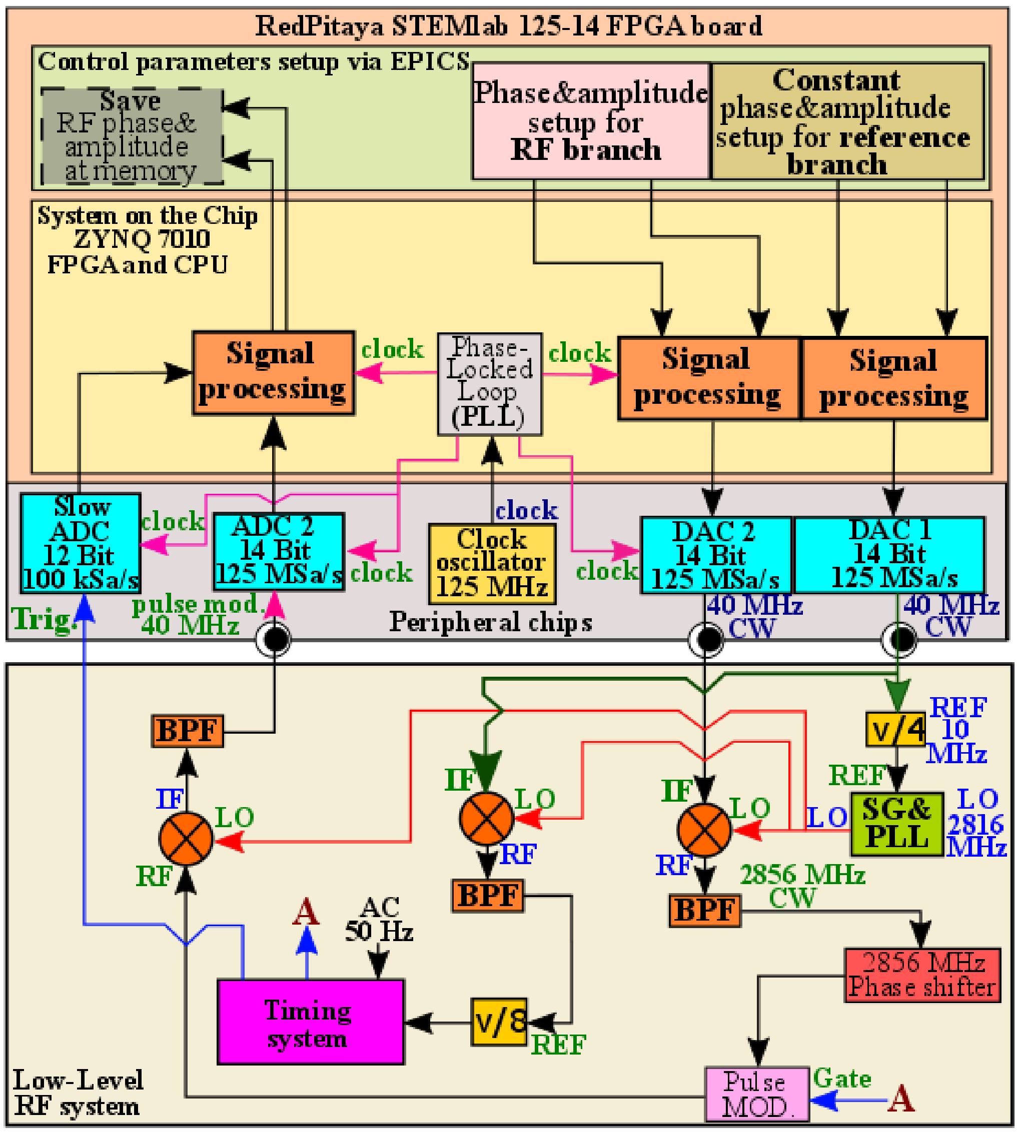

Figure 63: 2856MHz signal phase detection linearity measurement setup schematics

The RF output is filtered by BPF to reject sub-harmonics occurred during the signals mixing. The resulting frequency after filtering is 2856 MHz. Its phase is controlled by the calibrated phase shifter (see figure 63). Then, it is pulse modulated by the gate signal generated by the timing system, which is phase-locked to the 8^{th} subharmonic of the 2856 MHz. On the next stage, the phase-shifted RF signal is down-converted from 2856 MHz to 40 MHz by mixing with common LO and resulting IF signal is filtered by the BPF. Finally, the RF phase is detected by the FPGA board.

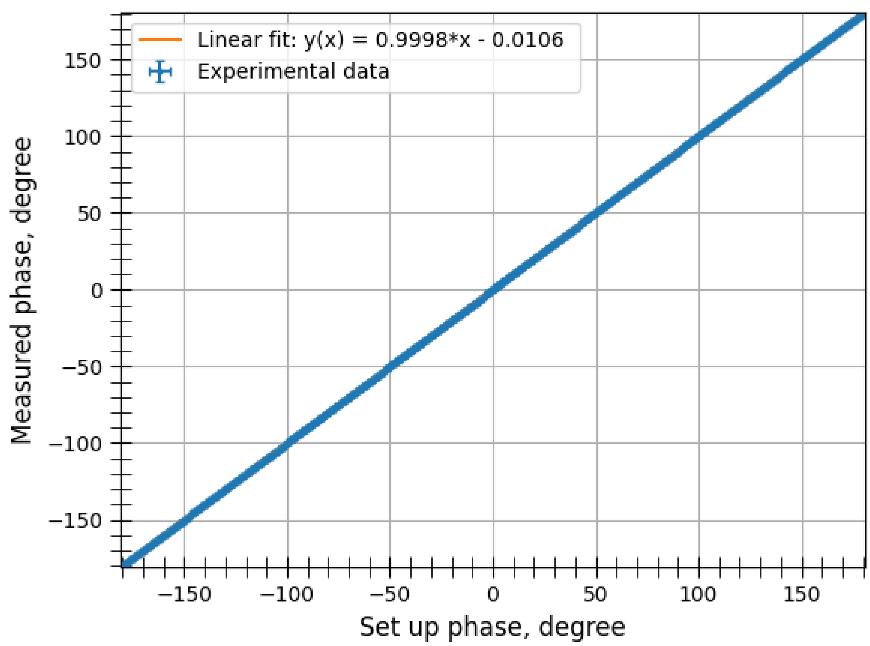

Figure 64: Phase detection linearity measurement results

Phase detection resolution is 0.044 ° (RMS). The error bar width demonstrated on the figure 64 is 6·RMS for the sake of visibility. The phase detection range is 360 °: from -180 ° to +180 °. The measured data was fitted with linear dependence. The fit amplitude and slope are $-0.011 \pm 0.001\,°$ and 0.998 ± 0.001, respectively. The line lies within the detection resolution.

If the RF-Gun or Booster accelerating field phase is drifting, fluctuating or jittering, it will be detected after the mixing with the common LO signal, because the down-converted frequency saves the phase information of the 2856 MHz frequency (RF) (see appendix A). Therefore, accelerating field phase can be detected with 0.044° (RMS) resolution.

4.3 40 MHz signal phase setup linearity check

Test-bench setup demonstrated on the figure 65 was assembled to check 40 MHz CW signal phase setup linearity. DAC 1 generates the 40MHz CW signal. The signal frequency is divided 4 times and fed to the AWG conventional preinstalled 10 MHz PLLs to phase-lock FPGA board crystal oscillator with AWG crystal oscillator. The AWG generates +3.3V pulse signal for the FPGA board external trigger input to start acquisition on the pulse rising edge arrival.

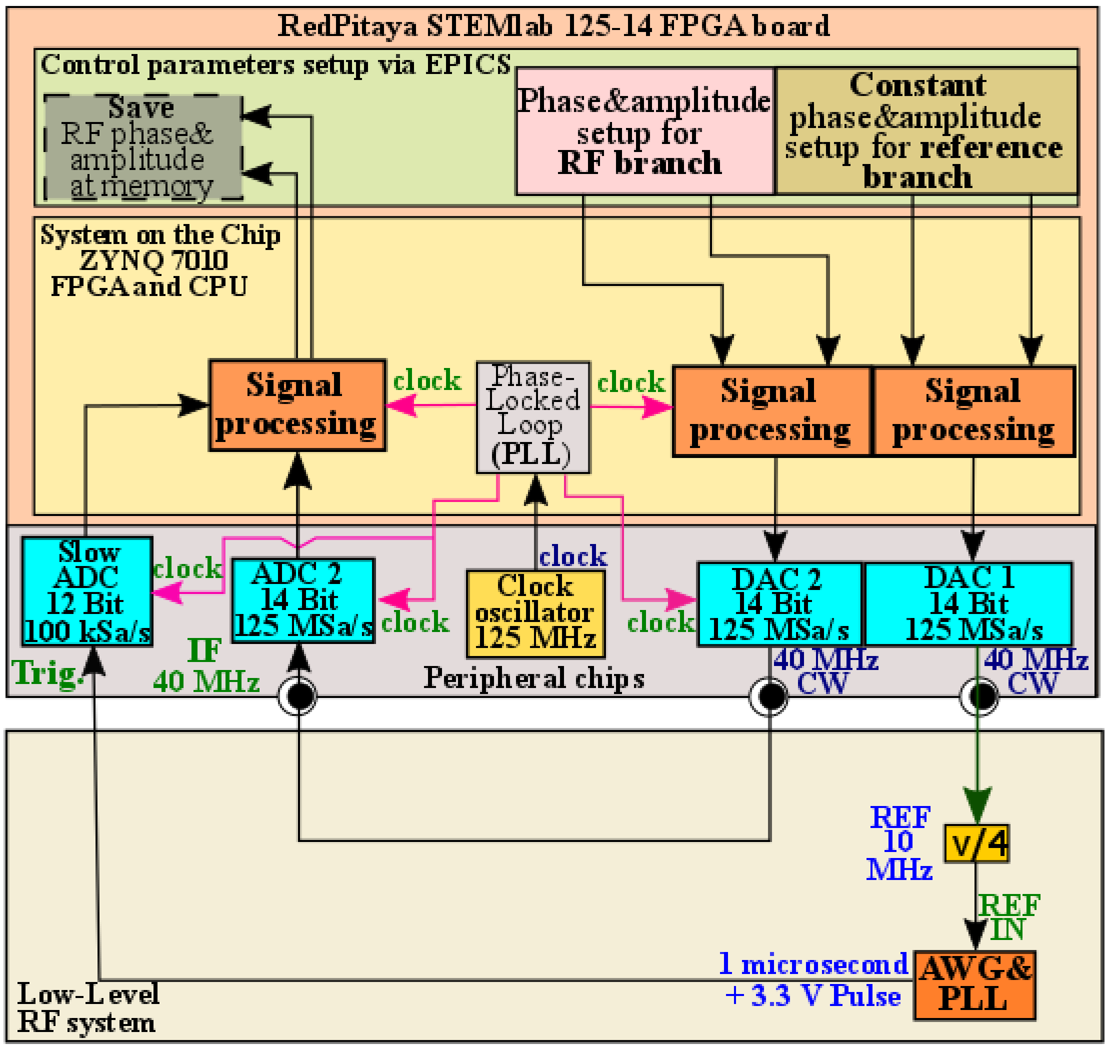

Figure 67: 40 MHz CW signal phase setup linearity measurement setup

The DAC 2 output generates the 40 MHz CW signal, which phase is controlled by the FPGA board signal processing logic (see chapter 3.1, appendix A and B). The signal is fed to the ADC 2 input and its phase is detected by the FPGA board logic.

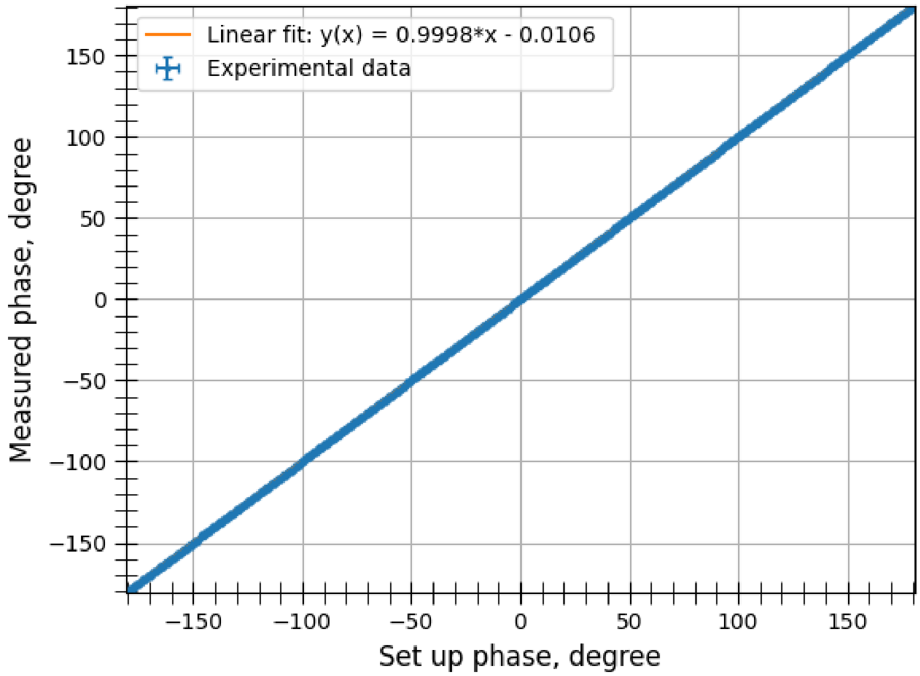

Figure 69: Phase setup linearity measurement results

Phase setup resolution is 0.044 ° (RMS). The error bar width demonstrated on the figure 68 is 6·RMS for the sake of visibility. The phase setup range is 360 °: from -180 ° to +180 °. The measured data was fitted with linear dependence. The fit amplitude and slope are -0.011 ± 0.001 ° and 0.998 ± 0.001, respectively. The line lies within the detection resolution.

If the RF-Gun or Booster accelerating field phase is drifting, fluctuating or jittering, it will be corrected by the IF CW signal phase shift (see appendix A and B). According to the phase setup&detection linearity measurement results, the maximum possible phase RMS stability of RF phase is 0.044 °

CHAPTER 5
RedPitaya STEMlab 125-14 FPGA board based LLRF feedback implementation into KEK LUCX facility LLRF system and its performance results

KEK LUCX facility has two accelerating cavities (RF-Gun and Booster), RF-Gun Nd:YAG laser system, Nd:YAG laser oscillator for Compton experiment and timing system, which require RF signals. Hence, two FPGA boards are required to implement feedback system at KEK LUCX facility (see figure 70).

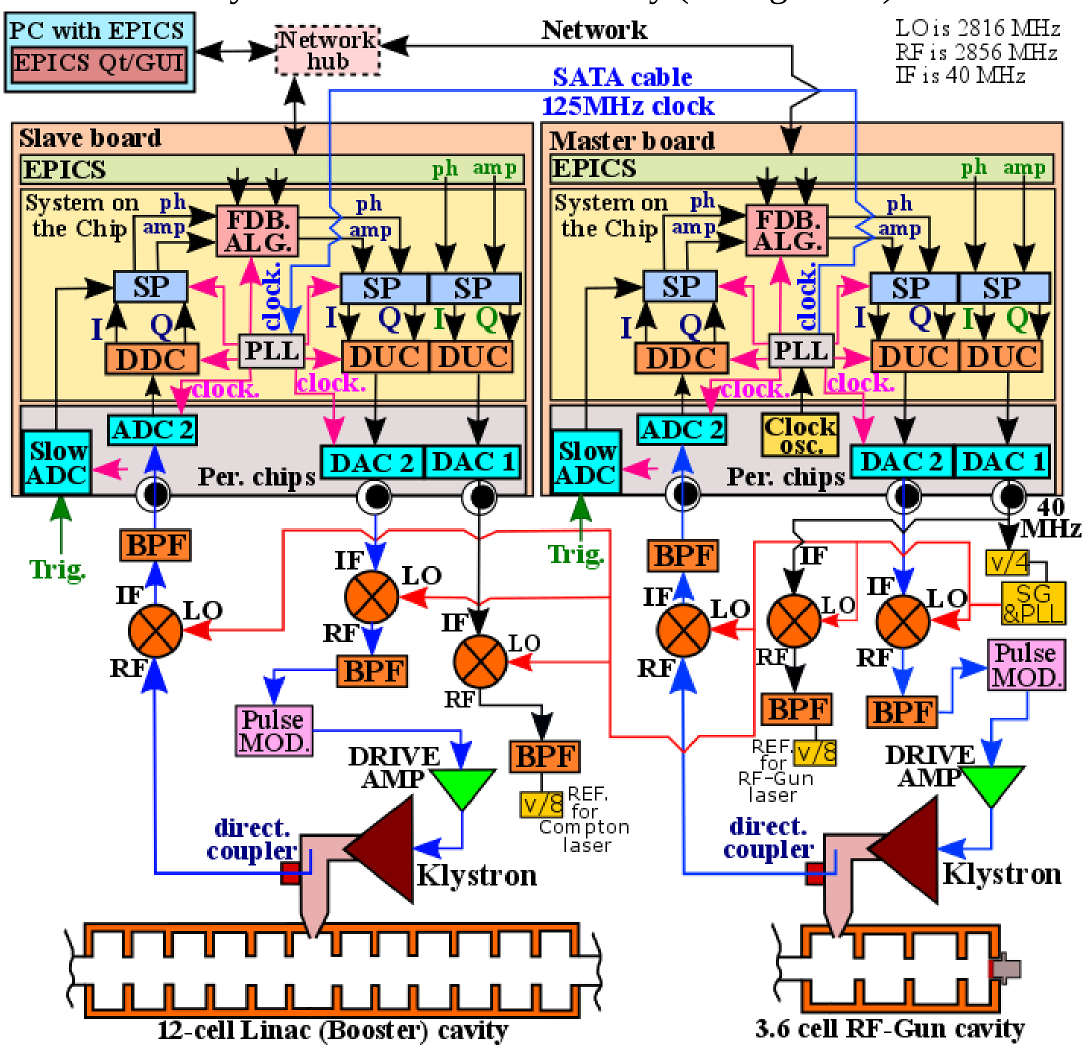

Figure 70: KEK LUCX accelerator Low-Level RF system schematic: SP is the signal processing, DUC is the digital down-conversion, SG is the signal generator, PLL is the phase-locked loop, BPF is the band-pass filter, "FDB. ALG." is the feedback algorithm

The Master board and Slave board shares the common 125 MHz clock signal supplied by the oscillator installed on the Master board. The Slave board is phase-locked the Master board ADC crystal oscillator in daisy chain via SATA connection. Hence, all signal processing and generation block are phase-locked with each-other. The RMS and peak-to-peak phase noises between the Master and Slave boards' outputs are 0.027° and 0.2 ° (see figure 71), respectively. As a result, the RF-Gun and Booster accelerating fields are synchronized with the same phase stability (see appendix A). The DAC 2 outputs are utilized to control the RF-Gun and Booster accelerating fields (see chapter 2 and 3).

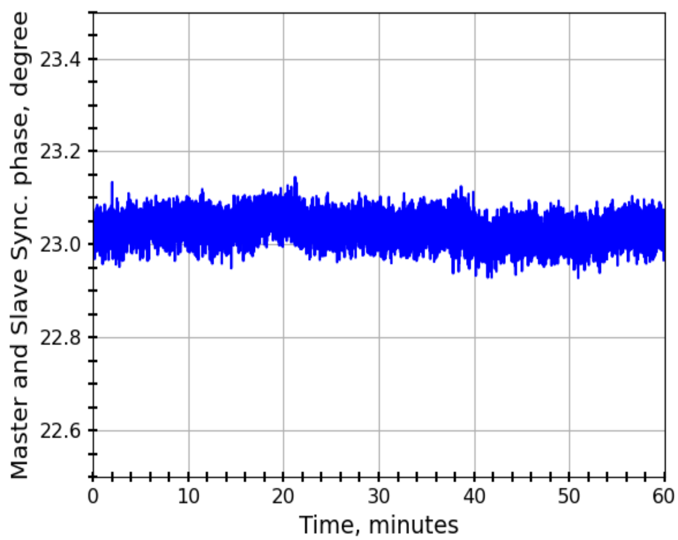

Figure 71: Synchronization stability between Master and Slave boards outputs

The DAC 1 outputs frequency after the up-conversion from 40 MHz to 2856 MHz are divided 8 times to get 357 MHz reference signals with a constant phase and amplitude for the RF-Gun laser oscillator feedback system (Time Bandwidth Systems) and laser-Compton experiment 4-mirrors cavity feedback system [44]. These reference signals are required to phase-lock laser-pulses generation with the accelerating fields. Therefore, the electron beam generation is phase-locked with the accelerating field and the laser pulse train at the Compton Experiment interaction point (see figure 2 and 36).The experiments were performed at KEK LUCX facility according to the facility operation rules. One operation shift is 8 hours. The facility warms up 2 hours. The data taking is next 4 hours and the rest of the time is devoted to shut down facility. The experiment setups and the feedback performance results are described in the next sections.

5.1 RF-Gun accelerating field stabilization experiment

The RF-Gun accelerating field stabilization without electron beam generation is a milestone for the feedback implementation into the facility LLRF system. Hence, the experimental test only with the facility RF system was performed to check the feedback algorithms effectivity to stabilize RF-Gun accelerating field.

5.1.1 Experimental setup

The KEK LUCX RF-Gun LLRF system branch with the digital feedback is demonstrated on the figure 72.

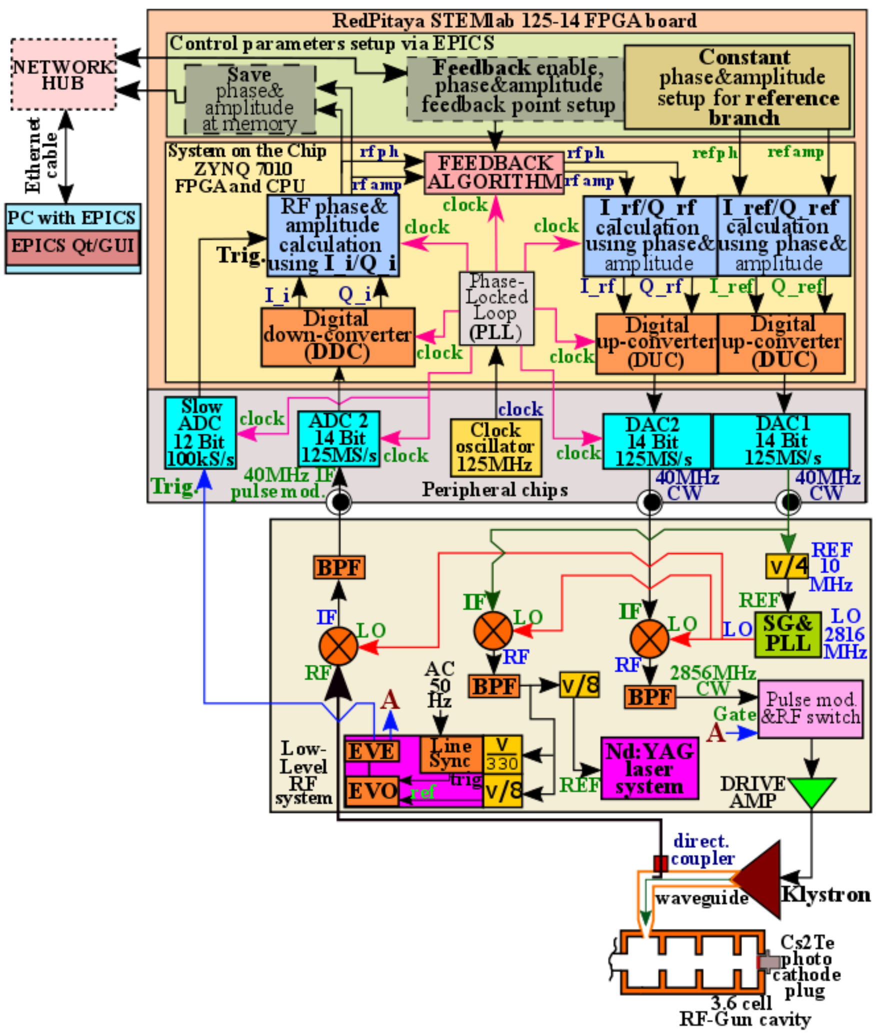

Figure 72: Experimental setup

The LLRF system configuration and the feedback signal processing with algorithms are the same as described ones in the sections 2.2, 3.1 and 4.2.

5.1.2 Experiment results

The experimental data was synchronously acquired every machine cycle during the 4 hours facility operation for RF-Gun LLRF feedback branch performance test after machine RF system warm up and its conditioning.

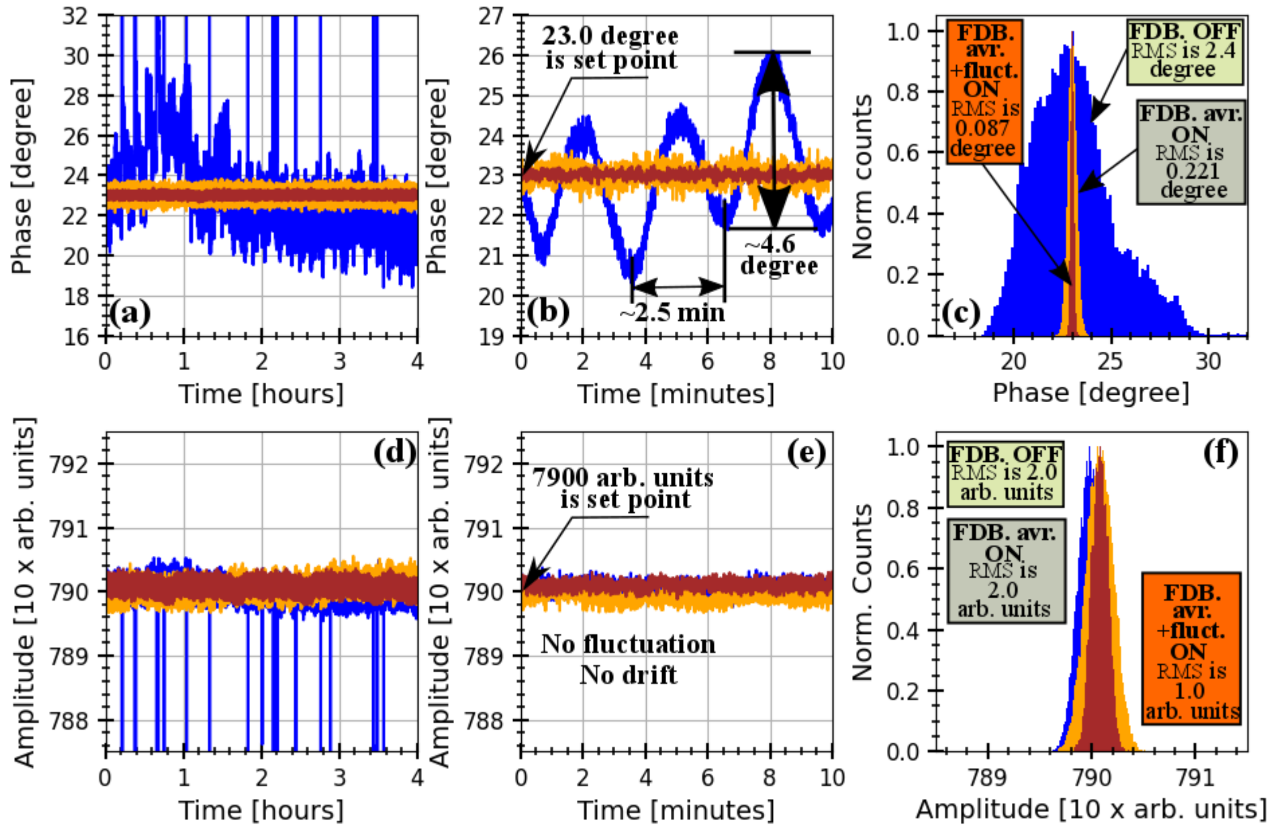

Figure 73: RF-Gun accelerating field stability experimental data (blue line is FDB OFF, orange line is FDB avr. ON, red line is FDB avr.+fluct. elim. ON): (a), (b) and (c) are RF-Gun phase stability during 4 hours, first 10 minutes and histogram, respectively; (d), (e) and (f) are RF-Gun amplitude stability during 4 hours, first 10 minutes and histogram, accordingly

The structure of phase instability includes fluctuation with 2.5 minutes period and 2.3 ° amplitude, phase drift and noise. Phase peak-to-peak and RMS stabilities with disabled feedback (“FDB OFF”) are 14 ° and 2.4 °, which correspond to 14 ps and 2.4 ps of 2856 MHz. However, amplitude does not drift or fluctuate. It jitters 2.0 arb. units (RMS) noise. Additionally, several discharges and RF system fails occurred during the data taking.

Nevertheless, feedback averaging algorithm ("FDB. avr. ON") improves phase RMS stability from 2.4 ° to 0.2 °, while amplitude RMS stability was not changed. The feedback averaging with fluctuation elimination algorithm ("FDB avr.+fluct. elim. ON") improved phase and amplitude RMS stabilities from 2.4 ° to 0.09 ° and from 2 arb. units to 1 arb. unit, respectively. Moreover, when the feedback was turned on, the discharges were eliminated.

5.2 Beam parameters stabilization experiment

Experimental verification of the electron beam parameters stabilization by stabilizing the RF-Gun accelerating field phases and amplitudes was necessary to proof that the LLRF feedback actually works. This experiment was performed at the June 2023, while the previous experiment (see section 5.1) was conducted at the February 2023.

5.2.1 Experimental setup

The KEK LUCX facility beamline and LLRF system with the digital feedback are demonstrated on the figure 74. The Booster klystron was turned off.

The nominal operating parameters of LUCX facility are listed in the table 1. The beam is accelerated up to 7.7 MeV by 3.6-cell RF-Gun. The high-power accelerating field is supplied to the RF-Gun from klystron via waveguide. After the acceleration, the beam enters a solenoid installed at an outlet of the RF-Gun. The emittance compensated electron beam passes through the first steering magnet (St1) to correct the small orbit misalignment. Then, the beam passes through the first quadrupole doublet (Qd1) and the second steering magnet (St2) to adjust the beam transverse size and position. After the orbit correction, the beam transverse size is adjusted by the pair of quadrupole doublets (Qd2 and Qd3) before the entrance to the bending magnet. After the bending, the beam propagates through the fourth quadrupole doublet (Qd4) and hits the beam profile monitor (Screen) (see chapter 1) before hitting the beam dump.

The calculated horizontal dispersion η_x at the screen location is 590 mm. The beam average energy of 7.700 ± 0.005 MeV and energy spread of 25 ± 1 keV correspond to the facility nominal operating parameters (see table 1). Hence, the beam average energy and energy spread change due to the accelerating field phase or/and amplitude drift will be detected as the image profile centroid position shift (see section 1.6.4) and the profile width change.

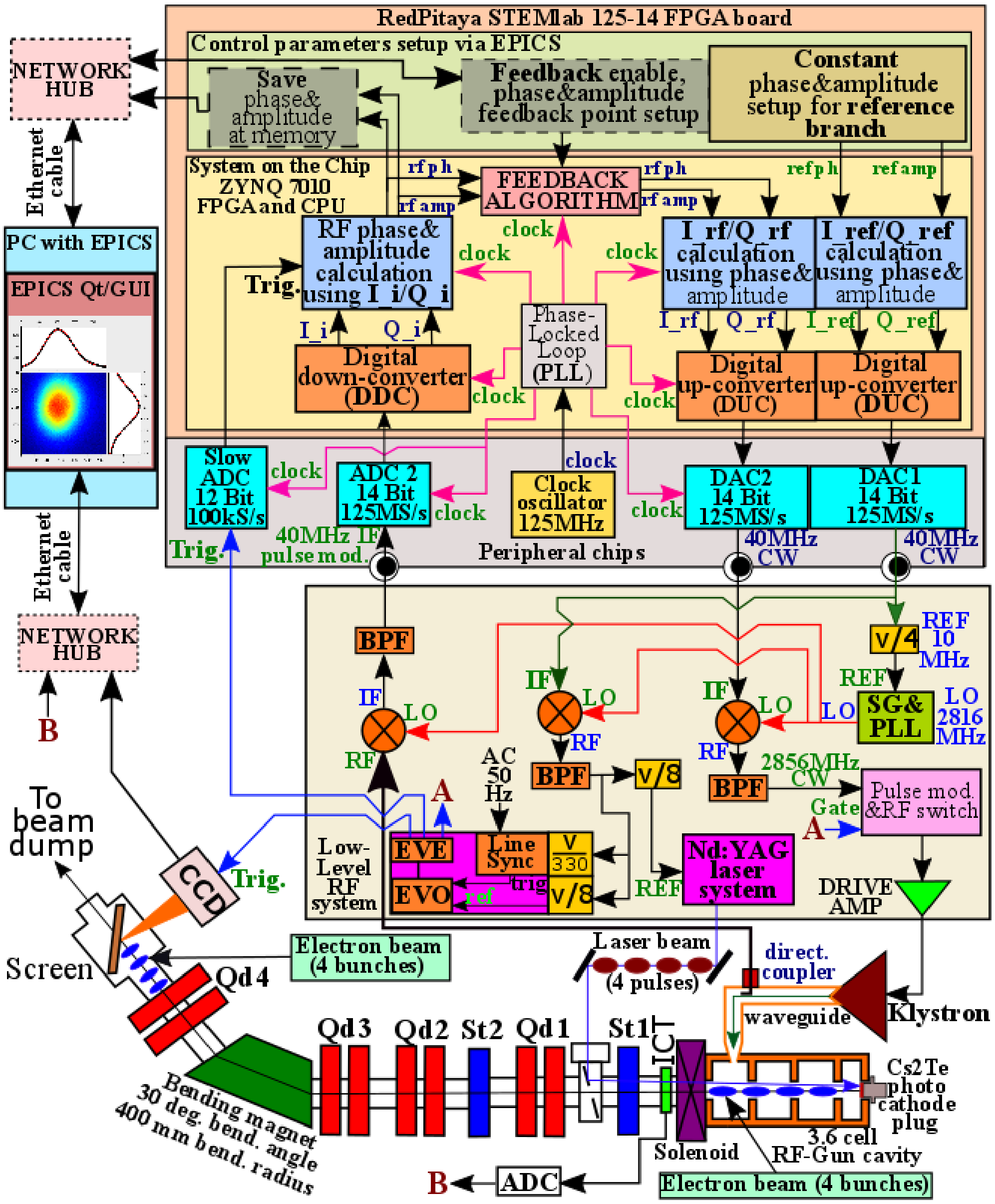

Figure 74: Experimental setup

Moreover the monitor is located at the position where the dispersive beam size contribution to the measured profile $\eta_x \cdot dE/E = 1915$ µm is larger than the betatron size contribution $(\beta_x \epsilon_x/\gamma)^{1/2} = 600$ µm, where γ and β_x are the Lorentz factor and the horizontal beta function, respectively. Thus, the beam profile transverse size (RMS) on the screen is recalculated using the equation 14 [45].

$$dE = E\, dx/\eta_x, \tag{14}$$

where dx is the beam transverse horizontal size (RMS) on the screen, E is the beam average energy, η_x is the horizontal dispersion at the screen location, dE is the beam energy spread (RMS).

For the given beamline optics, the profile monitor allows to detect the beam average energy and energy spread from 7.820 ± 0.005 MeV to 7.580 ± 0.005 MeV and from 25 ± 1 keV to 80 ± 1 keV, correspondingly.

The screen calibration curve is demonstrated on the 75.

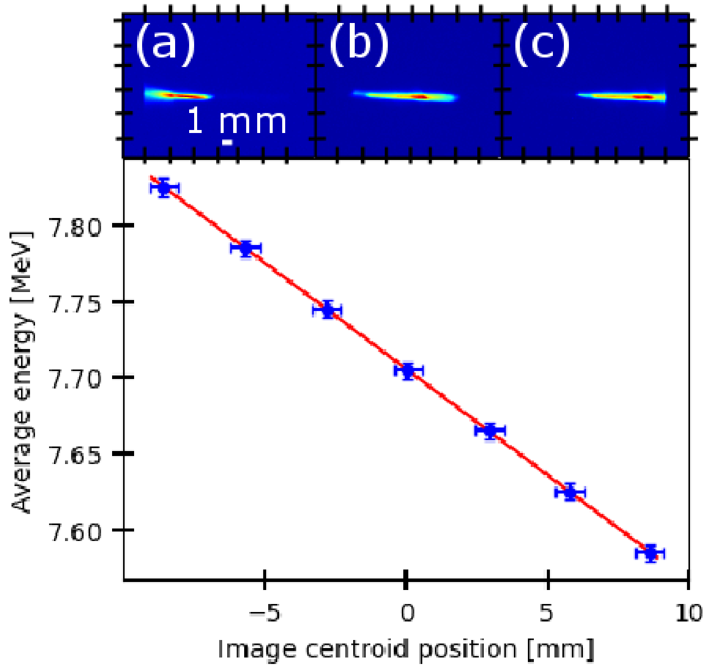

Figure 75: Top row: the beam profile for the different bending magnet currents corresponds to: (a) 7.82 MeV, (b) 7.80 MeV, (c) 7.58 MeV, respectively. Bottom row: beam image centroid position versus the beam average energy (blue dots with error bars) with linear fit function (red solid line): amplitude 0.0 MeV and slope mm/MeV

The calibration was performed by measuring the transverse beam profile shift for a few different bending magnet current settings which corresponds to the different beam average energies. The LLRF feedback was turned on during the calibration.The beam charge is measured by the Integrating Current Transformer (ICT) with the resolution of 2 pC [46]. It is installed after the solenoid (see figure 73). The bunch charge is calculated by dividing the beam charge to the number of the bunches. For this experiment, it is 4. The RF-Gun field is monitored by the LLRF system and signal processing logic programmed inside RedPitaya FPGA board (see figure 74 and 54). As additional information, RF-Gun cavity surface temperature was measured by the T-type thermocouple with 0.1 ℃ detection resolution. The thermocouple is installed on the first half-cell of the RF-Gun cavity.

5.2.2 Experiment results

The experimental data was synchronously acquired every machine cycle during the 4 hours facility operation for feedback ON (*corresponds to enabled "FDB avr.+fluct. elim. ON", when feedback averaging and fluctuation elimination algorithms are disabled*) and feedback OFF (*corresponds to "FDB OFF", when the entire feedback is disabled*) cases after machine RF system warm up, its conditioning and beamline optics corrections. Every profile monitor image was processed according to the following procedure. In the beginning, the image horizontal profile was fitted by the Gaussian distribution. Then, the image width and its centroid position were recorded after the application of the energy calibration factor.

The experimental results are demonstrated on the figures 75, 76 and 77. As can be seen, the RF-Gun cavity surface temperature fluctuates with 0.5 ℃ and 3 minutes period due to the cavity temperature isolation absence and unstable accelerating tunnel temperature control. The temperature inside the tunnel is controlled by the industrial air-conditioner. The cavity temperature fluctuation induces accelerating field phase fluctuation with 3.5 ° amplitude and 3 minutes period. The accelerating field amplitude slowly drifts form 8054 arb. units to 7800 arb. units. As a result, beam average energy and energy spread fluctuate with the same 3 minutes period. Moreover, the dataset shows the certain pattern of the fluctuation. The temperature and phase fluctuate mostly in-phase relative each-other, while the phase and the beam average energy fluctuate with half cycle advance. The energy spread data maximum points correspond to the phase and the average energy minima. The bunch charge jitters from 300 pC to 150 pC.

Nevertheless, the digital LLRF feedback improved accelerating field phase and amplitude peak-to-peak stability from 11.5 ° to 1 ° and from 254 arb. units to 50 arb. units. As a consequence, the electron beam average enrgy, energy spread and bunch charge peak-to-peak stability was improved more than 10 times.

Number of bins for the histograms with feedback ON and feedback OFF is 51. The widths of distributions are different, that is why the bins are visible for histogram with feedback ON, but the bins are not visible for histogram with feedback OFF. Moreover, all histograms are normalized to 1 for the sake of visibility.

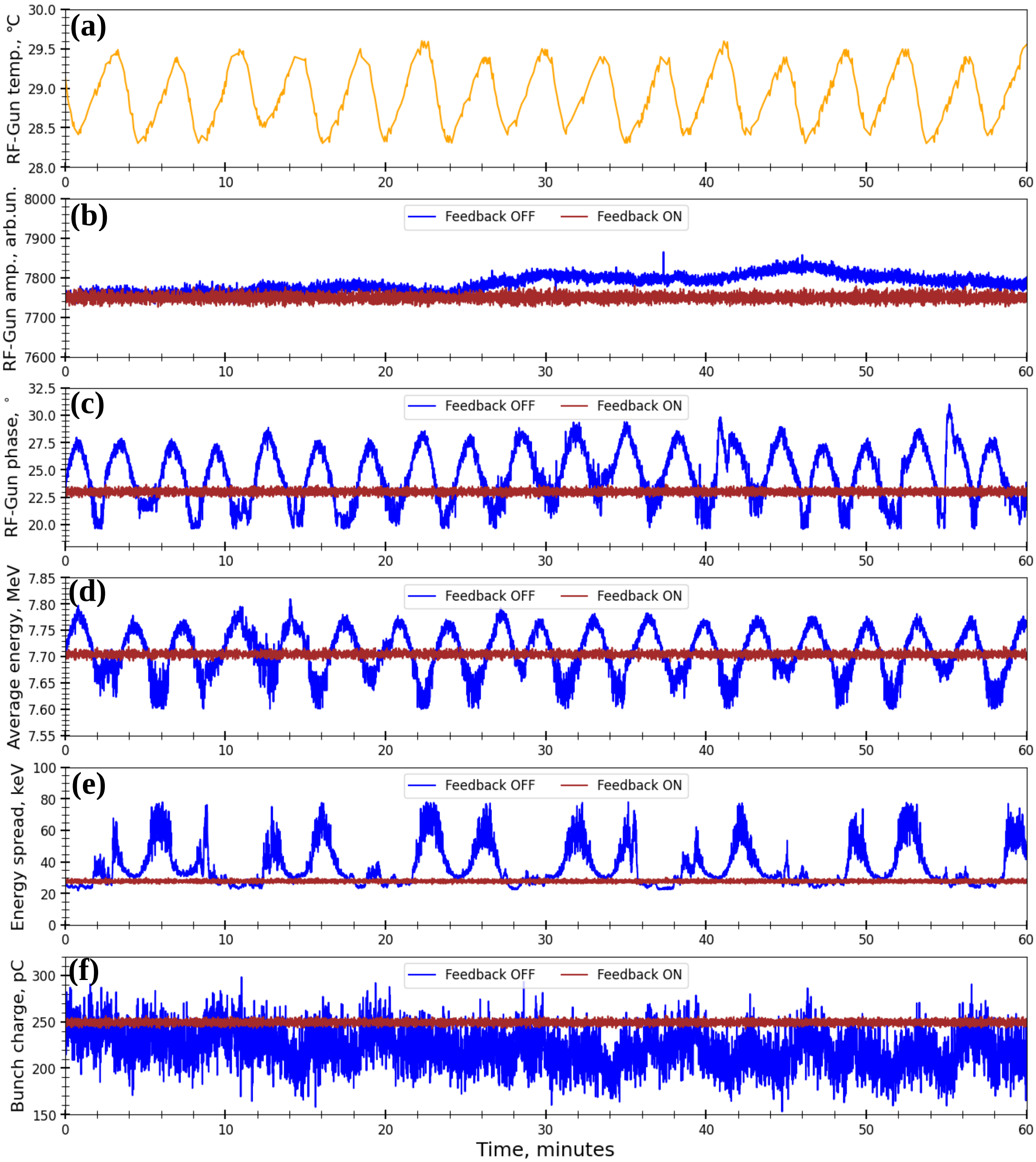

Figure 75: Experimental data strip charts (60 minutes time span): (a) is the RF-Gun cavity surface temperature, (b) is the RF-Gun accelerating field amplitude, (c) is the RF-Gun accelerating field phase, (d) is the average energy, (e) is the energy spread (RMS), (f) is the bunch charge.

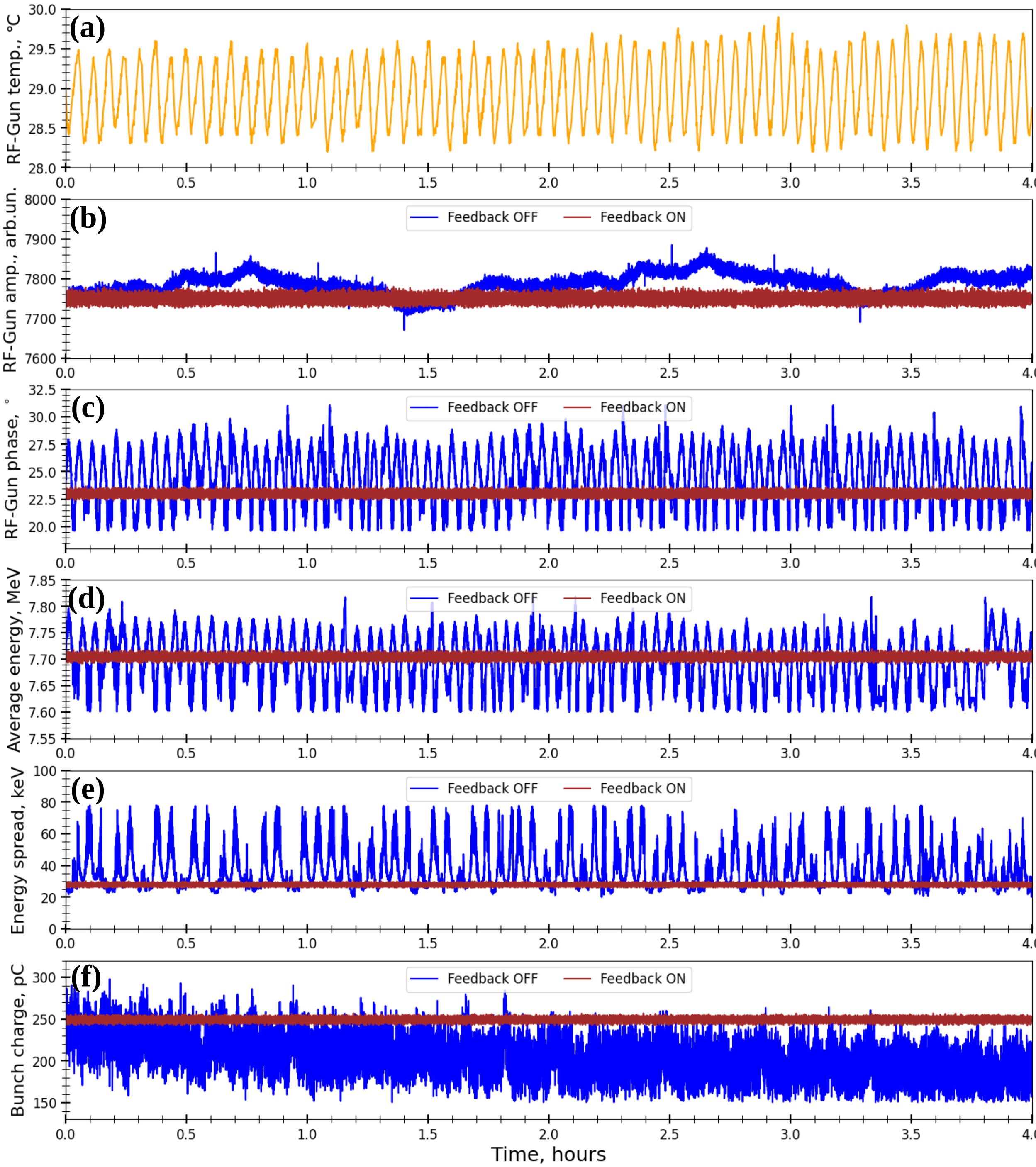

Figure 76: Experimental data strip charts (4 hours time span): (a) is the RF-Gun cavity surface temperature, (b) is the RF-Gun accelerating field amplitude, (c) is the RF-Gun accelerating field phase, (d) is the average energy, (e) is the energy spread (RMS), (f) is the bunch charge.

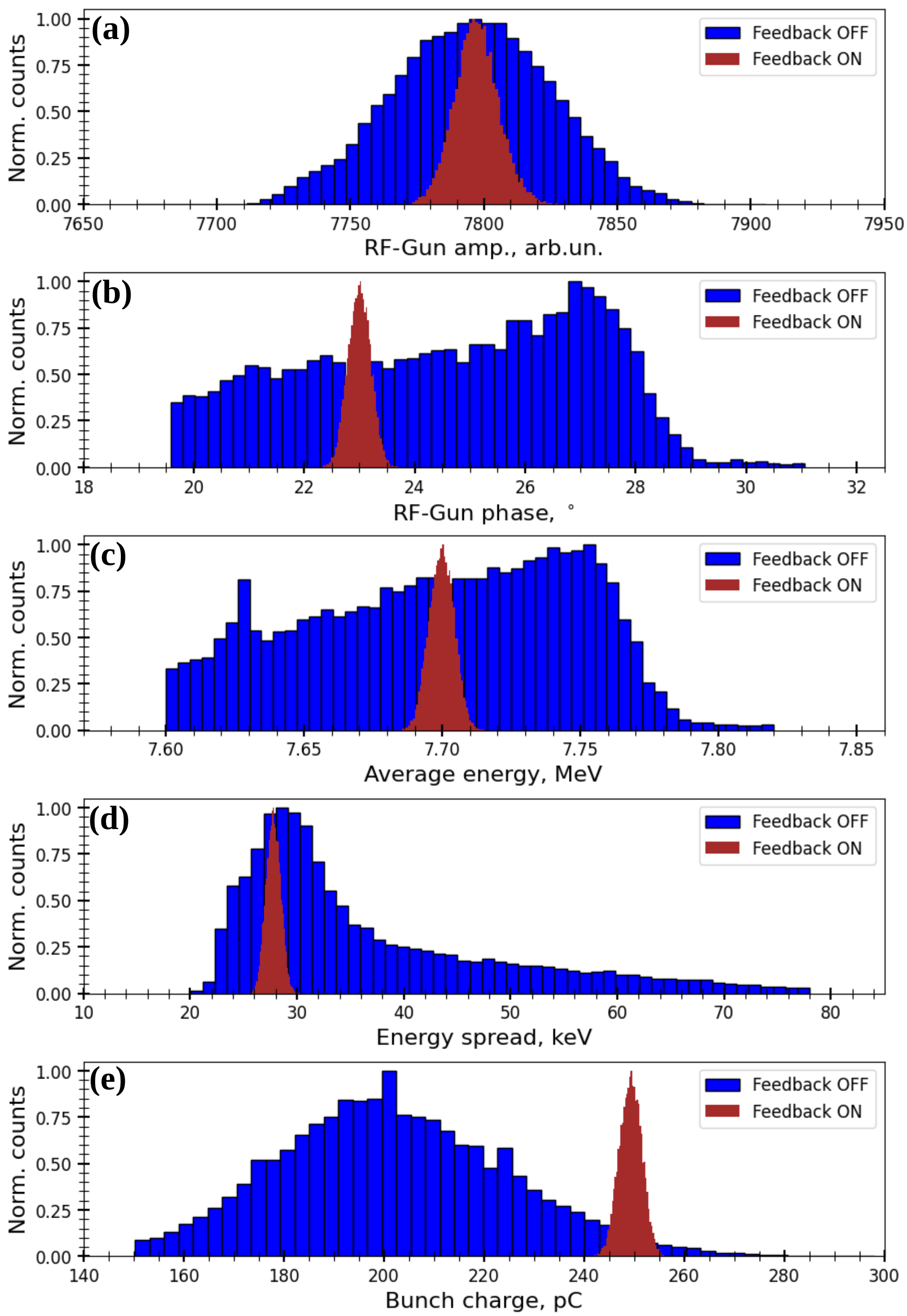

Figure 77: Experimental data histograms: (a) is the RF-Gun accelerating field amplitude, (b) is the RF-Gun accelerating field phase, (c) is the average energy, (d) is the energy spread (e) is the bunch charge

5.3 Booster accelerating field stabilization experiment

The Booster accelerating field stabilization without electron beam generation is final step for the feedback implementation into the facility LLRF system. Hence, the experimental test only with the facility Booster RF system branch was performed to check the feedback algorithms effectivity to stabilize Booster accelerating field.

5.3.1 Experimental setup

The KEK LUCX Booster LLRF system branch with the digital feedback is demonstrated on the figure 79.

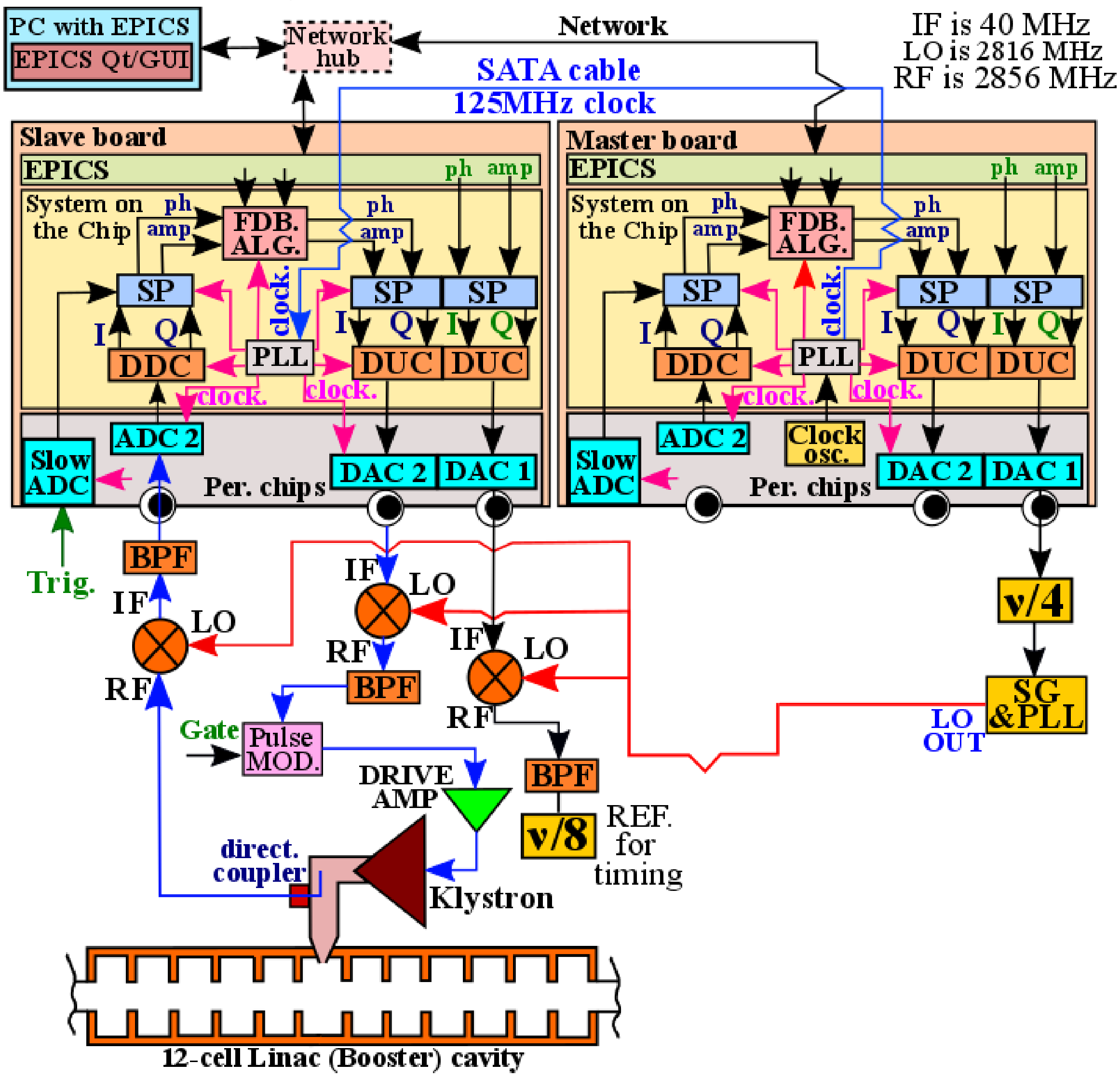

Figure 79: Experimental setup

The LLRF system configuration and the feedback signal processing with algorithms are the same as described ones in the sections 2.2, 3.1 and 4.2, except the phase-locking scheme. The slave board signal processing and generation is phase-locked to the master board clock oscillator, while the SG oscillator is phase-locked to the master board clock oscillator via preinstalled conventional 10 MHz PLL.

5.3.2 Experiment results

The experimental data was synchronously acquired every machine cycle during the 4 hours facility operation for Booster LLRF feedback branch performance test after machine RF system warm up, its conditioning.

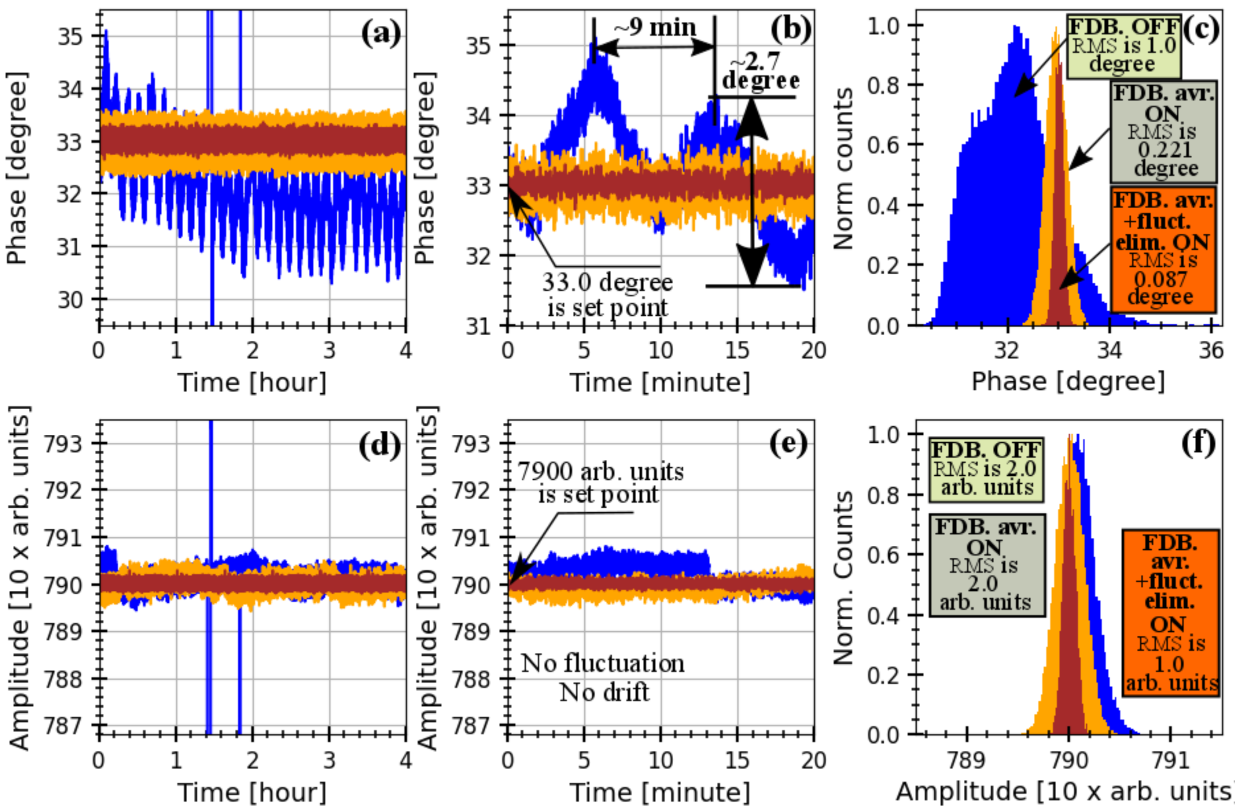

Figure 80: Booster accelerating field stability experimental data (blue line is FDB OFF, orange line is FDB avr. ON, red line is FDB avr.+fluct. elim. ON): (a), (b) and (c) are Booster phase stability during 4 hours, first 10 minutes and histogram, respectively; (d), (e) and (f) are Booster amplitude stability during 4 hours, first 10 minutes and histogram, accordingly

The structure of phase instability includes fluctuation with 9 minutes period and 1.35 ° amplitude, phase drift and noise. Phase peak-to-peak and RMS stabilities with disabled feedback (“FDB OFF”) are 4.5 ° and 1.0 °, which correspond to 4.5 ps and 1.0 ps of 2856 MHz. However, amplitude does not drift or fluctuate. It jitters 2.0 arb. units (RMS) noise. Additionally, several discharges and RF system fails occurred during the data taking.

Nevertheless, feedback averaging algorithm (“FDB. avr. ON”) improves phase RMS stability from 1.0 ° to 0.2 °, while amplitude RMS stability was not changed. The feedback averaging with fluctuation elimination algorithm (“FDB avr.+fluct. elim. ON”) improved phase and amplitude RMS stabilities from 1.0 ° to 0.09 ° and from 2 arb. units to 1 arb. unit, respectively. Moreover, when the feedback was turned on, the discharges would be eliminated.

CONCLUSION

Digital LLRF feedback system using Digital Down-Conversion&Digital Up-Conversion technique programmed at RedPitaya STEMlab 125-14 FPGA board was developed, implemented, tested to control and stabilize accelerating field at KEK LUCX facility. Precisely controlled accelerating field is milestone to generate stable electron beam for the high quality laser-Compton X-Ray generation. The research can be summarized as follows.

- Digital LLRF feedback system for KEK LUCX facility based on the standalone, commercially available RedPitaya STEMlab 125-14 FPGA boards was demonstrated. The system configuration includes two FPGA boards phase-locked with each-other by sending master board 125 MHz clock to slave board via SATA cable. Although, the conventional 10 MHz PLL preinstalled at the SG was utilized to phase-lock it with the boards. The RMS and peak-to-peak phase-locking stabilities of the up-converted 2856 MHz CW signal achieved by this configuration are 0.027 ° and 0.2 °, respectively.
- Digital LLRF two step feedback algorithms, which does not require tuning and calibrating, were employed into the FPGA boards' SoCs. These algorithms are averaging and fluctuation elimination.
- RF-Gun and Booster accelerating field phases RMS stabilities were improved from 2.4 ° to 0.09 ° and form 1.0 ° to 0.09°, respectively. Also, RF-Gun and Booster accelerating field amplitude RMS stabilities were improved only 2 times from 2 arb. units to 1 arb. unit.

As a result of the accelerating field stabilization, the electron beam parameters were stabilized more than 10 times. As an optimistic prediction, the laser-Compton X-Ray characteristics will be stabilized 10 times. Moreover, the precise RF control of accelerating field allows conducting long-term X-Ray imaging experiments for the medical and material science applications at KEK LUCX facility.

APPENDIX A

Mathematics behind frequency up-conversion and down-conversion at the RF-Mixers

Mathematical explanation of the frequency up- and down-conversion is explained in this chapter. The main focuses are phase setup during frequency up-conversion and phase detection during frequency down-conversion. Sinewaves representation was used for the final equations deviation

Frequency up-conversion

Basic trigonometric identity shows the rule to convert sinewaves product into sinewaves sum:

$$sin(z) = sin(x) \cdot sin(y) = 0.5 \cdot [cos(x - y) - cos(x + y)] \qquad \text{(A.1)}$$

Let's consider the next substitution:

$$x = \omega_0 \cdot t + \varphi_0 + \Delta\varphi_0, \qquad \text{(A.2)}$$

where $\omega_0 = 2\pi \cdot \nu_0$, ν_0 is the frequency of the IF signal, φ_0 is the initial phase of the IF signal, $\Delta\varphi_0$ is the manual or automatic phase shift of the IF signal, π is the constant, it equals to 3.14.

$$y = \omega_1 \cdot t + \varphi_1, \qquad \text{(A.3)}$$

where $\omega_1 = 2\pi \cdot \nu_1$, ν_1 is the frequency of the LO signal, φ_1 is the initial phase of the LO signal, π is the constant, it equals to 3.14.

Substitute the equations (A.2) and (A.3) into the (A.1) and get (a.4):

$$sin(z) = sin(\omega_0 \cdot t + \varphi_0 + \Delta\varphi_0) \cdot sin(\omega_1 \cdot t + \varphi_1) =$$

$$0.5 \cdot [cos(\omega_0 \cdot t + \varphi_0 + \Delta\varphi_0 - \omega_1 \cdot t - \varphi_1) -$$

$$- cos(\omega_0 \cdot t + \varphi_0 + \Delta\varphi_0 + \omega_1 \cdot t + \varphi_1)] \qquad \text{(A.4)}$$

It is necessary to reorganize equation (A.4):

$$sin(z) = 0.5 \cdot [cos(2\pi \cdot (\nu_0 - \nu_1) \cdot t + (\varphi_0 - \varphi_1) + \Delta\varphi_0) -$$
$$-cos(2\pi \cdot (\nu_0 + \nu_1) \cdot t + (\varphi_0 + \varphi_1) + \Delta\varphi_0)] \quad (A.5)$$

Band-Pass filter is applied to the equation (A.5):

$$BPF[sin(z)] = -0.5 \cdot cos(2\pi \cdot (\nu_0 + \nu_1) \cdot t + (\varphi_0 + \varphi_1) + \Delta\varphi_0) \quad (A.6)$$

Let’s make a reassignment:

$$sin^*(z) = BPF[\sin(z)] \quad (A.7)$$

$$\nu_0 + \nu_1 = \nu_2, \quad (A.8)$$

where ν_0 is equal to 40 MHz, $\nu_1$is equal to 2816 MHz,

$$40MHz + 2816MHz = 2856MHz \quad (A.9)$$

$$\varphi_0 + \varphi_1 = \varphi_2 \quad (A.10)$$

φ_0 is initial phase of the IF signal (40 MHz signal). It is highly stable. It is the phase stability of the FPGA board itself. It must be infinitely small in comparison with phase drift, oscillations and phase noise. φ_1 is the initial phase of the LO signal. Its initial phase is phase locked with FPGA board via 10MHz reference line or 10MHz CW PLL (phase-locked loop hereafter). It means that $\varphi_0 + \varphi_1 = const$. It never drifts or fluctuates.

The next stage is up-converted frequency amplification:

$$k_{amp} \cdot sin^*(z) = -0.5 \cdot k_{amp} \cdot cos(2\pi \cdot (\nu_0 + \nu_1) \cdot t +$$
$$+ (\varphi_0 + \varphi_1) + \Delta\varphi_0), \quad (A.11)$$

Let’s reassign equation (A.11) for the sake of visibility simplicity:

$$sin^{**}(z) = k_{amp} \cdot sin^*(z) \quad (A.12)$$

Substitute equations (A.8) and (A.9) into (A.11), then use equation (A.12):

$$sin^{**}(z) = -0.5 \cdot k_{amp} \cdot cos(2\pi \cdot \nu_2 \cdot t + \varphi_2 + \Delta\varphi_0) \quad (A.13)$$

As presented at equation (A.13), the phase shift of the IF signal will shift the phase of the entire RF signal after Band-Pass filtering and amplification.

Phase shift dependence is linear.

$$\Delta\varphi_0 = \Delta\varphi_2, \quad \text{(A.14)}$$

where $\Delta\varphi_2$ is phase shift of the RF signal after the Band-Pass filtering and amplification.

It is necessary to remember simple trigonometric equation presented at the equation (A.15):

$$-cos(w) = sin(w - \frac{\pi}{2}) \quad \text{(A.15)}$$

Reorganize equation (A.13) using equation (A.15):

$$sin^{**}(z) = 0.5 \cdot k_{amp} \cdot sin(2\pi \cdot \nu_2 \cdot t + (\varphi_2 - \frac{\pi}{2}) + \Delta\varphi_0) \quad \text{(A.16)}$$

Further explanation requires some reassignments and substitutions:

$$0.5 \cdot k_{amp} = A_2 \quad \text{(A.17)}$$

$$\varphi_2 - \frac{\pi}{2} = \varphi_2^* \quad \text{(A.18)}$$

$$sin^{**}(z) = sin_{up-conv}(z) \quad \text{(A.19)}$$

Substitute equation (A.17), (A.18) and (A.19) into (A.16):

$$sin_{up-conv}(z) = A_2 \cdot sin(2\pi \cdot \nu_2 \cdot t + \varphi_2^* + \Delta\varphi_0) \quad \text{(A.20)}$$

Down-conversion side

Let's remember basic trigonometric identity presented at the equation (A.1):

$$sin(z) = sin(x) \cdot sin(y) = 0.5 \cdot [cos(x-y) - cos(x+y)] \quad \text{(A.1)}$$

Up-converted signal was transferred into the pulse modulator, pre-amplifier, klystron, waveguide and to the accelerating cavity on the final step of the chain. The phase noise of the 2856MHz frequency is added to the equation (A.20):

$$sin_{up-conv}(z + \Delta\varphi_{dr}) = A_2 \cdot sin(2\pi \cdot \nu_2 \cdot t + \varphi_2^* + \Delta\varphi_0 + \Delta\varphi_{dr}), \quad \text{(A.21)}$$

where $\Delta\varphi_{dr}$ is the drift induced at the explained above delivery chain.

So, this induced drift must be compensated by $\Delta\varphi_0$ phase shift. Automatic phase shift of $\Delta\varphi_0$ is programed at the FPGA board based feedback loop. For the technical reasons, 2856MHz frequency must be down-converted back to the 40MHz (IF signal frequency). The RF signal is down-converted back to the 40MHz at the RF-Mixer using the same 2816MHz LO signal presented at the equation (A.3):

$$sin(q) = BPF[sin_{up-conv}(z + \Delta\varphi_{dr}) \cdot sin(2\pi \cdot \nu_1 \cdot t + \varphi_1)] =$$

$$= 0.5 \cdot A_2 \cdot cos(2\pi \cdot (\nu_2 - \nu_1) \cdot t + (\varphi_2^* - \varphi_1) + \Delta\varphi_0 + \Delta\varphi_{dr}) \quad \text{(A.22)}$$

Reminder of the equations (A.8), (A.10) and (A.18):

$$\nu_0 + \nu_1 = \nu_2 \quad \text{(A.8)}$$

$$\varphi_0 + \varphi_1 = \varphi_2 \quad \text{(A.10)}$$

$$\varphi_2 - \frac{\pi}{2} = \varphi_2^* \quad \text{(A.18)}$$

Make small reorganizations of the equations (A.8), (A.9):

$$\nu_0 = \nu_2 - \nu_1 \quad \text{(A.23)}$$

$$\varphi_0 = \varphi_2 - \varphi_1 \quad \text{(A.24)}$$

Substitute the equations (A.18), (A.23) and (A.24) into the equation (A.22):

$$sin(q) = 0.5 \cdot A_2 \cdot cos(2\pi \cdot \nu_0 \cdot t + \left(\varphi_0 - \frac{\pi}{2}\right) + \Delta\varphi_0 + \Delta\varphi_{dr}), \quad \text{(A.25)}$$

Let's reorganize the equation (A.25) for the sake of the visibility simplicity:

$$sin(q) = 0.5 \cdot A_2 \cdot cos(2\pi \cdot \nu_0 \cdot t + (\varphi_0 + \Delta\varphi_0 + \Delta\varphi_{dr}) - \frac{\pi}{2}), \quad \text{(A.26)}$$

$$cos(w) = -sin(w - \frac{\pi}{2}) \quad \text{(A.27)}$$

Apply the rule (A.27) for the equation (A.26):

$$sin(q) = -0.5 \cdot A_2 \cdot sin(2\pi \cdot \nu_0 \cdot t + (\varphi_0 + \Delta\varphi_0 + \Delta\varphi_{dr}) - \pi) \quad \text{(A.28)}$$

Let's remember simple trigonometric equation:

$$-si\,n(r - \pi) = sin(r) \quad \text{(A.29)}$$

Substitute the equation (A.29) into the equation (A.28) and get the equation (3.30):

$$sin(q) = 0.5 \cdot A_2 \cdot sin(2\pi \cdot \nu_0 \cdot t + (\varphi_0 + \Delta\varphi_0 + \Delta\varphi_{dr})) \quad \text{(A.30)}$$

The next stage of the down-converted signal is amplification:

$$k_{amp} \cdot sin(q) = k_{amp} \cdot 0.5 \cdot A_2 \cdot sin(2\pi \cdot \nu_0 \cdot t +$$

$$(\varphi_0 + \Delta\varphi_0 + \Delta\varphi_{dr})) \quad \text{(A.31)}$$

Let's make more understandable reassignment of the equation (A.31):

$$k_{amp} \cdot sin(q) = sin_{down-conv}(q) \quad \text{(A.32)}$$

$$k_{amp} \cdot 0.5 \cdot A_2 = A_2^* \quad \text{(A.33)}$$

$$sin_{down-conv}(q) = A_2^* \cdot sin(2\pi \cdot \nu_0 \cdot t + (\varphi_0 + \Delta\varphi_0 + \Delta\varphi_{dr})) \quad \text{(A.34)}$$

φ_0 is initial phase of the IF signal (40 MHz signal). It is highly stable. It is the phase stability of the FPGA board itself.

Let's consider the following situation: $A_2^* = 1$, $\varphi_0 = 0°$.

$$sin_{down-conv}(q) = sin(2\pi \cdot \nu_0 \cdot t + (\Delta\varphi_0 + \Delta\varphi_{dr})) \tag{A.35}$$

So, the phase feedback algorithm holds the next condition:

$$\Delta\varphi_0 + \Delta\varphi_{dr} = 0° \tag{A.36}$$

Frequency down-conversion technique saves the information about phase drift, fluctuation and noise.

APPENDIX B

Mathematics behind Digital Down-Conversion and Digital Up-Conversion

Digital Down-conversion

In trigonometry, the angle sum identity is:

$$\sin(\alpha+\beta) = \sin(\alpha)\cdot\cos(\beta) + \cos(\alpha)\cdot\sin(\beta) \qquad \text{(B.1)}$$

Sinewave equation is

$$y(t) = \mathrm{A}\cdot\sin(\omega\cdot t+\theta_0), \qquad \text{(B.2)}$$

where A is the amplitude, ω is the angular frequency and θ_0 is the phase.

Let's reconfigure the equation B.2 using the equation B.1 and phasor representation of orthogonal components. The phasor representation is conventional among researchers at RF science:

$$\mathrm{A}\cdot\sin(\omega\cdot t+\theta_0) = A\cdot\sin(\omega\cdot t)\cdot\cos(\theta_0) + A\cdot\cos(\omega\cdot t)\cdot\sin(\theta_0), \qquad \text{(B.3)}$$

The equation B.3 multiplication with $\cos(\omega\cdot t)$ function:

$$\mathrm{A}\cdot\sin(\omega\cdot t+\theta_0)\cdot\cos(\omega\cdot t) = A\cdot\sin(\omega\cdot t)\cdot\cos(\theta_0)\cdot\cos(\omega\cdot t) + \\ +A\cdot\cos(\omega\cdot t)\cdot\sin(\theta_0)\cdot\cos(\omega\cdot t) \qquad \text{(B.4)}$$

$$\mathrm{A}\cdot\sin(\omega\cdot t+\theta_0)\cdot\cos(\omega\cdot t) = \mathrm{A}\cdot\cos(\theta_0)\cdot\frac{1}{2}\cdot sin(2\cdot\omega\cdot t) + \\ +A\cdot\sin(\theta_0)\cdot cos^2(\omega\cdot t) \qquad \text{(B.5)}$$

$$cos^2(\omega\cdot t) = \frac{1+\cos(2\cdot\omega\cdot t)}{2} \qquad \text{(B.6)}$$

Substitute the equation B.6 into equation B.5 and get equation B.7:

$$A\cdot sin(\omega\cdot t+\theta_0)\cdot cos(\omega\cdot t) = A\cdot cos(\theta_0)\cdot\frac{1}{2}\cdot sin(2\cdot\omega\cdot t) + \\ +\frac{A}{2}\cdot sin(\theta_0) + A\cdot sin(\theta_0)\cdot\frac{1}{2}\cdot cos(2\cdot\omega\cdot t) \qquad \text{(B.7)}$$

Low-pass filter eliminates $sin(2\cdot\omega\cdot t)$ and $cos(2\cdot\omega\cdot t)$ terms:

$$LPF[A\cdot sin(\omega\cdot t+\theta_0)\cdot cos(\omega\cdot t)] = \frac{A}{2}\cdot sin(\theta_0) \qquad \text{(B.8)}$$

$$\frac{Q_0}{2} = \frac{A}{2}\cdot sin(\theta_0) \qquad \text{(B.9)}$$

$$Q_0 = A\cdot sin(\theta_0) \qquad \text{(B.10)}$$

So, Q_0 is In-Quadrature term.

The same situation occurs with In-phase term. Let's multiply the equation B.3 with $\sin(\omega \cdot t)$ function:

$$A \cdot sin(\omega \cdot t + \theta_0) \cdot sin(\omega \cdot t) = A \cdot sin^2(\omega \cdot t) \cdot \cos(\theta_0) +$$
$$+A \cdot \frac{1}{2} \cdot sin(\theta_0) \cdot sin(2 \cdot \omega \cdot t) \quad \text{(B.11)}$$

$$sin^2(\omega \cdot t) = \frac{1 - cos(2 \cdot \omega \cdot t)}{2} \quad \text{(B.12)}$$

Substitute the equation B.12 into the equation B.11 and get the equation B.13:

$$A \cdot sin(\omega \cdot t + \theta_0) \cdot sin(\omega \cdot t) = A \cdot \frac{1 - cos(2 \cdot \omega \cdot t)}{2} \cdot cos(\theta_0) +$$
$$+ A \cdot \frac{1}{2} \cdot sin(\theta_0) \cdot sin(2 \cdot \omega \cdot t) \quad \text{(B.13)}$$

Low-pass filter eliminates $sin(2 \cdot \omega \cdot t)$ and $cos(2 \cdot \omega \cdot t)$ terms:

$$LPF[A \cdot sin(\omega \cdot t + \theta_0) \cdot sin(\omega \cdot t)] = \frac{A}{2} \cdot cos(\theta_0) \quad \text{(B.14)}$$

$$\frac{I_0}{2} = \frac{A}{2} \cdot \cos(\theta_0) \quad \text{(B.15)}$$

$$I_0 = A \cdot cos(\theta_0) \quad \text{(B.16)}$$

So, I_0 is In-Phase term.

$$Q_0 = [A \cdot sin(\theta_0)] \quad \text{(B.17)}$$

$$I_0 = [A \cdot cos(\theta_0)] \quad \text{(B.18)}$$

where I_0 is the in-phase component, Q_0 is the in-quadrature component.

$$\mathrm{A} \cdot \sin(\omega \cdot t + \theta_0) = I_0 \cdot \sin(\omega \cdot t) + Q_0 \cdot \cos(\omega \cdot t), \quad \text{(B.19)}$$

I_0 and Q_0 components have coupled information about the amplitude and phase. It is necessary to decouple it. Arctangent function calculation gets phase information:

$$\theta_0 = \arctan\left(\frac{Q_0}{I_0}\right) = \arctan\left(\frac{A \cdot \sin(\theta_0)}{A \cdot \cos(\theta_0)}\right) \quad \text{(B.20)}$$

Calculation of the power will decouple amplitude information:

$$A = \sqrt{{Q_0}^2 + {I_0}^2} = \sqrt{A^2 \cdot sin^2(\theta_0) + A^2 \cdot cos^2(\theta_0)} \quad \text{(B.21)}$$

Digital Up-Conversion

Remind the equation B.20 and equation B.21:

$$\theta_0 = \arctan\left(\frac{Q_0}{I_0}\right) = \arctan\left(\frac{A\cdot\sin(\theta_0)}{A\cdot\cos(\theta_0)}\right) \tag{B.20}$$

$$A = \sqrt{{Q_0}^2 + {I_0}^2} = \sqrt{A^2 \cdot sin^2(\theta_0) + A^2 \cdot cos^2(\theta_0)} \tag{B.21}$$

Feedback holds the Amplitude and phase according to the set-points, so amplitude A and phase θ_0 are known, but I_0 and Q_0 are unknown. It is necessary to calculate the I_0 and Q_0 terms using amplitude and phase set-points.

$$tg(\theta_0) = \frac{Q_0}{I_0} \tag{B.22}$$

$$A^2 = {I_0}^2 + {Q_0}^2 \tag{B.23}$$

Let's reorganize the equation B.22:

$$Q_0 = I_0 \cdot tg(\theta_0) \tag{B.24}$$

And substitute the equation B.24 into the equation B.23:

$$A^2 = {I_0}^2 \cdot tg^2(\theta_0) + {I_0}^2 \tag{B.25}$$

$${I_0}^2 = \frac{A^2}{1+tg(\theta_0)^2} \tag{B.26}$$

$$I_0 = \frac{A}{\sqrt{1+tg(\theta_0)^2}} \tag{B.27}$$

$$Q_0 = \sqrt{A^2 - {I_0}^2} \tag{B.28}$$

Let's substitute the equation B.27 into the equation B.28:

$$Q_0 = \sqrt{A^2 - \frac{A^2}{1+tg(\theta_0)^2}} \tag{B.29}$$

Rewrite the equation B.29 into the equation B.30:

$$Q_0 = A \cdot \frac{tg(\theta_0)}{\sqrt{1+tg(\theta_0)^2}} \tag{B.30}$$

Remind the equation B.31:

$$\mathrm{A} \cdot \sin(\omega \cdot t + \theta_0) = A \cdot \sin(\omega \cdot t) \cdot \cos(\theta_0) + A \cdot \cos(\omega \cdot t) \cdot \sin(\theta_0) \tag{B.31}$$

Then rewrite into more understandable one:

$$\mathrm{A} \cdot \sin(\omega \cdot t + \theta_0) = I_0 \cdot \sin(\omega \cdot t) + Q_0 \cdot \cos(\omega \cdot t) \tag{B.32}$$

APPENDIX C

Future prospects

This chapter discusses future prospects of the RedPitaya STEMlab 125-14 FPGA board based LLRF feedback system RnD. The chapter describes a transfer of the FPGA board based LLRF feedback technology to KEK ATF facility (Linac and Damping Ring) and available upgrades of Digital Signal Processing routine programmed at FPGA chip.

Extension and transfer of the FPGA board based digital LLRF feedback technology to the KEK ATF facility

ATF is “Accelerator Test Facility” for International Linear Collider (ILC). KEK ATF facility is 1.29 GeV electron linear accelerator devoted to develop, implement and test linear collider technologies and other perspective technologies for fundamental accelerator science. ATF is large scale facility. It has laser driven RF-Gun, S-Band Linac (Injector) and Damping Ring. RF-Gun is the 3.6 cell standing wave accelerating structure. Linac accelerating structures are travelling wave structures. RF-Gun and Linac structures frequency is 2856MHz. Klystrons operate with 6.25 Hz repetition rate. Pulse length is less than 1μs. Damping Ring accelerating structure is travelling wave structure. Klystron operates at CW mode. Frequency is 714MHz.

Distance between Linac and Damping Ring dictates the structure of Low-Level RF distribution system. FPGA boards must be installed at the klystrons control racks far away from main SGs. FPGA board and server-client side programming developed for KEK LUCX facility is 100% applicable for KEK ATF Linac and Damping Ring. However, RedPitaya STEMlab 125-14 FPGA board needs a customization. It is 10MHz reference PLL input installation. This customization is available at the RedPitaya company website.

KEK ATF facility beamline is presented on the figure 81.

FPGA based LLRF feedback system feedback proposal is demonstrated on the figure 82.

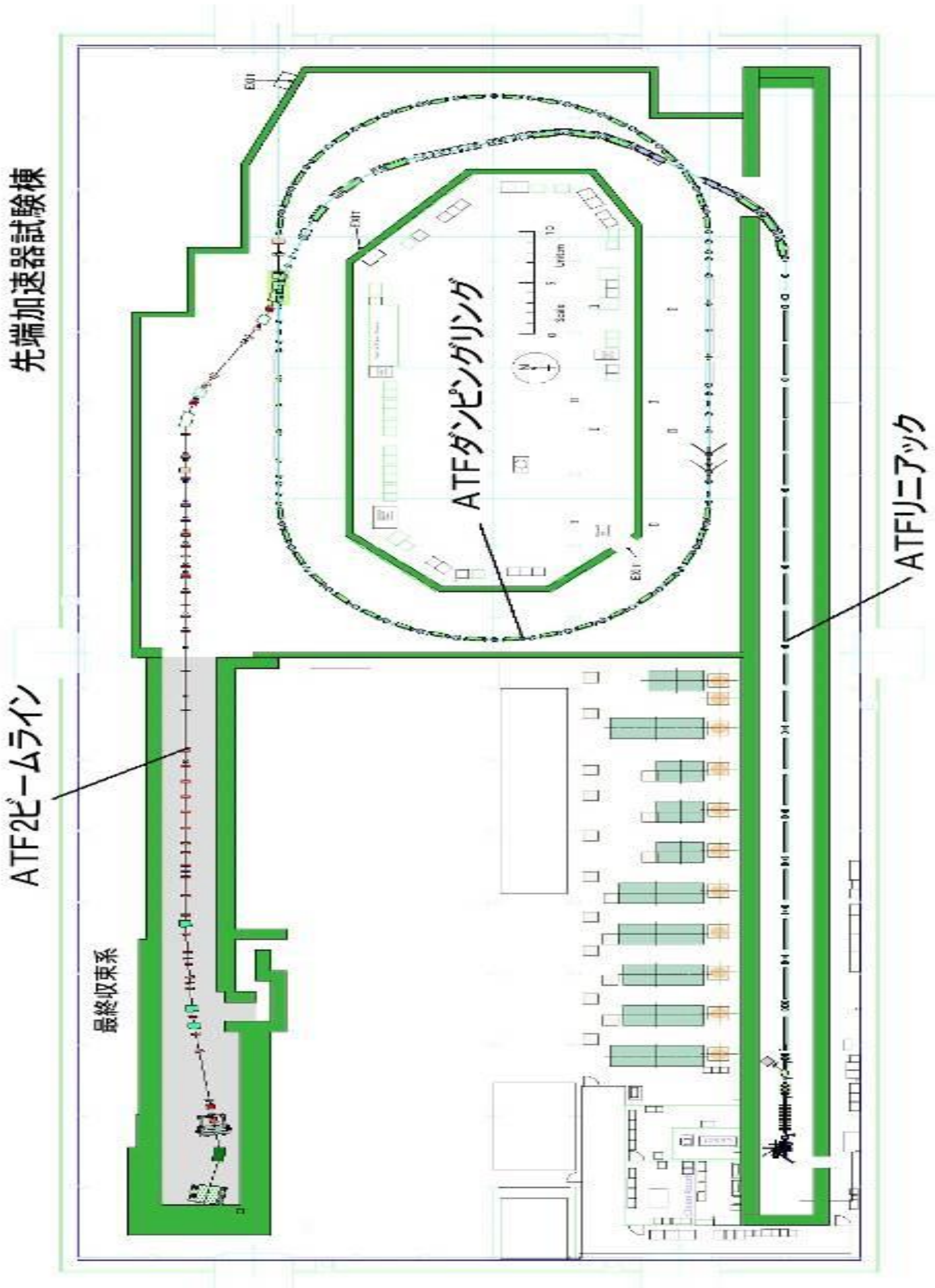

Figure 81: KEK ATF facility beamline layout

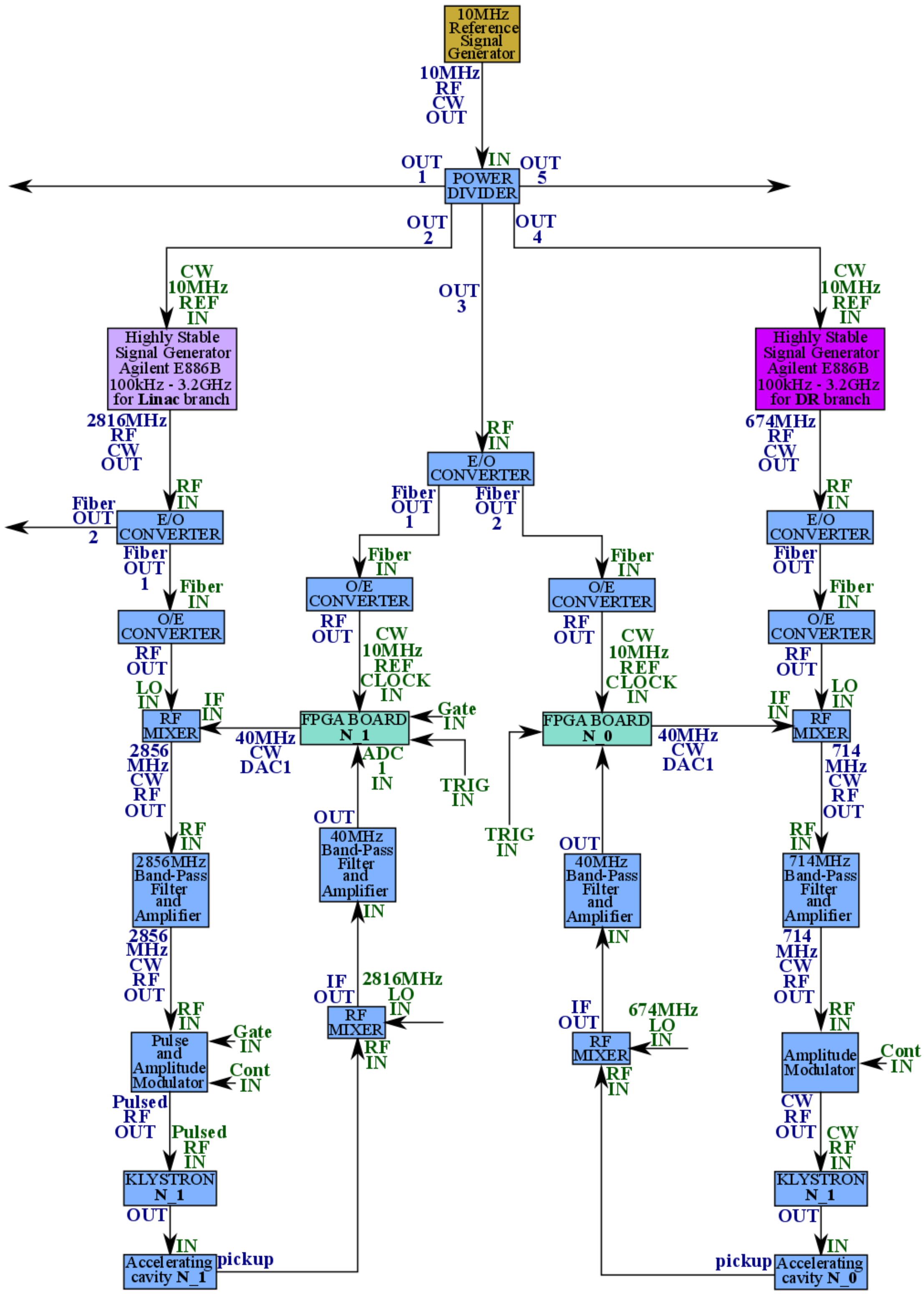

Figure 82: Proposed RedPitaya STEMlab 125-14 FPGA based LLRF feedback system

Linac and Damping Ring signal generators, FPGA boards are synchronized to the 10MHz Reference signal generator. Every SG has 10MHz reference input.

LLRF signals are distributed using fibers. RF signal is converted to the optical signal at E/O converter. Then optical signal is transferred at long distance by optical fiber. Optical signal is converted back to the electrical at klystron control station at O/E converter. Feedback system operates at frequency up- and down-conversion mode.

Bibliography

1. A. W. Stevenson et al., Phase-contrast x-ray imaging with synchrotron radiation for materials science applications, Nucl. Instrum. Methods Phys. Res., B 199, 427(2003).
2. O. Betz, U. Wegst, D. Weide, M. Heethoff, L. Helfen, W.-K. Lee, and P. Cloetens, Imaging applications of synchrotron x-ray phase-contrast microtomography in biological morphology and biomaterials science. i. general aspects of the technique and its advantages in the analysis of millimetre-sized arthropod structure, Journal of Microscopy 227, 51 (2007).
3. F. Arfelli et al., Low-dose phase contrast x-ray medical imaging, Phys. Med. Biol. 43 (1998).
4. K. Huke, 2.5 GeV electron storage ring construction at pf, Nucl. Instrum. Methods 177 (1980).
5. K. Tamasuka, Y. Tanak, M. Yabashi, H. Yamazaki, N. Kawamura, M. Suzuki, and T. Ishikawa, Spring-8 riken beamline iii for coherent x-ray optics, Nucl. Instrum. Methods Phys. Res., A 467-468, 686 (2001).
6. S. Amano et al., Several-MeV γ-ray generation at new-subaru by laser-Compton backscattering, Nucl. Instrum. Methods Phys. Res., A 602, 337 (2009).
7. K. Chouffani, D.Wells, F. Harmon, J. Jones, and G. Lancaster, Laser-Compton scattering from a 20 MeV electron beam, Nucl. Instrum. Methods Phys. Res., A 495, 95 (2002).
8. K. Aoki et al., High-energy photon beam production with laser-Compton backscattering, Nucl. Instrum. Methods Phys. Res., A 516, 228 (2004).
9. K. Sakaue et al., “Design Study on Linac-based Laser-Compton Scattering X-Ray Source”, Proceedings of IPAC2018, Vancouver, BC, Canada, 2018.
10. M. Endrizzi, X-ray phase-contrast imaging, Nucl. Instrum. Methods Phys. Res., A 878, 88 (2018).
11. V. Petrillo et al., Photon flux and spectrum of γ-rays Compton sources, Nucl. Instrum. Methods Phys. Res., A 694, 109 (2012).
12. M. Fukuda et al., “Development and Upgrade Plan of an X-Ray Source Based on Laser-Compton Scattering in Laser Undulator Compact X-Ray Source (LUCX)”, Proceedings of IPAC2016, Busan, Korea, 2016.

13. K. Sakaue et al., “Development of a Compact X-Ray Source Based on Laser-Compton Scattering with a Pulsed-Laser Super-Cavity”, Proceedings of EPAC08, Genoa, Italy.
14. RedPitaya company website: https://redpitaya.com/product/stemlab-125-14/
15. Xilinx company website: https://www.xilinx.com/products/silicon-devices/soc/zynq-7000.html
16. A. Aryshev et al., “Femtosecond response time measurements of a Cs_2Te photocathode”, Appl. Phys. Lett. 111, 033508 (2017).
17. Kwang-Je KIM, “RF and Space-Charge Effects in Laser-Driven RF electron Guns”, Nuclear Instruments and Methods in Physics Research, A 275 (1989) 201-218.
18. N. Terunuma et al., “Improvement of an S-band RF-Gun with a Cs2Te photocathode for the KEK-ATF’, Nuclear Instruments and Methods in Physics Research, A 613 (2010).
19. T. Aoki, “Development of an S-band Multi-Cell Accelerating Cavity for RF-Gun and Booster Linac”, Proceedings of IPAC2011, San Sebastian, Spain, 2011.
20. etd.canon/en/product/category/microwave/klystron.html
21. etd.canon/en/product/category/microwave/klystron.html
22. thermofisher.co/order/products/jp/en/TF1400-LN
23. Mitsubishi Electric website: mitsubishielectric.com/bu/air-conditioning-systems/
24. EPICS website, https://epics.anl.gov/EpicsDocumentation/AppDevManuals/
25. Bergoz Instrumentation company website: bergoz.com/products/ict/
26. Takasago LTD. Company website:
takasago-ss.co.jp/products/power_electronics/dc
27. B.Q.Zhao, L.Y.Zhao, M.Liu, C.X.Yin, "Implementation of SINAP timing system into Shanghai proton therapy project", IPAC2016.
28. Qtcreator website: https://www.qt.io/product/development-tools
29. EPICS Qt page at Github: https://qtepics.github.io/
30. K. Popov et al., “KEK LUCX facility Laser-to-RF&RF-to-RF Stability Study and Optimization”, Proceedings of IPAC2022, Bangkok, Thailand, 2022
31. A.Rhyder, A.Owen, G. Jackson, "Qt EPICS development framework", PCaPAC 2010.

32. ASTRA tracking code website page https://www.desy.de/~mpyflo/Astra_manual/Astra-Manual_V3.2.pdf
33. SATA standard page at wikipedia: https://en.wikipedia.org/wiki/SATA
34. Rohde Schwartz website page: https://www.rohde-schwarz.com/us/products/test-and-measurement/analog-signal-generators/rs-smb100a-microwave-signal-generator_63493-9379.html
35. https://www.keysight.com/us/en/product/E5052B/signal-source-analyzer-ssa.html
36. RedPitaya forum: forum.redpitaya.com
37. fpgatutorial.com/verilog/
38. Xilinx Vivado website: https://www.xilinx.com/products/design-tools/vivado.html
39. xilinx.com/products/intellectual-property/stream-broadcaster.html
40. xilinx.com/products/intellectual-property/dds-compiler.html
41. xilinx.com/products/intellectual-property/complex-multiplier.html
42. xilinx.com/products/intellectual-property/cic-compiler.html